

**Electron propagation in solid matter as a result of
relativistic laser plasma interactions**

Dissertation

zur Erlangung des akademischen Grades
doctor rerum naturalium (Dr. rer. nat.)

vorgelegt dem Rat der Physikalisch - Astronomischen Fakultät der Friedrich-Schiller
Universität Jena

von Dipl.-Phys. Flavio Zamponi
geboren am 08. 05. 1975 in Macerata, Italien

Gutachter

1.

2.

3.

Tag der letzten Rigorosumsprüfung

Tag der öffentlichen Verteidigung

Contents

Acknowledgements	iv
1 Introduction	1
2 Electron behaviour at relativistic intensities	4
2.1 Motivations	4
2.1.1 The fast ignitor	4
2.1.2 The laser-plasma interaction at relativistic intensities	5
2.1.3 The X-ray source	6
2.2 The laser system	8
2.3 Fast electrons in matter	11
2.3.1 Scaling laws for fast electrons	11
2.3.2 Collision times	13
2.3.3 Return currents	13
2.3.4 Ohmic Heating	15
2.3.5 Magnetic Fields	16
2.3.6 Weibel and other instabilities	20

2.4	Satellites	21
2.5	Spectropolarimetry	25
3	The X-ray spectrometer	30
3.1	Introduction	30
3.2	Principle of the spectrograph	30
3.3	Spectral and spatial properties	32
3.4	Non-dispersive setup	37
3.5	Integrated reflectivity for bent crystals	41
4	Magnetic field measurements: Zeeman effect in the X-ray regime	43
4.1	Introduction	43
4.2	Experimental setup	45
4.3	Results	47
4.4	Simulation	51
4.5	Conclusions	59
5	Spectropolarimetry of solid-density plasmas generated by fs laser pulses	60
5.1	Introduction	60
5.2	Experimental setup	61
5.3	Space and polarization dependent spectra	62
5.4	Conclusions	67
6	Energy resolved 2D imaging of an X-ray source at relativistic intensities	68
6.1	Introduction	68
6.2	Experimental Setup	68
6.3	Titanium foils: Results	70
6.4	Layered Target: Results	73
6.5	Conclusion	79
7	Discussion	81

8 Summary	83
Bibliography	86
A Characterization of the CCD	95
A.1 Introduction	95
A.2 The Quantum Efficiency	95
A.3 Spatial resolution	101
B Zusammenfassung	105

Acknowledgments

I would like to thank all those that more or less directly helped me in these, not always simple, years.

First of all I would like to thank Prof. Förster for the exciting topics of my PhD thesis and Ingo Uschmann for the support, invaluable discussions, patience and his deep knowledge in this field.

I would like to thank also E. Kroupp, E. Stambulchik and Y. Maron for the support on the magnetic field measurements and M. Deutsch for clarifying discussions about satellites.

I thank my colleagues from Düsseldorf and Pisa for the fruitful and reliable collaboration.

A special thank goes to Tino Kämpfer, for interesting discussion, support during the measurements, experimental skills, suggestions and irony. I also enjoyed the pleasant atmosphere in the X-ray Optics Group.

Last but not the least, Andrea who had to deal with me, not only in the lab but also at home.

E grazie anche a te Michelino: senza di te sarebbe stato diverso.

Flavio Zamponi

Jena

Progresses in laser technique with the possibility to amplify fs laser pulses [Strickland and Mourou, 1985], thank to the chirped pulse amplification technique, allowed in the last years giant steps in the comprehension of the laser-plasma interaction subject. The application of the new knowledges brought to the birth and development of new fields of research:

- femtosecond laser-produced plasma spectroscopy [Gauthier et al., 1995];
- efficient ultra-short X-ray pulse production [Rousse et al., 1994] and its applications in the time resolved X-ray diffraction field to study, for example, in the sub-ps regime, the transient state of laser heated organic film [Rischel et al., 1997], the non-thermal melting in semiconductors irradiated by fs laser pulses [Rousse et al., 2001b] or the atomic motion (i. e. phonons) in bismuth [Sokolowski-Tinten et al., 2003];
- the possibility to accelerate
 - electrons** [Modena et al., 1995; Amiranoff et al., 1998] by exploiting the coupling between laser field and electrons;
 - protons** see [Ledingham et al., 2003] and references therein;
 - ions** [Hegelich et al., 2002; Busch et al., 2003] by using the extremely high electric fields induced by the charge separation at the back side of the target;
- the production of quasi-monochromatic bunches of

-
- electrons** [Faure et al., 2004; Geddes et al., 2004; Mangles et al., 2004] utilising the “bubble regime” [Pukhov and Meyer-ter-Vehn, 2002], a solitary plasma cavity moving in the underdense plasma;
 - protons** [Schwoerer et al., 2006] exploiting micro-dot targets to reduce the extension (and, on the same time, the differences in the intensity, i. e. the spectrum) of the accelerating electric field at the back of the target;
 - ions** [Hegelich et al., 2006] by using a well characterized target to reduce the contaminants (hydrogen) to an exploitable level and to have only C^{5+} and C^{6+} at the surface to be accelerated;
- laser triggered nuclear reactions: some authors used MeV photons created by bremsstrahlung to fission Be by using a tabletop laser [Schwoerer et al., 2001] or Au and U with a PW class laser [Cowan et al., 2000]. [Ditmire et al., 1999] were able to obtain fusion neutrons by using 10^{16} W/cm² laser pulses on deuterium clusters; also [Pretzler et al., 1998] could show fusion in a deuterated plastic target;
 - the proposal of the Fast Ignitor [Tabak et al., 1994] (see next Chapter) and its last improvements [Kodama et al., 2001, 2002]: the use of hollow cones directly connected with the core of the target (a deuterated polystyrene) allowed a more effective heating and ignition from the PW pulse.

This thesis groups heterogeneous results coming from three experiments. The *leitmotiv* is the electron behaviour in the target during and after the interaction between a laser pulse and cold target at relativistic intensities.

The chapter will be organized as follows: first of all I will try to convince the reader about the importance of such a subject, then the physical methods that were used during the work will be presented, and finally a picture of the state of the art in the research from both experimental and theoretical sides will be offered.

This thesis describes the results and the implications of three experiments performed at the JeTi (Jenaer Ti:Sapphire) laser system. The measurement of the Zeeman effect in the

X-ray regime by exploiting the magnetic field created by the interaction of ultra-intense fs laser pulses with solid target will be discussed in Chapter 4. The polarization dependence of high resolution X-ray spectra as a tool to infer the electron velocity distribution at relativistic intensities inside the target will be matter of Chapter 5. Finally, in Chapter 6, the electron transport in solid plasma at intensities of about 5×10^{19} W/cm² detected by an energy resolving 2D X-ray imaging system will be investigated.

Chapter 2

Electron behaviour at relativistic intensities

2.1 Motivations

Three main reasons could be indicated as possible motivations to undertake a work about the motion of electrons as a result of relativistic interaction between laser and plasma: one is connected with the fast ignitor approach to the nuclear fusion, the second is the need to better understand the interaction between laser and plasma (there are only few fields in the physics expanding so quickly) and the third is the need to better know the physics behind a laser-produced X-ray source.

2.1.1 The fast ignitor

The fast ignitor is an alternative approach to the inertial confinement fusion [Tabak et al., 1994]. The basic idea is to separate the compression from the ignition: first, ns laser pulses are employed to compress the deuterium pellet to about 300g/cm^3 ; second, a multi-ps pulse drills a hole through the coronal plasma to reduce the distance between the target surface and core; then an ultra-intense laser pulse of PW class is used to generate hot electrons that ignite the core. The main advantages of the fast ignitor proposal are reduction of the total energy required to achieve the ignition and relaxed requirements about the symmetry of the compression phase (instabilities during the compression phase are less deleterious because the ignition is a step separated from the compression).

Since the fast ignitor proposal in 1994 huge efforts have been made in the research to understand the process of generation and transport of hot electrons needed in the last and

decisive phase of the fast ignitor. However some aspects remain still less understood than others. I present here a short list.

- The anomalous inhibition of the electron transport in cold solid target is now relatively well understood and good simulation codes have already been working for non-relativistic intensities [Bell et al., 2006]. What happens if we go to higher intensities?
- What happens if the target is an insulator? There are models to simulate the behaviour of metallic targets: very few was done/understood for insulator, even if foam or plastic targets (coupled with buried fluor layers) have been used since years.
- The role of the magnetic fields. Theoretical works have predicted gigagauss magnetic fields in the laser-plasma interaction already 15 years ago. However there are only few experimental works on this subject. Even if we propose in this thesis a new way to diagnose them by means of the Zeeman effect, the impact of such huge fields on the electron transport and, mainly, how to exploit them in the fast ignitor scheme is still not clear.

2.1.2 The laser-plasma interaction at relativistic intensities

When ultra-short laser pulses are focused on to a solid target at intensities of $\geq 10^{18}$ W/cm², in a thin layer (≈ 100 nm) at the interface vacuum–target, ions and electrons experience an electric field from the incident radiation [Gibbon et al., 1996]. This field is much stronger than typical atomic fields. The thickness of the created plasma layer is of the order of the penetration depth of the laser radiation in the target material, which ranges from a few tens up to a few hundreds of nanometers. Since a typical plasma expansion velocity is 0.1 nm/fs, no significant hydrodynamic motion occurs during the laser pulse for pulse durations shorter than 100 fs [Ziener et al., 2002]. This means that the laser interacts with a plasma of almost solid density ($n_e \approx 10^{23} \dots 10^{24}$ e/cm³). In this layer the atoms are instantaneously ionized and a thin layer of dense plasma is created.

To describe the type of the interaction, the dimensionless parameter $a = eA/mc^2$ is used (e is the electron charge and A is the vector potential): if $a > 1$ one speaks of relativistic interaction. This condition can be rewritten as $I\lambda_0^2 = 10^{18} \text{ W/cm}^{-2}\mu\text{m}^2$, where λ_0 is the laser wavelength. As soon as $a > 1$ the charged particles in the plasma are accelerated up to MeV energies through various mechanisms (Brunel effect [Brunel, 1987], anomalous skin effect [Rozmus and Tikhonchuk, 1990], resonant absorption) in the forward direction.

The presence of a prepulse has important consequences on the laser-plasma interaction. It creates a small plasma before the main pulse arrives and changes the physics of the problem. The plasma scale length $L \doteq \left| \frac{n}{\nabla n} \right|_{n=n_c} = v_i t$ (n is the plasma density, n_c is the critical plasma density and v_i the sound velocity of the plasma) describes how large the plasma in front of the target is and, more important, how steep the gradient is at the critical density. If there is no prepulse, the resonant absorption is not effective because there is no well definite plasma critical layer.

Since the plasma is almost collisionless, there is no reason for the energy-carrying electrons to have a Maxwellian distribution. On the contrary the energy is given to a small fraction of electrons, called “hot” or “fast”, with a characteristic energy determined by the mechanics of the absorption process.

2.1.3 The X-ray source

Electrons accelerated in the plasma by the laser pulse and injected in the cold target create X-ray radiation via bremsstrahlung and K-shell ionization [Rousse et al., 1994]. There are many features that makes such a source appealing [Rousse et al., 2001a]: the X-ray burst is relatively bright (up to 10^{12} Ti-K α photons per pulse can be produced [Ewald et al., 2002]), the expected duration is 200-600 fs, depending on the material, target thickness and intensity [Feurer et al., 2001; Reich et al., 2000; Reich, 2002; Sokolowski-Tinten et al., 2003; Bargheer et al., 2004], and the source is small (down to $10 \mu\text{m}$ as measured in [Zhavoronkov et al., 2005]). These features make it an ideal source for time resolved X-ray diffraction experiments in optical pump X-ray probe setup: for example, in [Morak et al., 2006] the

propagation of acoustical phonons in InSb bulk could be monitored, in [Lübcke et al., 2005] the Borrmann effect was used to sensibly reduce the X-ray transmission through a GaAs crystal in the ns timescale.

Moreover, in experiments where high intensity laser pulses are used, the $K\alpha$ emission has been often used to monitor the electron behaviour in the matter. Typically layered target are used. The upper layer is the medium through which the electrons propagate and, at variable depths, the fluor medium; its $K\alpha$ emission is observed: intensity and shape give hints on the electron motion in the target [Batani et al., 2002, 2005; Pisani et al., 2000; Key et al., 1998; Koch et al., 2001; Beg et al., 1996; Martinolli et al., 2006].

However still many aspects are not clear. The dimension of the $K\alpha$ -source is expected to be of the order of the laser spot size with a small broadening due to the scattering of the electrons inside the target material. While this is confirmed for relatively low laser intensities (10^{16} - 10^{17} W/cm²), experiments have shown that in the high intensity range ($\geq 10^{18}$ W/cm²) the X-ray source is much larger than expected, having the main peak surrounded by a halo of weak $K\alpha$ emission, see [Reich et al., 2003]. It is to be noticed that in [Pretzler et al., 2003] exactly the opposite was found: at relativistic intensities the source dimension has become much smaller. Possible explanations for this are proposed by [Reich, 2002]: magnetic fields created by the interaction of the main pulse with the plasma [Sudan, 1993] in combination with the self induced fields in the target created by the electron motion [Bell et al., 1997, 1998, 2006] and additional electric fields at the back of the target [Romagnani et al., 2005], should deflect expanding electrons back to the target in a large spot and thus producing a larger X-ray source. Another explanation might be: electrons enter the solid with an angular spread. Such electrons beams were found in a half-cone angles of 15, 30 and 90 degrees [Wharton et al., 1998; Pretzler et al., 2003; Koch et al., 2001; Stephens et al., 2004]. In [Wharton et al., 1998] the lower energy electrons ($E \leq 200$ keV) were found to enter the target isotropically while the high energetic ones from a narrow beam.

It is to be mentioned that already at the beginning of the '80s some authors [Fabbro and Mora, 1982; Wallace, 1985; Forslund and Brackbill, 1982] could explain the presence of a

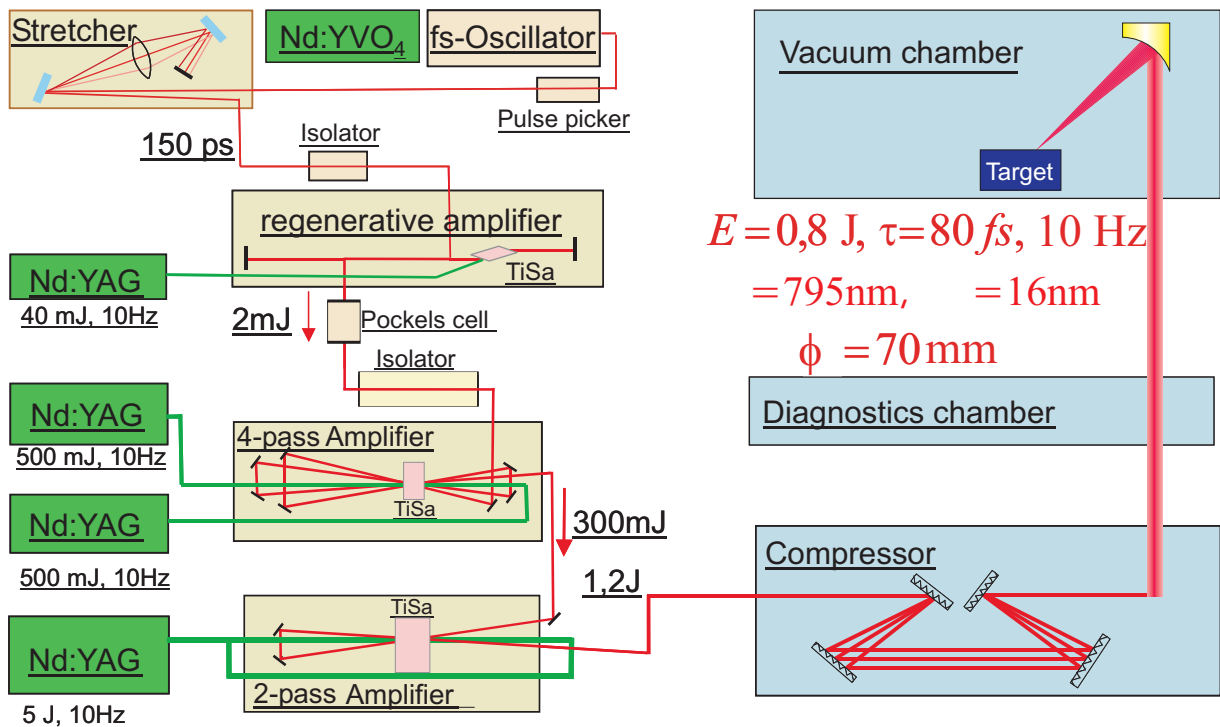


Figure 2.1: Schematic of the JeTilaser system.

halo surrounding the X-ray emission, observed for example in [Kieffer et al., 1984; Luther-Davies et al., 1987; Burgess et al., 1985] by taking into account electric and magnetic fields created at the plasma–vacuum interface.

2.2 The laser system

The experiment was performed using the JeTi, Jenaer Ti:Sapphire, multi-TW chirped-pulse-amplified laser system [Ziener et al., 2002] (see Fig. 2.1). The system consists of an oscillator, a stretcher, a regenerative amplifier, two additional multi-pass amplifiers, and an in-vacuum compressor. The maximum energy output before compression is 1.4 J, giving about 0.7 J after compression, with a pulse duration of 70 fs at a repetition rate of 10 Hz. After the compression, the laser beam traverses a diagnostic chamber and then it is guided to the target chamber through a vacuum beam-line in order to avoid a nonlinear

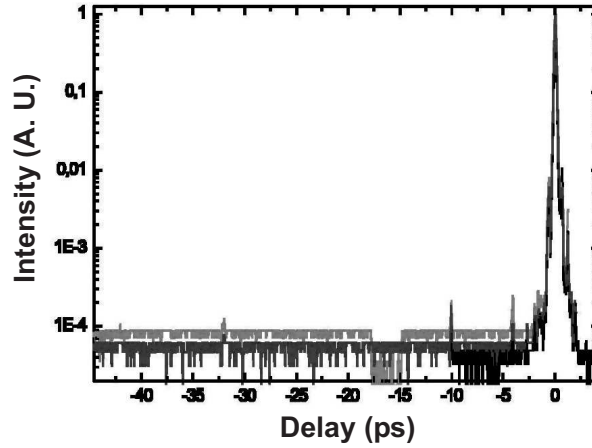


Figure 2.2: *Third order autocorrelation measurement of the laser pulse. From [Veisz et al., 2004]*

interaction of the laser pulse with the atmosphere. In the target chamber the beam can be focused by an off-axis parabolic mirror on to a foil-target to spot sizes down to $5 \mu\text{m}^2$, yielding irradiances up to $5 \cdot 10^{19} \text{ W/cm}^2$.

In the diagnostic chamber a third order autocorrelator can be used to monitor the pulse temporal profile at ps scale with a dynamic range of four orders of magnitude. There are two prepulses at 4 ps and 600 fs before the main pulse, having an intensity contrast ratio of 2×10^{-4} and 5×10^{-3} , respectively. No other prepulses with a contrast ratio bigger than 10^{-4} were detected within 200 ps before the main pulse. A typical autocorrelator trace is reported in Fig. 2.2. The contrast ratio in the time domain 5 ns and more before the main pulse was measured using a fast photo diode with filters.

An important remark has to be done for the experiments described in Chapters 4 and 5: between the first and the second run a fast Pockels cell unit was inserted after the regenerative amplifier. The high-intensity part of the pulse is preceded by a 5-ns long low-intensity pedestal due to ASE mainly generated in the regenerative amplifier. By changing the position of the gate relative to the main pulse, the pedestal is either fully or partially transmitted or almost fully suppressed to a minimum prepulse duration of 500 ps. The two prepulses at 4 ps and 0.6 ps before the main pulse, respectively, create a preplasma

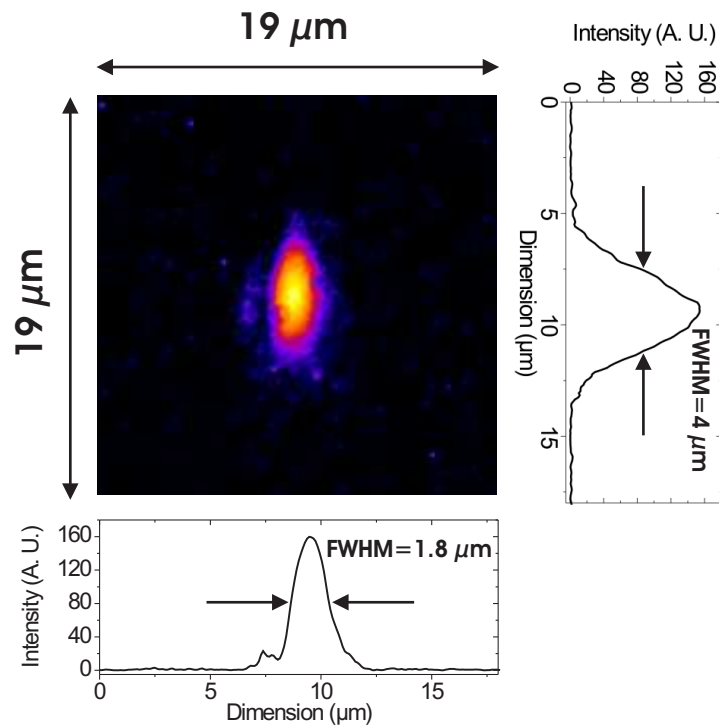


Figure 2.3: Imaging of the focal spot, together with its horizontal and vertical lineouts.

with a scale length of about $100\ \text{nm}$ [Ziener et al., 2002]. The presence of the fast Pockels cell between the first and the second run could have influenced the characteristics of the preplasma–plasma: simulations performed in [Kaluza et al., 2004] under similar conditions indicated an influence of the ASE on the bulk of the target, radiatively heated due to X-rays generated in the focus of the prepulse on the target front side. Moreover, the presence of a preplasma has a dramatic influence on the characteristics of the satellite emission and the magnetic field generation (see later in Chapter 4).

The measurement of the laser focal spot dimension was done in the target chamber. By using a strong beam attenuator and a microscope objective put in the place of the target an image of the focal spot, with a magnification of about 50, could be made for the same conditions used later in the experiment, i. e. vacuum, same laser energy, same amplifiers. A small CCD was used as a detector. For the calibration a mesh with a $50\ \mu\text{m}$ step was

imaged (not shown here). In Fig. 2.3 a typical focal spot is shown. The FWHM surface was about $5 \mu\text{m}^2$.

2.3 Fast electrons in matter

Let us consider now the motion of the electrons in cold matter. After the laser pulse has turned off we have the following situation: there are electrons with energies up to MeV, they are almost collisionless and, for this reason, far away from equilibrium. Their propagation in the forward direction, in the cold target, encounters immediately the resistance opposed by the charge separation: the ions, less mobile because of their higher inertia, exert an attractive electrostatic force that would prevent any further propagation. The fast electrons can propagate in the cold target only if counter propagating currents (the return currents) provide a sufficient charge compensation for their motion. In other words: the motion of high energetic electrons is heavily subjected, through strong electric fields, to the presence and mobility of electrons with much less energies (up to some keV), forming the return currents.

The formulae that we will deduce in the next sections, based mainly on the pioneering works of A. R. Bell, see [Bell et al., 2006] and references therein, make connections between these two portions of the electron spectrum (high and low energy) showing the surprising importance of the low energy component. It's worth mentioning that A. R. Bell is one of the few people able to reliably simulate these complicated interactions between slow and fast electrons in dense plasmas, under the influence of self-induced electric and magnetic fields.

2.3.1 Scaling laws for fast electrons

The electrons in a plasma (with density n) irradiated by a laser pulse acquire an energy T (in eV)¹ and escape the absorption region with a thermal velocity $\sqrt{2T/m_e}$ transport-

¹It is the energy kT_e of an electron having a temperature T_e , where k is the Boltzmann constant

ing energy with a flux $\frac{3}{2}neT\sqrt{2T/m_e}$ (here a Maxwellian distribution was assumed but, especially for short pulses and high energy electrons, which are almost collisionless, this need not to be true). Only a fraction of the electrons transports energy: the energy flux is usually written as $Q = fQ_{free}$, where $Q_{free} = neT\sqrt{2T/m_e}$ is “free-streaming heat flow” and f is a flux limiter. ²

By equating the absorbed energy flux with the electron energy flux we have:

$$\eta I_{18} = 0.02fn_{23}T_{keV}^{3/2}, \quad (2.1)$$

where T_{keV} is the energy of the energy-carrying electrons in keV, n_{23} is their density in units of 10^{23} cm^{-3} , I_{18} is the laser intensity in units of 10^{18} W/cm^2 and η is the fraction of absorbed laser energy.

In [Beg et al., 1996] a function was used to fit the measured electron energy in dependence of the laser intensity in the range 10^{16} W/cm^2 to $5 \times 10^{18} \text{ W/cm}^2$ (Beg’s law):

$$T_{keV} = 200(I_{18}\lambda_{\mu m}^2)^{1/3}, \quad (2.2)$$

where $\lambda_{\mu m}$ is the wavelength in μm . Rearranging this with eq. 2.1, yields

$$n_{21} = \frac{2f}{\eta}I_{18}(I_{18}\lambda_{\mu m}^2)^{-1/2} : \quad (2.3)$$

one can see that the density of fast electrons required to carry the energy flux can exceed the critical density $1.1 \times 10^{21} \lambda_{\mu m}^{-2} \text{ cm}^{-3}$ (where the factor $2\eta/f \approx 1$ can be used for high intensity laser pulses if electrons are free to escape the absorption region). To this energy and density corresponds a high pressure:

$$P_{Mbar} = 640\frac{\eta}{f}I_{18}(I_{18}\lambda_{\mu m}^2)^{-1/6}. \quad (2.4)$$

²If fluid codes are used to model laser-plasma interaction, the heat transfer is described by the Spitzer-Härm [Spitzer and Härm, 1953] heat diffusion law. This law overestimates the heat flux near the critical surface because of the steepness of the temperature gradient: an heat flux limiter, f , is therefore used to be able to reproduce the measured data [Matte and Virmont, 1982]. The heat transport is non-local [Bell et al., 1981].

As for eq. 2.1, by using the energy flux conservation, we can get:

$$j_{16} = \eta I_{18} T_{MeV}^{-1}; \quad \mathbb{I}_{MA} = 100\eta P_{100} T_{MeV}^{-1}, \quad (2.5)$$

where j_{16} is the current density in 10^{16} Am^{-2} , \mathbb{I}_{MA} is the current in megaamperes and P_{100} is the laser power in units of 100 TW. Using eq. 2.2, we can rewrite them in:

$$j_{16} = 5\eta I_{18} (I_{18} \lambda_{\mu m}^2)^{-1/3}; \quad \mathbb{I}_{MA} = 500\eta P_{100} (I_{18} \lambda_{\mu m}^2)^{-1/3}. \quad (2.6)$$

If we insert our laser parameters ($\eta = 0.1$) we obtain an electron temperature $T_{keV} \approx 400 \text{ keV}$ (to be compared with the measured value 1.4 MeV, see Chapter. 5), a fast electron density $n \approx 5 \times 10^{21} \text{ cm}^{-3}$ and a current of about 200 MA.

2.3.2 Collision times

By inserting eq. 2.2 in the collision time, taken from the NRL plasma formulary [NRL, 2006], one gets the mean free path (mfp) for fast electrons (with Coulomb logarithm set to 5):

$$\text{mfp} = 10^4 Z^{-1} n_{23}^{-1} (I_{18} \lambda_{\mu m}^2)^{2/3}. \quad (2.7)$$

Substituting with the parameters at our disposal yields $\text{mfp} \approx 22 \text{ mm}$ which is much larger than the target thickness.

2.3.3 Return currents

The fast electron current must be balanced by (thermal) electrons moving in the opposite direction.

In [Bell et al., 1997] the need of these return currents is vividly explained with an example: let us consider a laser pulse impinging on a target. Let us assume that the absorbed energy be $\epsilon_{laser} = 7.1 \text{ J}$, the laser pulse duration $\tau_{laser} = 1 \text{ ps}$, the fast electron temperature $T_0 = 200 \text{ keV}$, and the laser spot diameter $2r_{spot} = 30 \mu\text{m}$. The current brought by the fast electrons is $\mathbb{I} = \epsilon_{laser} / \tau_{laser} / (1.5T_0) = 24 \text{ MA}$. If the current entered the target, in the cylinder with radius r_{spot} , the magnetic field at the cylinder surface would

be $B = 3200$ MG. If the current penetrated into the target for a distance $R_e \approx 60\mu\text{m}$ (the fast electron root-mean-square range) then the energy stored in the magnetic field would be $(B^2/2\mu_0)\pi r_{spot}^2 R_e 2 \log(R_e/r_{spot}) = 5$ kJ, which is energetically impossible (the input energy was much smaller), implying that such a current cannot be maintained.

The return currents are drawn by electric fields. By assuming that the thermal electron can be considered as a separate component of the plasma having conventional electrical conductivity σ , one can calculate the electric field $E = j_f/\sigma$ (the subscript “ f ” and “ t ” indicate *fast* and *thermal*, respectively), needed to compensate the fast electron current j_f :

$$E_{10} = 5\sigma_6^{-1}\eta I_{18}(I_{18}\lambda_{\mu\text{m}}^2)^{-1/3}, \quad (2.8)$$

where E_{10} is the electric field in units of 10^{10} V/m and σ_6 the electrical conductivity in units of $10^6\Omega^{-1}\text{ m}^{-1}$. Such an electric field can stop fast electrons with an energy following the Beg’s law in a distance:

$$L_{\mu\text{m}} = 4\sigma_6\eta^{-1}I_{18}^{-1}(I_{18}\lambda_{\mu\text{m}}^2)^{2/3}. \quad (2.9)$$

Substituting for our parameters (we used $\sigma_6 = 1$, the value for aluminium at ≈ 100 eV) we obtain $E \approx 3.5 \times 10^{10}$ V/m and $L \approx 12\mu\text{m}$. We can see that the electric fields induced by the fast electrons are strong enough to brake them in very short distances; on the contrary, collisions, see eq. 2.7, have no effects on the dimension scale of the target thickness.

This transport inhibition was already found in a number of experiment, for example in [Feurer et al., 1997]. There laser pulses were focused to 5×10^{18} W/cm² on a thin aluminium layer deposited on a copper target. No Cu-K α photons were measured if the Al was thicker than 800 nm. Similarly, in other experiments, results could be explained only by invoking an inhibiting mechanism for the electron transport (see, for example [Feurer et al., 1997; Pisani et al., 2000; Teubner et al., 1996]).

In [Guerin et al., 1999] a 1D PIC simulation was performed in which the collisions could be turned off: the fast electrons could, in this case, penetrate in the material because the thermal electrons were able to provide the return current and, consequently, the electric fields were relatively small. On the contrary, with the collisions included, the fast electron transport was inhibited.

We stress the fact that the mean free path (as shown in eq. 2.7) is much larger than the target thickness (about 25 μm) and that the fast electrons are inhibited only by the fields. The collisions are involving only the *thermal* electrons, anyway collisions have an enormous impact on the *fast* electron propagation.

3D PIC code were employed to simulate the return currents, e. g. [Honda et al., 2000; Sentoku et al., 2002, 2003]. They found that return and fast electron currents balance out locally (see later eq. 2.12): the total amount of current is almost zero in every point. Both the forward and return currents are widely distributed in the transverse space, and they are not well separated, i. e., the current neutralization works well. In [Honda et al., 2000] the typical energy for return current is estimated to be of the order of $\sim \text{keV}^3$, i. e. enough to produce vacancies in the K-shell of a titanium target.

2.3.4 Ohmic Heating

As just mentioned direct heating due to the fast electrons cannot be effective because they are not collisional. In the same way the electric fields dominate the transport, they dominate also the heat exchange. The fast electrons do work against the field and, correspondingly, the thermal electrons are ohmically heated with a volume heating rate $1.5n_t e(d\theta/dt) = j_f^2 \sigma$, where θ is the thermal electron temperature in eV and n_t is the thermal electron density. By inserting the value for j_f from eq. 2.5 one gets a temperature for the thermal electrons during the laser pulse $\theta = 90\sigma_6^{-1} n_{t,23}^{-1} t_{ps}^2 \eta^2 I_{18}^2 (I_{18} \lambda_{\mu\text{m}}^2)^{-2/3} \text{keV}$. By taking into account the variation of σ with the temperature, i. e. by using the Spitzer formula [NRL, 2006] $\sigma_6 = 1.310^8 Z^{-1} \theta_{\text{keV}}^{3/2}$ in units of $10^6 \Omega^{-1} \text{m}^{-1}$, the temperature can be rewritten:

$$\theta(t) = 1.3 n_{t,23}^{-2/5} t_{ps}^{2/5} Z^{2/5} \eta^{4/5} I_{18}^{4/5} (I_{18} \lambda_{\mu\text{m}}^2)^{-4/15} \text{keV}, \quad (2.10)$$

³The energy of return current electrons are difficult to estimate also because the very concept of return current is difficult to define in a non-ambiguous way. In [Guerin et al., 1999] it is shown that the concept of return current is badly defined and that one can abstain to use it. Anyway, even if not enough accurate, it helps, also in a pictorial way, to understand the complicated physics involved.

$$\sigma(t) = 2n_{t,23}^{-3/5} t_{ps}^{3/5} Z^{-2/5} \eta^{6/5} I_{18}^{6/5} (I_{18} \lambda_{\mu m}^2)^{-2/5} \times 10^8 \Omega^{-1} \text{m}^{-1}, \quad (2.11)$$

where Z is the atomic number.

According to these formulae, the temperature rises up to 1 keV increasing the conductivity and reducing the electric fields and the inhibition would not occur. The equation 2.11 should be applied to the target as a whole. In reality the plasma temperature increases first in regions close to the front surface; but the fast electrons already went farther in the cold target. For them the transport inhibition can indeed occur.

In the derivation of eqs. 2.10 and 2.11 the validity of the Spitzer conductivity for the thermal electrons was assumed. However, this can be incorrect for low intensities because of the material properties (insulator and metal for low temperature have different behaviours) and for high intensities because the amount of hot electrons can be large (in the derivation of the Spitzer conductivity, the drift velocity is assumed to be much smaller than the thermal velocity). It is known that the Spitzer conductivity ceases to apply when the heat flow approaches that of Q_{free} [Malone et al., 1975; Bell et al., 1981; Matte and Virmont, 1982].

2.3.5 Magnetic Fields

First of all it is interesting to show that the return currents, \mathbf{j}_t , and fast electron currents, \mathbf{j}_f , must balance out also locally, i. e. $\mathbf{j}_f = -\mathbf{j}_t$ to a good approximation at every point. Let us assume that the fast electrons enter the target normally and uniformly in a cylinder of radius r_f ; the same can be done for the thermal electrons, in this case $r_t = r_f + \Delta r$. Both beams have the same current \mathbb{I} . Writing $j_f = \mathbb{I}/\pi r_f^2$ and $j_t = \mathbb{I}/\pi r_t^2$ the magnetic field is:

$$B = \frac{\mu_0 \mathbb{I}}{2\pi} \begin{cases} r \left(\frac{1}{r_f^2} - \frac{1}{r_t^2} \right) & \text{if } r < r_f, \\ \frac{1}{r} - \frac{r}{r_t^2} & \text{if } r_f < r < r_t, \\ 0 & \text{if } r_t < r. \end{cases} \quad (2.12)$$

With the assumption that $\Delta r \ll r_f$, $B_{max} = \mu_0 \mathbb{I}(\Delta r/r_f)/\pi r_f$. The magnetic energy per unit length stored in the cylinder is $\mu_0 \mathbb{I}^2(\Delta r/r_f)^2/4\pi$. With $r_f = 10\mu\text{m}$ and $\mathbb{I} = 200\text{ MA}$, $B_{max} = 8 \times 10^4(\Delta r/r_f)\text{ MG}$ and the magnetic energy per unit length becomes $10^3(\Delta r/r_f)^2\text{ J } \mu\text{m}^{-1}$. The magnetic energy cannot be larger than the absorbed energy: therefore $\Delta r \ll r_f$, i. e. the two beams are almost overlapping.

In [Davies et al., 1997] a simple formula is given to calculate the peak magnetic field due to fast electrons at the target surface, considering the conductivity as a constant:

$$B_{max} \approx 230 \left(\frac{5 \times 10^5 \Omega^{-1}\text{m}^{-1}}{\sigma} \right) \left(\frac{2\tau}{1\text{ ps}} \right) \left(\frac{10\mu\text{m}}{R} \right) \left(\frac{\eta}{0.3} \right) \left(\frac{I}{10^{17}\text{ W/cm}^2} \right)^{2/3} \left(\frac{1\mu\text{m}}{\lambda} \right)^{2/3} \text{ T}, \quad (2.13)$$

where τ is the laser pulse duration and R the laser spot radius. With our laser parameters one gets $B_{max} \approx 3\text{ kT}$ or 30 MG . In the same work the interaction between the magnetic field and the fast electrons was shown: in the simulation the magnetic field in the target could bend the electron trajectories and refocus them at the back side. Furthermore they attributed, like [Sentoku et al., 2002; Adam et al., 2006], the halo observed by some authors [Reich et al., 2003; Burgess et al., 1985; Luther-Davies et al., 1987] to the magnetic fields present at the target surface: in these magnetic fields the electrons cannot penetrate in the bulk but they can move along the target surface; in this way they can be transported many hundreds μm away from the laser focus.

If we have that $\mathbf{j}_f = -\mathbf{j}_t = E/\rho$, where ρ is the resistivity of the material, by using Faraday's law $\partial\mathbf{B}/\partial t = -\nabla \times \mathbf{E}$, we can obtain:

$$\frac{\partial\mathbf{B}}{\partial t} = \nabla \times (\rho\mathbf{j}_f), \quad (2.14)$$

which can be decomposed in

$$\frac{\partial\mathbf{B}}{\partial t} = \nabla\rho \times \mathbf{j}_f + \rho\nabla \times \mathbf{j}_f. \quad (2.15)$$

The first term in the right-hand side describes the source of a magnetic field for a change of the resistivity in the target, the second term is the source due to the motion of the fast electrons (the cause of the magnetic field in the previous paragraph).

In [Bell et al., 1998] there is a discussion about the influence of layered target on the fast electron propagation. A formula is given to calculate the magnetic field in this case (Spitzer resistivity case):

$$B \approx 220 \left(\frac{|Z_1 - Z_2|}{10} \right)^{1/2} \left(\frac{T_{thermal}}{300 \text{ eV}} \right)^{-3/4} \left(\frac{z_{layer}}{10 \mu\text{m}} \right)^{-2} \left(\frac{\tau_{laser}}{\text{ps}} \right)^{-1/2} \left(\frac{T_{fast}}{200 \text{ keV}} \right)^{-1} \times \left(\frac{E_{absorbed}}{10 \text{ J}} \right) \text{MG}. \quad (2.16)$$

For a chromium layer (1.2 μm thick) deposited on nickel (Chapter 6), one gets 220 MG (or 22 kT) strong magnetic fields. The magnetization parameter M that describes the dimension of the region occupied by the magnetic fields is introduced. If $M > 1$, this region is larger than the fast electron Larmor radius and the fast electrons are magnetized. In our case $M \approx 20$: the magnetic field generates an insulating layer at the interface between the two materials and could inhibit the transport.

The first experiment showing the presence of a magnetic field generated by the interaction of a 20 ns laser pulse with a solid target was reported more than three decades ago [Stamper et al., 1971]: small coils were used as probes, connected with an oscilloscope and put close to the focal spot. A magnetic field of ≈ 500 G was measured. They suggested a thermoelectric source for this: if the gradient of the temperature, ∇T , in a hot collisional plasma is not collinear with the electron density gradient, ∇n , then a magnetic field can be created: $\partial \mathbf{B} / \partial t \propto \nabla n \times \nabla T$.

The first MG magnetic field could be detected by using a 100 ps Nd:glass laser able to reach intensities $\approx 10^{16}$ W/cm² [Raven et al., 1978]. Time and space resolved measurements were possible by exploiting the Faraday effect.

Years later, after the advent of the chirped pulse amplification and the possibility to achieve intensities in which the electrons are accelerated to energies comparable or larger than their rest mass, a PIC simulation was used to simulate the laser-plasma interaction [Wilks et al., 1992]. Magnetic fields with magnitude ≈ 250 MG (or 25 kT) were found in the overdense region around the laser focal spot. A theoretical work [Sudan, 1993] tried to model the cited results that could not be explained by means of thermoelectric

effect. The possibility to create a “dc” (or quasi-static, in opposition to the fast oscillating magnetic field of the driving electromagnetic wave) magnetic field was shown. The origin lies with the electrons expelled in the forward direction by the ponderomotive forces of the laser pulse and piled up: this creates an average electron current that lasts as long as the laser pulse is increasing in amplitude. Problems with this model were immediately recognized (in the previous simulation the magnetic field peaked well behind the plasma vacuum interface, much deeper than predicted in this model) and a possible solution was indicated in the hot electrons flowing perpendicularly to the plasma-vacuum interface.

Something similar was suggested in [Tripathi and Liu, 1994]: let a short laser pulse propagate along the direction of density gradient, $\nabla n \parallel \hat{z}$, and the laser intensity have a variation along \hat{x} . The laser ponderomotive force $\propto \nabla I$ (where I is the intensity) imparts on the electrons a drift velocity $\mathbf{v} \parallel \hat{x}$. The produced electron current density $\mathbf{J} = -n(z)e\mathbf{v}$ is irrotational ($\nabla \times \mathbf{J} \neq 0$) and gives rise to a quasistatic magnetic field along $\nabla I \times \nabla n$. This explanation was also used to interpret the results obtained in another simulation work [Mason and Tabak, 1998]; there the ponderomotive force could be, during the run, left off: in this case the magnetic field was a factor 4 lower and confined in a thin layer in the underdense plasma region.

In [Borghesi et al., 1998a,b] a 4 MG (or 400 T) magnetic field was measured by means of the Faraday effect; [Sandhu et al., 2002] detected a 25 MG (or 2500 T) peak magnetic field with excellent temporal resolution by exploiting the ellipticity changes in the probe beam; [Tatarakis et al., 2002] could attribute the induced high harmonics suppression to a 350 MG (or 35 kT) magnetic field. All these experiments employed optical methods in the visible range, allowing only for measurements of magnetic fields present at the plasma–target interface.

Indirect evidence of the presence of magnetic fields inside the target was experimentally given by [Tatarakis et al., 1998; Gremillet et al., 1999; Borghesi et al., 1999]. The first one detected the presence of a plasma plume (very small, $\leq 10\mu\text{m}$) on the back side of a 200 μm thick plastic target. The only possibility to explain it, was to assume that a magnetic field has guided the electrons through the target. The other two experiments, very similar,

observed with time resolution, the propagation of electron jets through transparent targets (glass or plastic). Here the explanation given was the same.

In a series of simulations [Evans, 2006] a number of possible experimental conditions were explored with the help of the implicit hybrid PIC commercial code LSP. There the presence of a prepulse increased the magnetic fields by a factor of 5. This can be explained in terms of resistivity change at the plasma-target interface (a sort of buried layer with different resistivity).

2.3.6 Weibel and other instabilities

The Weibel instability [Weibel, 1939], filamentation and the two-stream instability [Bret et al., 2005] are strictly connected to each other and, together, have a strong influence on the behaviour of the fast electrons in the target. The basic idea is that two counter propagating streams of electrons (fast current and return current) are not stable because of the repulsion forces between them. Results of a PIC simulation [Sentoku et al., 2003] are reported in Fig. 2.4. After short time (some fs) from the perturbations on the surface of the plasma small ring-like structures emerge from the noise around the focal spot and, at later times, coalesce in larger filaments. The peak of the wave number spectrum is $k_y c / \omega_{pe} \approx 1 \dots 2$, where k_y is the wave number of the perturbation parallel to the target surface and ω_{pe} is the plasma frequency; this value shifts to lower values at later times [Sentoku et al., 2000]. The growth rate, in [Tatarakis et al., 2003] is given by:

$$\gamma = \omega_{pe} \beta_b \sqrt{\frac{n_b}{\gamma_b n_e}}, \quad (2.17)$$

where n_b/n_e is the ratio of the beam density to the background plasma density, v_b is the beam velocity, $\beta_b = v_b/c$ and γ_b is the relativistic Lorentz factor of the beam, but for a more complete view see [Bret et al., 2005]. Inside the filament (diameter of the order of one μm) the magnetic field is between 1 kT and 20 kT depending on the different conditions of the simulations [Honda et al., 2000; Sentoku et al., 2002, 2003].

In connection with the Weibel instability there are often calculations concerning the Alfvén limit [Alfvén, 1939]. Its value is $\mathbb{I} = mc^3/e\beta_b\gamma_b = 17\beta_b\gamma_b$ kA and it is the maximum

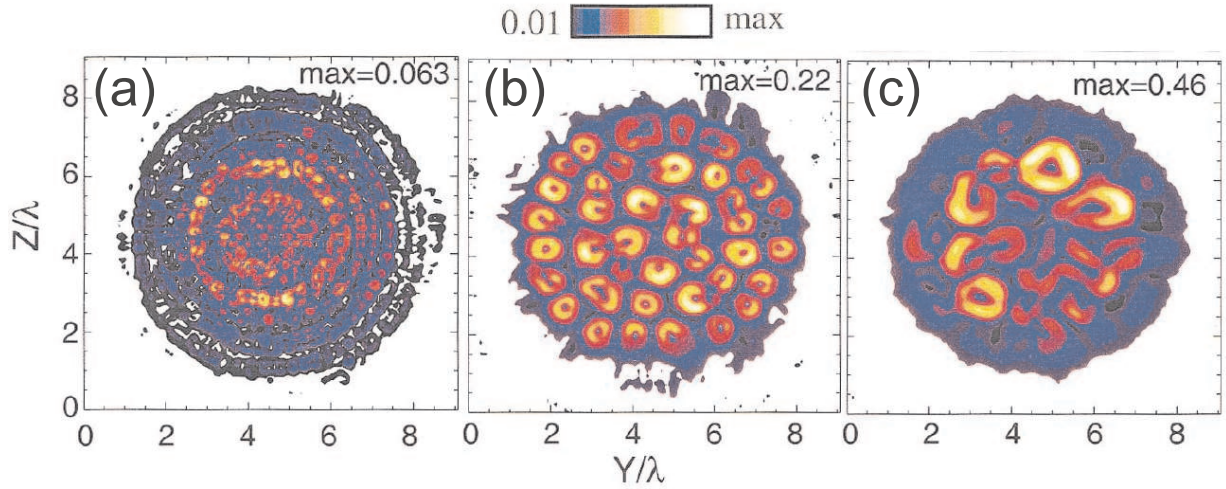


Figure 2.4: Evolution of the magnetic field driven by instabilities at different times. Figure taken from [Sentoku et al., 2003]. The magnetic field is shown in units of B_0 , the oscillating laser magnetic field. The cross sections, parallel to the target surface, are all at a distance of $2.9 \mu\text{m}$. The laser pulse is semi-infinite and reaches its maximum after 7.5 fs. Plot (a) refers to $t = 12.5$ fs, (b) $t = 37$ fs and (c) $t = 62$ fs.

amount of current that can be transported by a beam before it becomes unstable (the magnetic field is too high: at this limit, if an electron is added to the beam, it describes a 8-like trajectory without net motion). The fast ignitor scheme involves the transport of an amount of relativistic electrons exceeding this limit by orders of magnitude. Simulations shows that the current transported by a single filament is smaller than the Alfvén limit: if two beams coalesce and the sum of the current is larger than this limit, the exceeding magnetic energy is converted in transverse heat [Honda et al., 2000; Sentoku et al., 2002].

2.4 Satellites

The aim of the experiment described in Chapter 4 was to measure the magnetic field produced by the interaction of fs laser pulses with solid matter. The line broadening caused by the Zeeman effect amounted to 0.5 eV. The presence of other possible sources

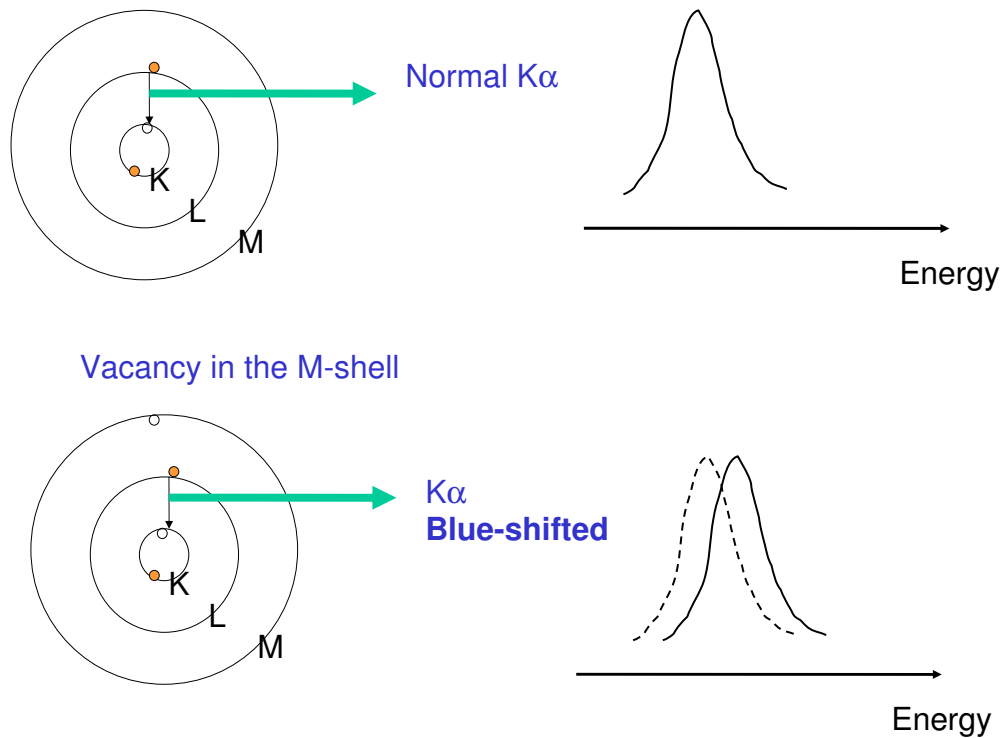


Figure 2.5: Schematic representation of the creation of a $K\alpha$ satellite.

of line broadening had to be considered and taken into account: the presence of satellites in the spectra was carefully analysed and, in some cases, could be excluded. We want now to describe what satellites are and how they are created.

[Compton and Allison, 1954] assigns the first observation of a “non-diagram line” to [Siegbahn and Stenström, 1916]. These lines are often close to strong diagram lines and hence are frequently referred to as satellites. Their origin is sketched in Fig. 2.5. If, during the process of recombination (and $K\alpha$ emission, in our case), a vacancy is present in the M-shell, then the emitted line will be blue-shifted.

To understand better the physics involved in the specific case of titanium, we report in Fig. 2.6 some calculation performed by Moshe Deutsch and Ruth Sharon from the Bar-Ilan University (Israel) for the case of $K\alpha$ transitions. The idea behind is that the $K\alpha$ line shape is a mixture of many transitions; each of them leave a track on the final line shape. The results were obtained by means of a multiconfigurational relativistic Dirac-Fock code that is

able to solve the approximated Hamiltonian of an isolated atom, given an initial and a final electronic configuration. Relativistic corrections are taken into account. Let us consider for example the “stick” diagram (b) (the height of the vertical lines gives the intensity of the allowed transitions involved, their position the transition energy): the external electronic configuration of a neutral titanium atom (described in the upper left corner) is considered and, rather counterintuitively, many transitions contribute to the $K\alpha$ radiation. Many other different external electronic configurations are taken into account. We note also that the stick diagrams labeled with (g), (h) and (i) show a blue shift, compared with the measured spectrum (a). They involve the presence of a vacancy in the 3p-shell or M-shell (called 3p “spectator” in the graph). The (f) plot, with 3d spectator, shows a red shift: even if the atom lost some electrons and is positively charged, the $K\alpha$ transition had a lower energy. Anyway, in our measurements, we couldn’t observe any hint of red shift due to satellites.

The code has an accuracy not better than 2–3 eV for the energy. Moreover, it is not clear, in principle which configuration is involved. In [Deutsch et al., 1995], for Cu, it is shown that 4 configurations are involved with different weights. The procedure of the analysis used in that paper is the following: the position of the group of sticks, or multiplet, (one multiplet for $K\alpha_1$ and one for $K\alpha_2$) can be varied and is taken as a free parameter, the same happens for the intensity (each group is taken as a whole) and the line width (every stick line has the same common line width of the other sticks belonging to a group). A high resolution spectrum of $K\alpha_1$ and $K\alpha_2$ is acquired at the X-ray tube. A fitting routine is applied to the calculated spectrum in order to reproduce the measured spectrum. The free parameters are obtained; in particular the intensity gives the importance of a single multiplet to the final line shape.

For M-shell holes the line shift amounts to $\approx 2\text{--}3$ eV per vacancy [Hill et al., 1976; Zschornack; Mokler and Folkmann, 1978]. For L-shell vacancies in Ti it is about 25 eV per missing electron. The removal of the first four electrons of the outer shell ($4s^2 3d^2$) causes a line shift of about 0.5–1 eV. The uncertainty comes from the fact that, at least for M-shell holes, there are no clean measurements, because the satellite lies too close to

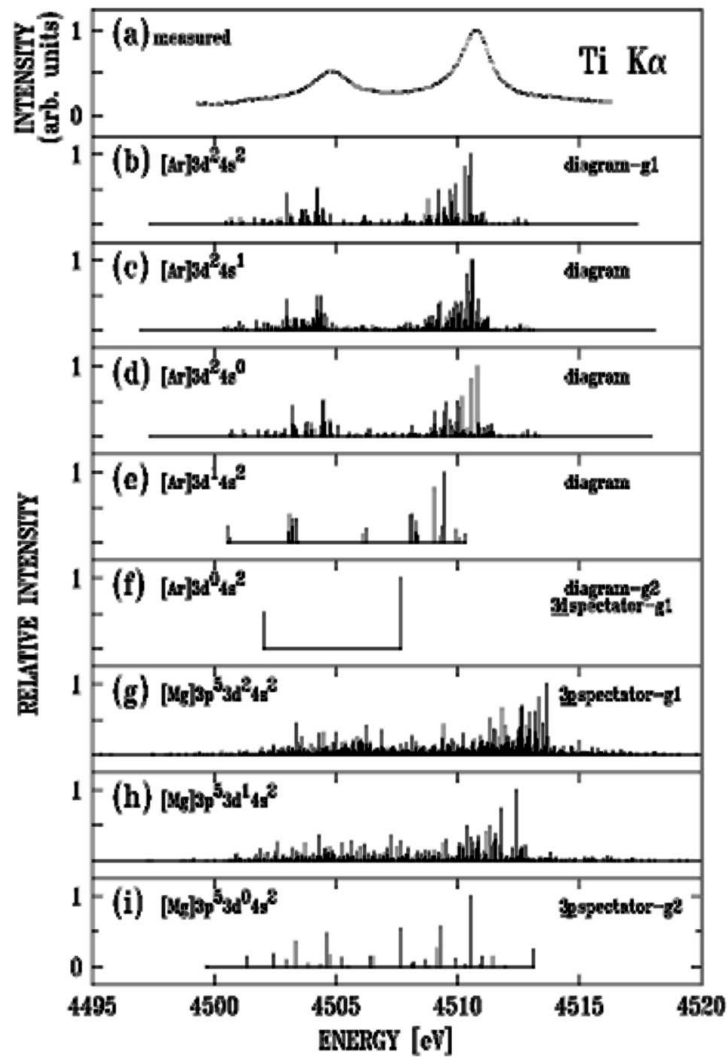


Figure 2.6: Relativistic multiconfigurational Dirac-Fock calculations for the $K\alpha$ transitions in an isolated titanium atom. In (a) the measured spectrum. In (b) to (i) many possible electronic configurations are taken into account and the corresponding “stick” diagrams are plotted.

the diagram line to be independently resolved ⁴.

⁴One could measure a “line shift” if all the atoms had the same amount of vacancies: this is obviously not the case, there is a population and what can be measured is a shoulder on the blue side of the diagram line, like e. g. in Fig. 5.5 of Chapter 5. There we talk about line shift: what is meant is that, by fitting the $K\alpha$ lines with Lorentz functions, the presence of a more or less large shoulder can “pull” the fitting function in the blue direction. It is no real blue shift.

In [Deutsch et al., 2004] the evolution of satellites from threshold to saturation is followed and the asymmetrical shape of copper $K\alpha$ can be attributed to the presence of satellites (the line shape is symmetrical just over threshold). Something similar for titanium can be found in [Shigeoka et al., 2004]. Unfortunately, in this reference, not all the satellites are taken into account but only the so-called Ti- $K\alpha''$. Ti satellites has been recently investigated with a laser-plasma source [Hansen et al., 2005] and they were used to obtain an estimation of the plasma temperature.

2.5 Spectropolarimetry

Spectropolarimetry is the measurement of spectra in dependence of the polarization.

The presence of a magnetic or electric field offers the simplest case of a possible influence on the polarization features of radiation. In the case of plasma particles having an anisotropic velocity distribution (this case will be of interest for the present work) one has an anisotropic excitation. The idea is that the excited atom keeps a sort of memory of the direction of the collision by which it was produced and presents its memory in form of polarization of light it emits [Fujimoto and Kazantsev, 1997].

The technique is sensitive to anisotropies in the radiating and transmitting media. The comparison of spectra acquired with different polarizations can provide an insight into anisotropies of the electron distribution function. We sketched in Fig. 2.7 the ideas of the review paper [Fujimoto and Kazantsev, 1997]. Let us consider an electron flying in the \hat{z} direction and colliding with a classical atom (ion core and an electron connected by a harmonic force). If the energy of the electron is just enough to excite the atom, the atomic electron will start to oscillate in the \hat{z} direction. The emission will be a dipole emission, polarized in the \hat{z} direction, if seen in the x - y plane (π polarization). Let us consider the other extreme case, the electron passes by the atom with high energy: now the atom experiences a pulsed electric field directed in the x - y plane. This pulse may be approximated by a half cycle of an electromagnetic wave propagating in the \hat{z} direction. The photo-excited atomic electron will oscillate in the x - y plane and the radiation will be

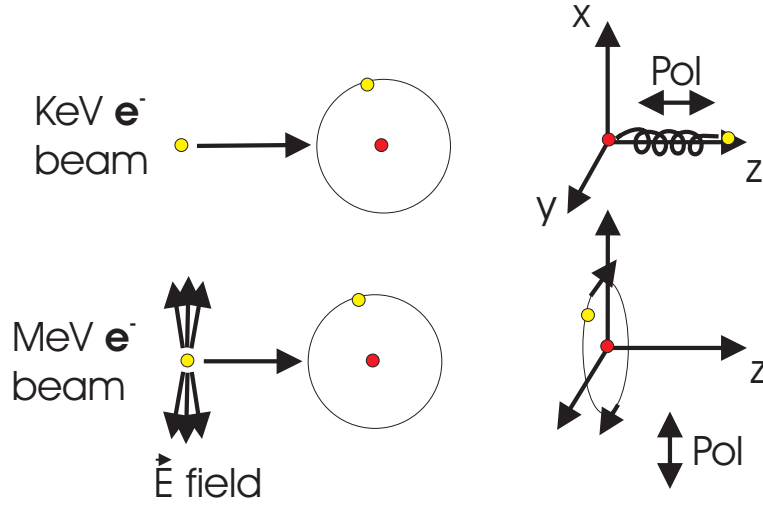


Figure 2.7: *The working principle behind the spectropolarimetry.*

σ polarized.

In the first case the degree of linear polarization $P = (I_\pi - I_\sigma)/(I_\pi + I_\sigma)$ will be $P \approx 1$. In the second case it will have a lower value. In the limit of very high energy it will be $P \approx -1$.

The basic idea behind the spectropolarimetry is to measure the linear polarization degree of the radiation to obtain information about the electron velocity distribution (EVD) that caused this kind of emission. The process is not straightforward as it could appear, because there are many free parameters in play.

To show how the different parts are connected, I'll follow the theoretical approach suggested in [Walden et al., 1999]. This description is valid in the absence of electric and magnetic fields.

Let us consider a plasma with a beam-like electron distribution function parallel to \hat{z} . The emitting ions will be excited by collisions with unpolarized electrons governed by a distribution function $f(\mathbf{v})$ (\mathbf{v} is the velocity) or, in terms of energy and pitch angle, by:

$$f(\epsilon, \alpha) = (1 - n_{fast})f_t(\epsilon)f_0 + n_{fast}f_{fast}(\epsilon, \alpha), \quad (2.18)$$

where the subscript *fast* and *t* refer to fast (anisotropic) and thermal (Maxwellian) elec-

trons, $f_0 = \frac{1}{4\pi}$, $\cos \alpha = \frac{\mathbf{v} \cdot \hat{\mathbf{z}}}{v}$, the energy ϵ is in excitation energy units $\epsilon = E/E_{ex}$ and α is the pitch angle that characterizes the fast electron anisotropic distribution. There are some normalization factors:

$$\begin{aligned} f_{fast}(\epsilon, \alpha) &= f_{fast}(\epsilon)f(\epsilon, \alpha), \\ \int_0^\infty f_{fast}(\epsilon)d\epsilon &= 1, \\ 2\pi \int f(\epsilon, \alpha)d\mu d\epsilon &= 1, \\ \mu &= \cos \alpha. \end{aligned} \tag{2.19}$$

We have $n_{fast} = N_{fast}/N_e$, with $N_{fast} + N_t = N_e$, where n_{fast} is the relative density of the fast electrons ($n_{fast} \ll 1$; this is not necessarily the case, but to simplify the calculation it will be assumed to be true) and N_e is the total electron density.

Expanding the pitch angle distribution function in Legendre polynomials $P_l(\mu)$ one can rewrite eq. 2.18:

$$\begin{aligned} f(\epsilon, \alpha) &= \tilde{f}(\epsilon)f_0 + \bar{f}(\epsilon, \alpha)f_2 \quad \text{with} \quad f_2 = 5f_0, \\ \tilde{f}(\epsilon) &= (1 - n_{fast})f_t(\epsilon), \\ \bar{f} &= n_{fast}f_{fast}(\epsilon) \sum_{l=2}^{\infty} \bar{f}_l(\epsilon)P_l(\mu), \\ \bar{f}_l(\epsilon) &= \frac{2l+1}{2f_2} \int_{-1}^1 f(\epsilon, \alpha)P_l(\mu)d\mu. \end{aligned} \tag{2.20}$$

If we consider, for example, a beam-like electron distribution with $f(\epsilon, \alpha) = 1/(2\pi)\delta(1-\mu)$, (δ is the Dirac delta) we obtain $\bar{f}_2 = 1$; in general it will depend on the energy of the incident electrons.

For the limit case of lines excited by an electron beam the degree of polarization P can be expressed through cross sections for the excitation of the m states (magnetic levels), averaged over the electron distribution function eq. 2.20 with $n_{fast} = 1$:

$$\bar{P} = \frac{\langle v\sigma_0(\epsilon, \alpha) \rangle - \langle v\sigma_1(\epsilon, \alpha) \rangle}{\langle v\sigma_0(\epsilon, \alpha) \rangle + \langle v\sigma_1(\epsilon, \alpha) \rangle}, \tag{2.22}$$

where the $\sigma_i(\epsilon, \alpha)$ are the excitation cross sections for the m states relative to the quantization axis rotated by the angle α with respect to the vector \hat{z} . Transforming the cross sections for rotations about the quantization axis, one can rewrite \bar{P} as follows:

$$\bar{P} = \frac{3\tilde{P}\beta}{3 - \tilde{P}(1 - \beta)}, \quad (2.23)$$

\tilde{P} is the degree of polarization of a beam-like electron distribution and β is:

$$\beta = \frac{\int v [\sigma_0(\epsilon) - \sigma_1(\epsilon)] f_{fast}(\epsilon) \bar{f}_2(\epsilon) d\epsilon}{\int v [\sigma_0(\epsilon) - \sigma_1(\epsilon)] f_{fast}(\epsilon) d\epsilon}. \quad (2.24)$$

In a plasma we have to consider also an isotropic part of the distribution function: the cross section have to be averaged also over the Maxwellian part and the m states population from other processes has to be taken into account. Assuming an isotropic character of the population we have:

$$P = \frac{3\bar{P}g}{3 - \bar{P}(1 - g)} \quad \text{with} \quad g = \frac{\langle v\sigma \rangle_{fast}}{X}, \quad (2.25)$$

where σ is the cross section summed over all the m states and X is the total rate of excitation of the J level.

For both eqs. 2.23 and 2.25 there are two factors, β and g , which lead to a decrease of the polarization degree P . The first is connected with the width of the anisotropic distribution function through the pitch angle α and the second is connected with the relative contribution of the non-thermal electrons to the total population of a J level. In other words: \tilde{P} is the polarization degree for a perfect beam-like distribution function ($\alpha = 0$ and $n_{fast} = 1$), \bar{P} is the polarization degree for an anisotropic distribution function with some pitch angle ($\alpha \neq 0$ and $n_{fast} = 1$): this can be seen in the presence of \bar{f}_2 in the expression for β ; if $\bar{f}_2 = 1$, i. e. perfect beam, $\beta = 1$ and $\bar{P} = \tilde{P}$. P is the polarization degree if we consider also the Maxwellian part of the distribution: if $g = 1$, we have only fast electrons contributing to the population and $P = \bar{P}$.

At this point a form for \bar{f}_2 is needed: in our case it should come from a code simulating the laser-plasma interaction. Temporal evolution of the electron density, temperature and beam-like features of the electron distribution [Hakel et al., 2004] have to be taken

into account. Moreover, all the terms contributing to the σ for the excitation process (collisional, radiative) must be considered with time dependence. The evolution of all these contributions are then put together to give the intensity of the polarized components of the spectrum, time integrated to be directly comparable with the measurements.

Chapter 3

The X-ray spectrometer

3.1 Introduction

A high resolution X-ray spectrometer was developed to be able to discern an even small line broadening due to the influence of the Zeeman effect on the $K\alpha$ lines: the Zeeman energy splitting, $\Delta E \sim \mu_B B$ (where μ_B and B are the Bohr magneton and the magnetic field, respectively) with a magnetic field of some kT (not commonly available in laboratory) is of the order of 0.1 eV. A high energy resolution is then an essential condition for the success of the experiment.

In order to be able to distinguish the contribution of the magnetic field from other possible sources of line broadening, a polarizer was coupled with the spectrometer in a non-dispersive setup. In this way the components σ , more sensitive to the magnetic field, can be partially filtered out. A direct comparison (like in [Sarfaty et al., 1995]) polarized vs. nonpolarized spectra can allow a precise estimation of the amount of the magnetic field involved in the measurements.

3.2 Principle of the spectrograph

Different types of spectrographs using crystals as wavelength dispersive element are known. They are using flat crystals, cylindrically bent ones, i.e. Johann, von Hámos, a vertical variant of Johann spectrograph [Johann, 1931; Johansson, 1933; Kopecky, 1995], or spherically bent crystals [Faenov et al., 1994]. To achieve a spatial resolution in addition to the

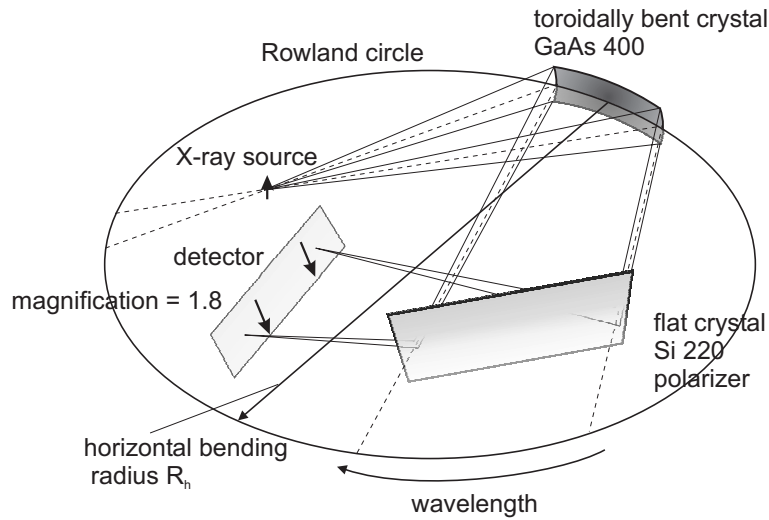


Figure 3.1: The spectrometer setup is sketched in the figure. The flat crystal, working as a polarizer, could be removed allowing the focusing of the nonpolarized spectrum on the Rowland circle.

spectral resolution the Johann, von Hámós and the spherically bent crystal setups use a slit along the dispersion direction to image the plane perpendicular to the dispersion plane. The slit is positioned between radiating source and the crystal. The ratio of the distances from the slit to the detector and from the source to the slit defines the magnification factor. For all these spectrometers the spatial resolution is limited by the slit width. The smaller the slit, the better the resolution but as a consequence the lower the luminosity of the instrument.

As an alternative spectrometer an imaging spectrograph using a toroidally bent crystal is presented here. This type of spectrometer provides an 1D spatial resolution in combination with a high spectral resolution and high luminosity.

The first use of toroidally bent crystals has been made to increase the spatial resolution in monochromatic imaging [Förster et al., 1991] or to increase the luminosity by focusing the X-ray spectrum to a line [Hauer et al., 1985]. In comparison to a spherical surface, the toroidal surface has the advantage of having two different focal lengths, the horizontal one f_{hor} and the vertical one f_{ver} , corresponding to the two radii of curvature R_{hor} and R_{ver} .

These quantities are connected to each other by:

$$f_{hor} = \frac{R_{hor}}{2} \cdot \sin \theta_0, \quad f_{ver} = \frac{R_{ver}}{2 \cdot \sin \theta_0},$$

where θ_0 is the Bragg angle. If the bending radius in the dispersion plane is larger than the bending radius perpendicular to the dispersion plane, the angle $\bar{\theta}$ for a reduced astigmatic image is defined by:

$$\frac{R_{ver}}{R_{hor}} = \sin^2 \bar{\theta} \quad (3.1)$$

This angle delivers the same focal distance in the dispersion plane and in the plane perpendicular to it, i. e. $f_{hor} = f_{ver}$. It means that each spatial source element is imaged in the image plane of the source. By an angular deviation from the reflection angle $\bar{\theta}$ one gets two focused lines of each source point caused by astigmatism.

Independently of the geometry of the setup the radiation is dispersed into a spectrum which is focused horizontally by the crystal with bending radius R_{hor} near the Rowland circle with a distance to the crystal:

$$l_b = R_{hor} \sin \theta_0.$$

In order to use the crystal as a spectrometer, the source was moved inside the Rowland circle (as shown in Fig. 3.1). For a small source the different wavelengths are reflected at different positions on the surface of the GaAs bent crystal and collected by the detector put on the Rowland circle. As already mentioned R_{ver} was chosen such that an 1D imaging in the vertical direction could be achieved.

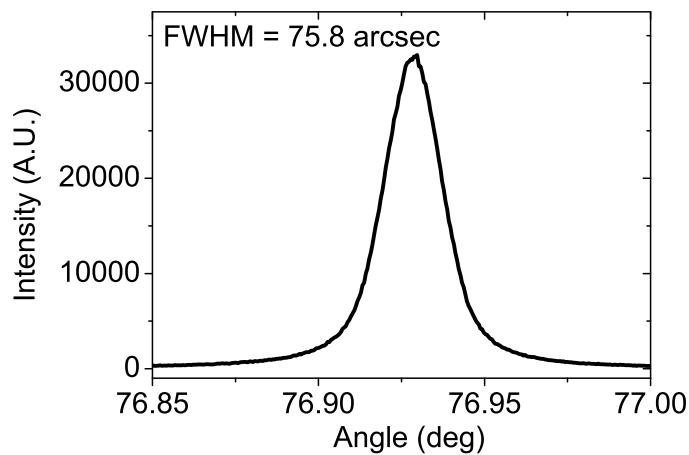
3.3 Spectral and spatial properties

In this section experimental conditions are investigated for a situation where a point source is placed inside the Rowland circle. In this case different wavelengths are reflected at different portions of the crystal, according to the Bragg equation. Basis equations of the

Table 3.1: Data concerning the spectrometer and the X-ray radiation used in the experiment.

We note that in our case $M_v = 1.8$.

Reflection	R_{ver}	R_{hor}	l_a	l_b	θ_{bent}	Reflection	θ_{flat}	Ti-K α_1	Ti-K α_2
GaAs 400	[mm]	[mm]	[mm]	[mm]	[°]	Si 220	[°]	[eV]	[eV]
	305.9	450	244.9	441	76.7		45.7	4510.84	4504.86

**Figure 3.2:** Convolution of the rocking curves of two identical flat GaAs crystal (400) reflections measured with a (n , $-n$) setup and a Ti-K α source.

angular distribution on the toroidally bent surface were given in [Förster, 1985; Missalla et al., 1999]. In Table 3.1 the data concerning the spectrometer are reported.

The difficulty to find a perfect GaAs crystal motivated a careful characterization to find out which role the crystal imperfections play and what influence on the rocking curve they have. In order to extract information about the spectral resolution, a measurement was performed with a double crystal spectrometer by using two identical flat GaAs crystals with (100) orientation with the same dislocation density ($n \simeq 6 \cdot 10^5 \text{ cm}^{-2}$) as the crystal used in the spectrometer. The double crystal spectrometer measures the convolution of the two rocking curves. The measurements are shown in Fig. 3.2. From this, through a deconvol-

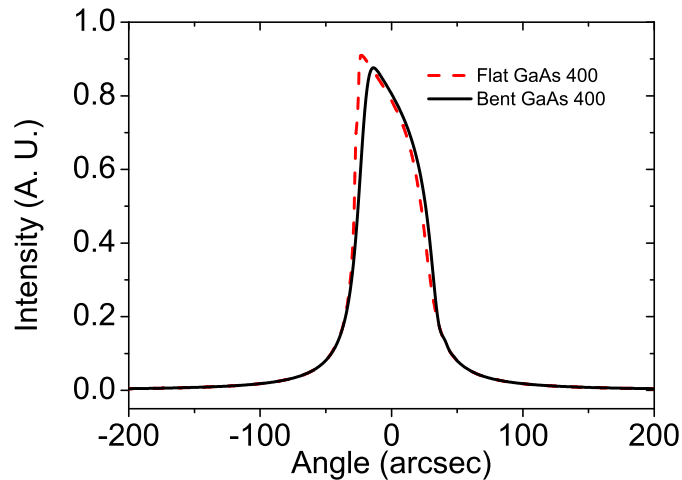


Figure 3.3: Calculated rocking curves for flat and toroidally bent GaAs (400) crystals. For calculations concerning the bent crystal the same parameters of the spectrometer crystal were used. Differences in the FWHM amount to less than 2.5%.

lution, a FWHM = 55 arcsec for the rocking curve can be calculated. Calculations¹ show that the large radius of curvature used for the GaAs (400) does not change significantly the width of the rocking curve if compared to a flat crystal, as reported in Fig. 3.3.

The difference between the measured rocking curve and the theoretical one obtained assuming a perfect crystal amounts to 4%. From the FWHM of the measured rocking curve a spectral resolution $\Delta\lambda/\lambda \simeq 15000$ can be deduced.

Combining the fact that one detects a spectrum on the Rowland circle with the fact that by choosing the appropriate R_{ver} a 1D imaging can be obtained, it is possible to have spatial resolution of the source in the vertical direction. This is achieved without using any slit or aperture in the optical path. To know the position of the source with respect to the crystal one has to use the lens equation $1/l_a + 1/l_b = 1/f$, with $l_b = R_{hor} \sin \theta_0$ and $f = f_{ver}$.

¹In this thesis the rocking curves were all calculated by means of the code DIXI of G. Hölzer

Then the distance from the X-ray source to the crystal is fixed by:

$$l_a = R_{hor} \sin \theta_0 \frac{1}{2 \frac{\sin^2 \theta_0}{\sin^2 \theta} - 1} \quad (3.2)$$

By using a toroidally bent crystal, magnification and Bragg angle can be chosen independently; moreover it is possible to achieve magnifications larger than one. The magnification can be calculated by:

$$M_v = \frac{l_b}{l_a} = 2 \frac{\sin^2 \theta_0}{\sin^2 \theta} - 1.$$

Because the imaging distance is always the distance to the Rowland circle there is no free choice of magnification independently of the spectral window being reflected for a fixed vertical bending radius.

Experiments using spherically bent crystals have already been made [Faenov et al., 1994; Young et al., 1998]. With spherically bent crystals only a few experimental conditions can be accessed. Because of the identical radii $R_{hor} = R_{ver}$, putting Eq. (3.1) and (3.2) together, the distance to the source is given by the optic:

$$l_a = \frac{R_{hor} \sin \theta_0}{2 \sin^2 \theta_0 - 1}$$

But a different magnification using the same crystal material implies that a different spectral range is reflected. Even further, by looking closely at the equation one can see that only magnification ratios smaller than one are accessible with a spherical crystal because of the condition

$$M_v = \frac{l_b}{l_a} = 2 \sin^2 \theta_0 - 1.$$

Moreover an angle $\theta_0 > 45^\circ$ is required to obtain a vertical image at all.

The limit for demagnified imaging is given by the spectral window of the illumination of the crystal by parallel light. The torus has to have a ratio of the bending radii with $R_{ver}/R_{hor} < 2 \sin^2 \theta_0$. The spectral window for magnified imaging is not limited by geometric reasons but usually there is a minimal safety distance from crystal to plasma to protect the crystal from debris.

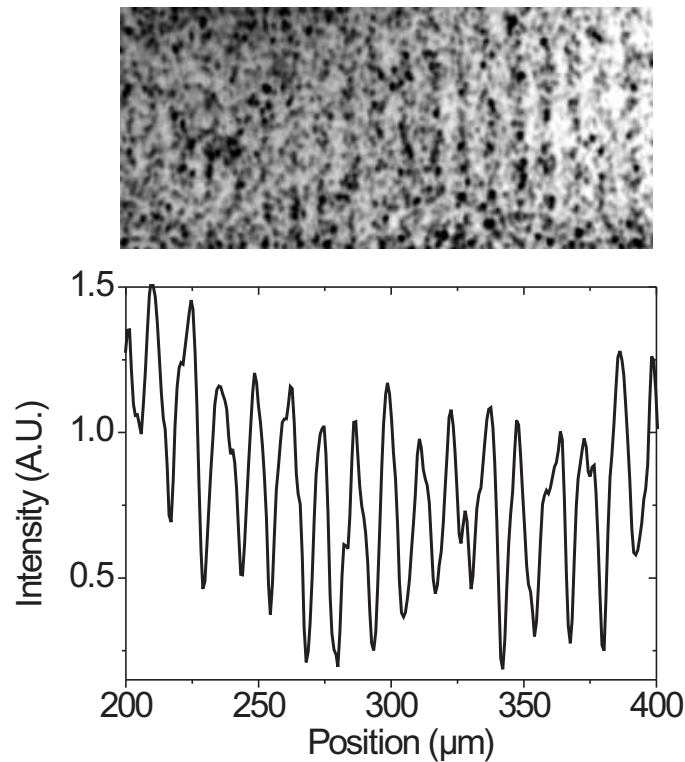


Figure 3.4: Upper panel: a 1D image of a mesh with a constant of $12.5 \mu\text{m}$. Lower panel: intensity profile of the 1D image of the same mesh. The resulting spatial resolution is about $4 \mu\text{m}$.

The spatial resolution of the spectrometer used in the experiment was tested by putting a $12.5 \mu\text{m}$ mesh in front of the source, an X-ray tube. In Fig. 3.4 the results are shown. The upper part is a 2D scan of the film: vertical modulations are clearly visible. By summing up several lines the signal to noise ratio can be improved: the lower part of the figure shows the lineout. To calculate the spatial resolution, the copper mesh was assumed to be completely absorbing for Ti- $K\alpha$ radiation. The image of the mesh, assumed to be composed by rods with squared cross section, would give, in case of infinitely high resolution, a square function, i. e. a series of flat maxima and minima. The first derivative would be a series of Dirac delta functions. In the real case the transition between maxima and minima is not so steep anymore because the finite resolution smears the contours.

The first derivative of the lineout is composed by peaks with a finite FWHM. We used the value of the measured FWHM as spatial resolution of the spectrometer. We note that the assumptions used in the calculations (completely absorbing rods, perfectly squared rods) are best case assumptions. If they are not satisfied, the calculated final resolution is worse than the real one. The spectrometer spatial resolution obtained with this method amounts to 4 μm .

3.4 Non-dispersive setup

In addition to the bent GaAs crystal, a second crystal, a flat Si (220), could be coupled in a non-dispersive setup, i.e. this second crystal was working as a diffracting element but reflecting all the wavelengths coming from the first crystal [Uschmann et al., 1993; F. N. Chukhovskii, 1992]. The total dispersion must be equal to zero. The Bragg angle of the flat crystal $\theta_{flat} = 45.7^\circ$ allowed almost only the reflection of the σ -polarized part of the radiation.

A general and authoritative discussion about double flat crystal spectrometers is given in [Compton and Allison, 1954].

The non-dispersive setup sets some constraints on the positions of source, crystals and detector. Given R_{hor} , the horizontal radius of curvature and θ_0 , the Bragg angle, the remaining parameters l_a , l_b and R_{ver} , the distance source-crystal, the distance crystal-detector and the vertical radius of curvature, respectively, are fixed.

The main steps of such a calculation are shown in the following.

From [Missalla et al., 1999], let us consider the rocking curve of the crystal, i. e. the function $C[\sigma(\alpha, \Phi) - \Delta\lambda/\lambda_0 \tan \theta_0]$, where $\sigma(\alpha, \Phi) = \theta - \theta_0$ is the deviation angle θ from the central Bragg angle θ_0 corresponding to different reflection positions on the crystal, λ_0 is the wavelength corresponding to the Bragg angle θ_0 , $\Delta\lambda$ is the deviation from this central wavelength, α and Φ are the horizontal (in the dispersion plane) and the vertical

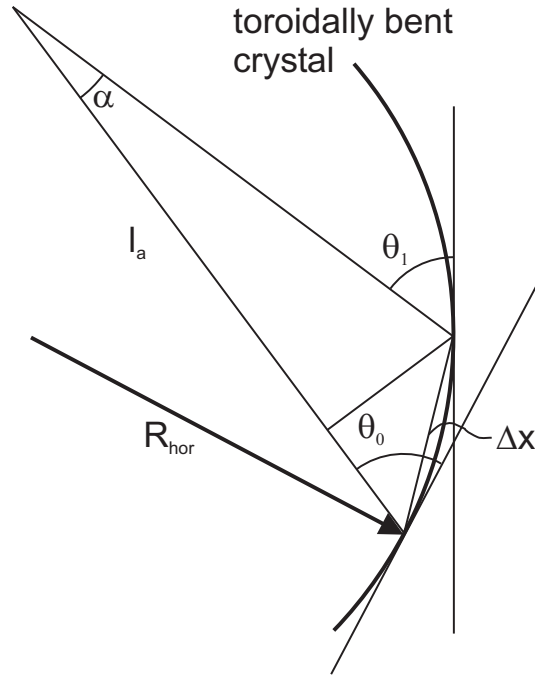


Figure 3.5: Pictorial representation of the parameters used in the derivation of a non-dispersive setup.

divergence angles. By putting

$$\sigma(\alpha, \Phi) - \Delta\lambda/\lambda_0 \tan \theta_0 = 0 \quad (3.3)$$

we look for the variations of the incident angle (or wavelength) in dependence of the position on the crystal. We can use the first order approximation [Missalla et al., 1999]:

$$\sigma(\alpha, \Phi) \simeq \sigma(\alpha) \simeq \frac{k-1}{2k}\alpha, \quad (3.4)$$

$k = k^{hor} = \frac{l_b^{hor}}{l_a}$ can be seen as the magnification due to the horizontal bending and l_b^{hor} is the position of the image due to this bending, and $l_a = l_a^{hor}$. The lens equation can be

rewritten as

$$\begin{aligned}\frac{1}{l_b^{hor}} + \frac{1}{l_a} &= \frac{1}{f_{hor}} \\ \frac{l_a}{l_b^{hor}} + 1 &= \frac{l_a}{f_{hor}} \\ \frac{1}{k^{hor}} + 1 &= \frac{l_a}{f_{hor}},\end{aligned}\tag{3.5}$$

and finally one comes to:

$$k^{hor} = \frac{R_{hor} \sin \theta_0}{2l_a - R_{hor} \sin \theta_0}.$$

Taking Fig. 3.5 into account we can write

$$\alpha = \frac{\Delta x \sin \theta^b}{l_a},$$

the superscript b indicates that the calculations are involving the bent crystal. The subscript 0 has been omitted for sake of clarity.

Eq. (3.3) can be now rewritten to give the dispersion [Compton and Allison, 1954] for the bent crystal:

$$\frac{\Delta \lambda^b}{\lambda} = \frac{1}{\tan \theta^b} \left[\frac{\sin \theta^b}{l_a} - \frac{1}{R_{hor}} \right] \Delta x.\tag{3.6}$$

For the part concerning the flat crystal (marked with a superscript f) we can combine

$$\Delta \theta^f = \frac{\Delta x \sin \theta^b}{l_b}\tag{3.7}$$

with the lens equation

$$\frac{1}{l_a} + \frac{1}{l_b} = \frac{1}{f_{hor}},$$

where $f_{hor} = \frac{R_{hor}}{2} \sin \theta^b$ to obtain

$$l_b = \frac{l_a R_{hor} \sin \theta^b}{2l_a - R_{hor} \sin \theta^b}.$$

Substituting in Eq. 3.7 we get:

$$\Delta\theta^f = \frac{2l_a - R_{hor} \sin \theta^b}{l_a R_{hor}} \Delta x$$

and finally

$$\frac{\Delta\lambda^f}{\lambda} = \frac{\Delta\theta^f}{\tan \theta^f} = \frac{1}{\tan \theta^f} \frac{2l_a - R_{hor} \sin \theta^b}{l_a R_{hor}} \Delta x. \quad (3.8)$$

The total dispersion is the difference of the two dispersions. The non-dispersive setup is now achieved by posing the total dispersion equal to zero:

$$\frac{1}{\tan \theta^b} \left[\frac{\sin \theta^b}{l_a} - \frac{1}{R_{hor}} \right] \Delta x - \frac{1}{\tan \theta^f} \frac{2l_a - R_{hor} \sin \theta^b}{l_a R_{hor}} \Delta x = 0. \quad (3.9)$$

Now we get l_a in dependence of R_{hor} :

$$l_a = \frac{R_{hor} \sin \theta^b \left[\frac{\tan \theta^b}{\tan \theta^f + 1} \right]}{1 + 2 \frac{\tan \theta^b}{\tan \theta^f}}. \quad (3.10)$$

The vertical radius of curvature R_{vert} has now become a function of l_a and R_{hor} . It must be chosen such that the 1D imaging occurs on the Rowland circle. So we have $l_b = R_{hor} \sin \theta^b$ and applying again the lens equation $\frac{1}{l_a} + \frac{1}{l_b} = \frac{1}{f_{ver}}$ with $f_{ver} = \frac{R_{ver}}{2 \sin \theta^b}$ one obtains:

$$R_{ver} = \frac{2l_a R_{hor} \sin^2 \theta^b}{l_a + R_{hor} \sin \theta^b}$$

and applying the Eq.(3.10) finally we come to:

$$R_{ver} = \frac{2R_{hor} \sin^2 \theta^b \left[\frac{\tan \theta^b}{\tan \theta^f} + 1 \right]}{2 + 3 \frac{\tan \theta^b}{\tan \theta^f}}.$$

The data reported in Table 3.1 fulfill the requirements set by the previous formulae.

3.5 Integrated reflectivity for bent crystals

From [Missalla et al., 1999] the amount of reflected photons can be written as:

$$N_{ref} = \int_{\alpha_{min}}^{\alpha_{max}} \int_{\Phi_{min}}^{\Phi_{max}} \int_{\lambda_{min}}^{\lambda_{max}} d\alpha d\Phi d\lambda G(\alpha, \Phi) J(\lambda) C\left(\sigma(\alpha, \Phi) - \frac{\Delta\lambda}{\lambda_0} \tan \Theta_0\right),$$

where $G(\alpha, \Phi)$ is the angular distribution of the emitted energy and can be taken = 1, in our case; the angles α and Φ are the horizontal and the vertical divergence angle. $J(\lambda)$ is the energy distribution of the spectrum, $C\left(\sigma(\alpha, \Phi) - \frac{\Delta\lambda}{\lambda_0} \tan \Theta_0\right)$ is the function already described in Sec. 3.4.

By taking into account eq. 3.4, for the case of a point source not sitting on the Rowland circle, and performing a variable change $\alpha \rightarrow \Theta$, where

$$\Theta = \sigma(\alpha, \Phi) - \frac{\Delta\lambda}{\lambda_0} \tan \Theta_0,$$

with $d\alpha = 2k^{hor}/(k^{hor} - 1)d\Theta$ one gets:

$$\begin{aligned} N_{ref} &\approx \int_{\lambda_{min}}^{\lambda_{max}} J(\lambda) d\lambda \int_{\Phi_{min}}^{\Phi_{max}} d\Phi \int_{\Theta_{min}}^{\Theta_{max}} \frac{2k^{hor}}{k^{hor} - 1} C(\Theta) d\Theta \\ &\approx \frac{2k^{hor}}{k^{hor} - 1} R_{int} \int_{\lambda_{min}}^{\lambda_{max}} J(\lambda) d\lambda \int_{\Phi_{min}}^{\Phi_{max}} d\Phi \\ &\approx \frac{2k^{hor}}{k^{hor} - 1} R_{int} \frac{\Delta h_{crystal}}{l_a} \int_{\lambda_{min}}^{\lambda_{max}} J(\lambda) d\lambda, \end{aligned} \tag{3.11}$$

where $\Delta h_{crystal}$ is the crystal height in the vertical plane; the wavelength dependence in $C(\Theta)$ could be neglected under the assumption that the spectral range of the spectrometer is small enough. By substituting for $l_a = (k^{hor} + 1)/(2k^{hor})R_h \sin \Theta_0$ one finally gets:

$$N_{ref} = N_L \frac{(2k^{hor})^2}{(k^{hor})^2 - 1} \frac{\Delta h_{crystal} R_{int}}{\sin \Theta_0 R_h}, \tag{3.12}$$

where N_L is the number of photons emitted by the laser-plasma source. It's important to notice that eq. 3.12 is valid only if the spectral range of the focusing setup

$$\Delta\lambda \approx \lambda \left| \frac{k^{hor} - 1}{k^{hor} + 1} \right| \frac{\Delta s_{crystal}}{R_h \tan \Theta_0} \tag{3.13}$$

is larger than the width $\Delta\lambda_L$ of the emitted spectral bandwidth of the source; $\Delta s_{crystal}$ is the horizontal crystal dimension.

We have now to determine the value of R_{int} . The dynamical theory of the X-ray diffraction [Authier, 2003; Takagi, 1962; Taupin, 1964] gives the value for the integrated reflectivity in the case of perfect crystals:

$$R_{int} = \frac{8}{3} \frac{1}{\sin 2\Theta_0} \frac{1 + \cos 2\Theta_0}{2} \sqrt{\chi_{hkl}\chi_{\bar{h}\bar{k}\bar{l}}}, \quad (3.14)$$

where χ_{hkl} is the Fourier component of the dielectric susceptibility (the indices hkl label the reflection) and can be written as:

$$\chi_{hkl} = \frac{\lambda^2 r_e}{\pi V} F_{hkl} \quad (3.15)$$

r_e is the classical electron radius, V is the volume of the unit cell and F_{hkl} is the structure amplitude for the hkl reflection.

Chapter 4

Magnetic field measurements: Zeeman effect in the X-ray regime

4.1 Introduction

The influence of a magnetic field on transitions involving external electrons is well-known [Zeeman, 1897]; on the contrary, for inner shell electrons in medium – high Z it remained until now unexplored. Astronomical objects offered already the possibility to study exotic conditions of the matter [Trümper et al., 1978]: B-fields of the order of 10^8 T (10^{12} G) induced cyclotron transitions between Landau levels of electrons of the hot magnetized plasma of the X-11 neutron star surface. The Zeeman effect caused by magnetic fields of $10^2 \dots 10^6$ T ($10^6 \dots 10^{10}$ G) could explain unusual features of white dwarfs visible light spectra [Kemic, 1974]. However, presently, only H and He spectra can be calculated for $B \approx 10^2 \dots 10^4$ T ($\approx 10^6 \dots 10^8$ G). The strongest magnetic fields $B \approx 10^{10} \dots 10^{11}$ T ($10^{14} \dots 10^{15}$ G) are believed to be caused by the sudden gravitational collapse of neutron stars in which in short time the rotational energy is transformed in magnetic energy [Duncan and Thompson, 1992]. On earth, the effect of a magnetic field on the soft X-ray emission from atoms has been reported: the emission of an otherwise strictly forbidden line has been induced by a 3 T (30000 G) magnetic field. The highest magnetic fields available in lab are of the order of 1000 T (10^7 G) produced by flux compression, in which a seed field (about 2 T) is compressed by an imploding metal liner (copper ring), triggered electromagnetically or by chemical explosives [Kane et al., 1997].

The production of magnetic fields of the order of tens of kT [Tatarakis et al., 2002] in

lab has become possible only few years. This is achieved by using laser-produced plasmas. By focusing ultra-short ultra-intense laser pulses on to a solid target at intensities of $\geq 10^{18}$ W/cm² [G. Mourou, 2006], electrons at the target surface are accelerated up to MeV energies and, due to relativistic effects, mainly in the forward direction. It is expected that this motion produces currents of several MA and induces extremely intense magnetic fields.

Theoretical works, partly connected with the Inertial Confinement Fusion, already suggested that ultra-intense laser pulses could excite quasi-stationary magnetic fields of ≈ 100 kT (10^9 G, see [Sudan, 1993], for example). Particle in Cell simulations [Wilks et al., 1992; Pukhov and Meyer-ter-Vehn, 1996] supported the estimations performed with analytical methods. [Sentoku et al., 2002; Mason and Tabak, 1998] extended the investigation to overdense plasmas. In the same time experiments performed with optical techniques in the visible range (Faraday rotation, high harmonic suppression and ellipsometry, respectively), confirmed the presence of such huge fields [Borghesi et al., 1999; Tatarakis et al., 2002; Sandhu et al., 2002].

These colossal fields (up to 3.5×10^4 T) are very difficult to diagnose by conventional methods for several reasons. Their lifetime is very short, of the order of some picosecond, and they are confined in a small region (a few tens of μm). Since the plasma has a density close to solid state values it is opaque in the visible and UV spectral regions. Probing a state of the matter at such high densities requires very high frequency probe beams, e. g. X-rays.

The Zeeman effect was already used, in the visible range, in combination with a pair of polarizers, to measure the magnetic field produced by a Z-pinch [Sarfaty et al., 1995]. However, the Zeeman effect [Zeeman, 1897] has never been observed for hard X-rays. This is due to the fact that in order to be observed, the Zeeman energy splitting, $\Delta E \sim \mu_B B$ (where B and μ_B are the magnetic field and Bohr magneton, respectively) must be at least of order of the width of the X-ray emission line. Even for the relatively narrow, few-eV wide, X-ray lines of the low-Z, 3d transition elements, this requires extremely high fields, $B \sim 10^3$ T, which are not commonly available in laboratories.

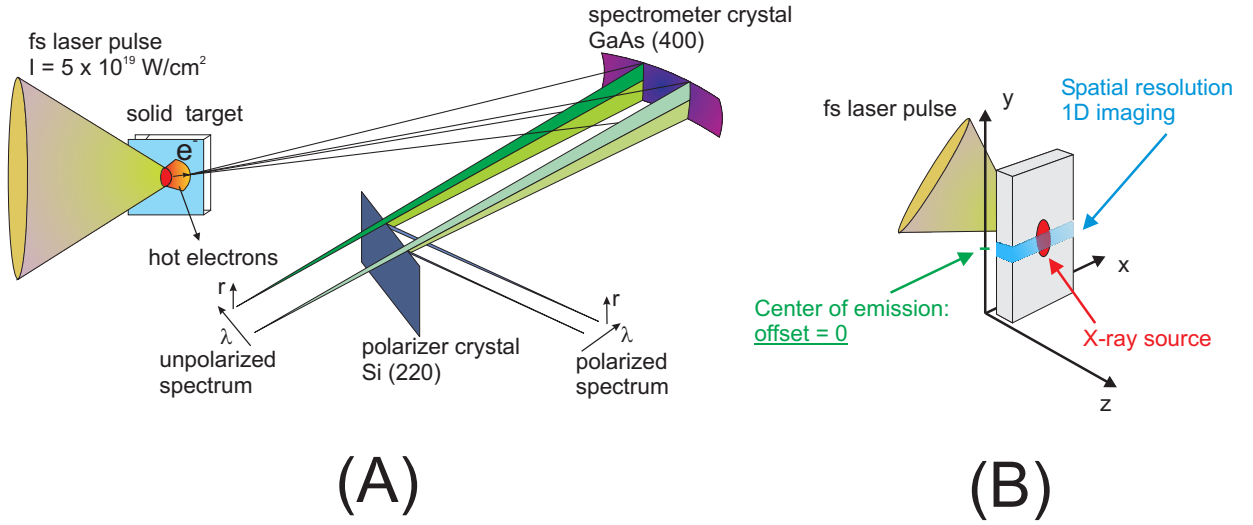


Figure 4.1: In (A) the experimental setup is shown. In (B) the target geometry is described in more detail: the laser pulse impinges on the target and the X-ray spectrometer is placed on the back side of the target. The 1D spatial resolution is along the y-axis: the features of the emission are integrated together along the x-axis and in the target depth, i. e. everything embraced by the bluish belt. The position where offset = 0 is also shown.

4.2 Experimental setup

The experimental setup is sketched in Fig. 4.1. The laser pulses, with energy on target varying from 150 to 500 mJ and pulse duration between 70 and 500 fs, were tightly focused down $5 \mu\text{m}^2$ yielding intensities up to $5 \times 10^{19} \text{ W/cm}^2$. 2, 5 and 25 μm thick titanium foils were used as targets. .

This study took advantage of a high spectral resolution experimentally determined to be $E/\Delta E \approx 15000$ ($\Delta E \approx 0.3 \text{ eV}$), and an 1D imaging with a spatial resolution of 20 μm for the first run and 4 μm for the second run. This was done by means of a toroidally bent GaAs(100) crystal, used at a Bragg angle of 76.60° in the fourth order for the Ti $K\alpha$ transition, and placed behind (see Fig. 4.1) the target at an angle of 27° with the target surface. The large Bragg angle provides a high angular dispersion and diffracted X-rays are almost nonpolarized: in Fig. 4.2 the reflection curves of the crystal for the two

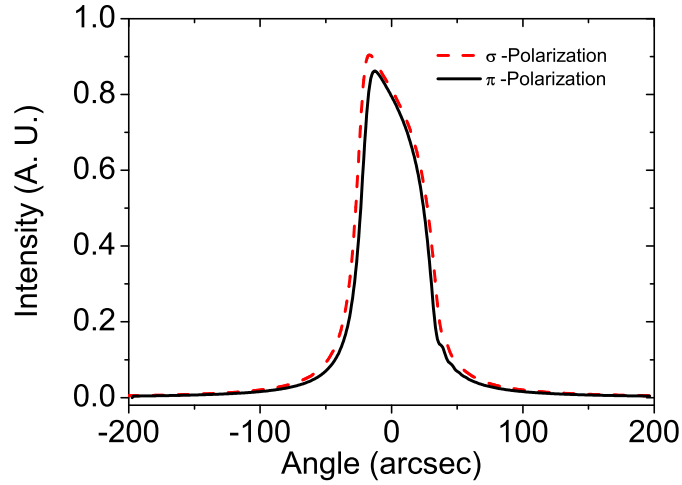


Figure 4.2: Calculated reflection curves for the bent GaAs (400) crystal for the two polarizations. The integrated reflectivity difference amount to about 10%.

polarizations are shown. The vertical bending radius allowed a high resolution 1D imaging to be achieved simultaneously with the high spectral resolution. Polarized spectra were acquired by allowing the radiation to reflect off a flat Si(220) crystal polarizer mounted in a non-dispersive geometry downstream from the bent-crystal analyzer. The spectra were recorded with calibrated Agfa Structurix X-ray films.

The results about the magnetic field measurements are concerning only the first run. In the second run, even if a substantial improvement of the spectrometer spatial resolution should have made the task easier, the massive presence of satellites had a negative impact on the possibility to clearly demonstrate a line broadening due to Zeeman effect. A better temporal contrast had (almost paradoxically) negative effects. On one side, according to simulations, the presence of a prepulse can increase the peak magnetic field (a factor of 5 was found in the simulations performed by [Evans, 2006]. See Fig. 4.3), on the other side, it is known [Rosmej et al., 2000] that the absence of a small prepulse gives rise to an increase of satellites.

However the polarization dependent measurements could give interesting hints about

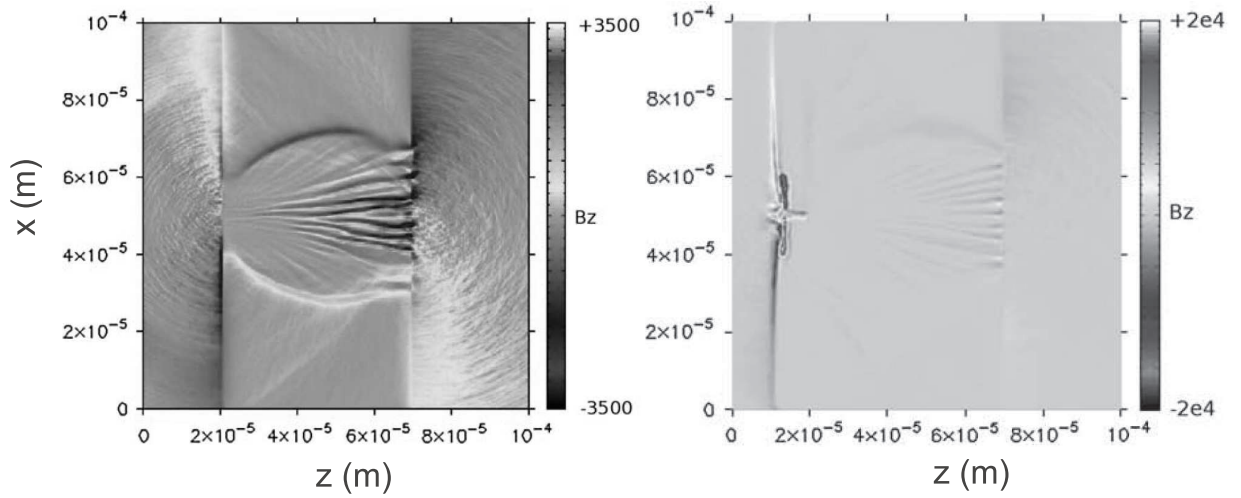


Figure 4.3: Simulations taken from [Evans, 2006] showing the influence of the prepulse on the magnetic field. On the left panel the electron jet meets the target without preplasma. On the right panel a linear preplasma is assumed. Note that the magnetic field is given in Tesla.

the electron velocity distribution inside the target. More details are given in Chapter 5.

4.3 Results

Fig. 4.4 is a typical spectral image, with Fig. 4.5 showing intensity x-axis scans of the $K\alpha_1$ peak, taken at the intensity maxima of the spectral images measured at the two indicated intensities. A broadening of 25%, well beyond the scatter of the measured X-ray intensities, is clearly observed at the higher intensities.

Scans of the $K\alpha_1$ images were taken at different y-axis offsets from the peak intensity of each image. Each scan was fitted by two Lorentzian plus a constant background, and the quantities derived from the fitted Lorentzians are plotted in Fig. 4.6. Fig. 4.6(A) shows where the X-ray emission takes place, i.e. where the laser intensity was the highest. Fig. 4.6(B) shows a clear increase in FWHM of about 0.4 eV from the peripheral regions towards the center for high intensities. At low intensities the linewidths exhibit almost no change. The dashed line shows the $K\alpha_1$ line width as measured with an X-ray tube; its

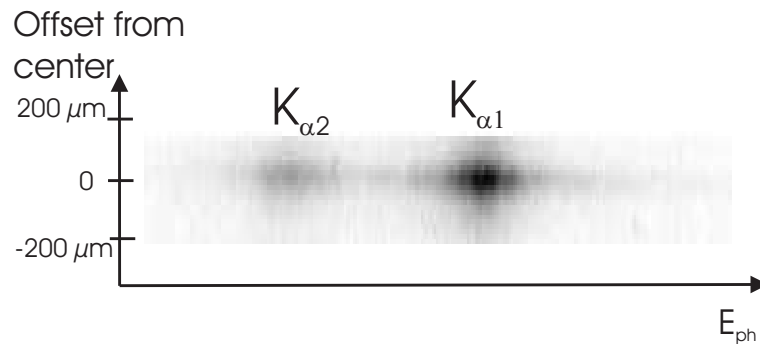


Figure 4.4: Typical spectral image. Note the energy resolution in the x-axis and the spatial resolution in the y-axis. A scan in the x-direction gives the spectrum at a given position. A scan in the y-direction gives the dimension of the X-ray source: in this case it was about $70 \mu\text{m}$ FWHM.

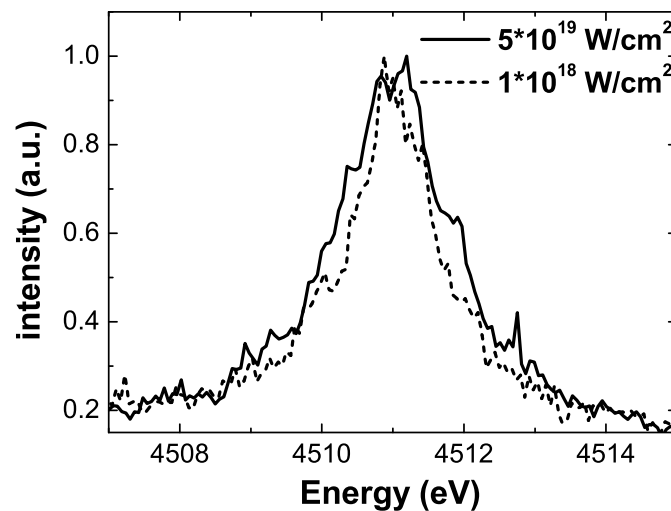


Figure 4.5: Scans of the $K\alpha_1$ line measured with the indicated intensities, unpolarized radiation, and $5 \mu\text{m}^2$ focal spot on a $25 \mu\text{m}$ Ti foil target. The dotted spectrum was preceded by a prepulse 150 ps earlier with a one thousandth of the main pulse energy. The solid line spectrum had no prepulse.

uncertainty is about $\pm 0.02 \text{ eV}$. The FWHM at the maximal intensity used is $\sim 0.55 \text{ eV}$ higher. Fig. 4.6(C) demonstrates that the $K\alpha_1$ peak position stays constant to better than

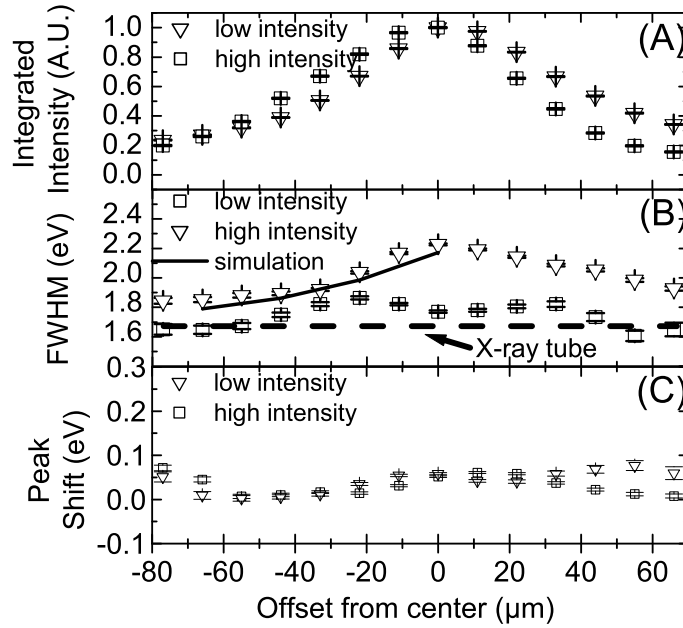


Figure 4.6: The analysis of the spectra. In (A) the area under the fitted $K\alpha_1$ line as a function of the position on the target (the emission maximum is the zero position). In (B) and (C) the same was done with the FWHM and the position of the maximum. In (B), with a dashed line, the FWHM as measured from an X-ray tube is displayed; the solid line shows the FWHM of the simulated spectra described later. Low and high intensity refers to the irradiation conditions described in Fig. 4.5.

± 0.07 eV for all offsets and intensities.

Calculations were performed at the Weizmann Institute, Israel, to estimate the influence of the Doppler and Stark effects due to micro fields in the plasma. Simple energy-balance considerations, 100 mJ laser energy distributed in the target, modeled as a squared prism $50 \times 50 \times 25 \mu\text{m}^3$, gives a mean energy of about 10...50 eV. The X-ray burst duration, ~ 500 fs, is of the same order as the electron-ion thermalization time, therefore $T_i = T_e$ can be assumed (T_i and T_e are the ion and electron temperature, respectively). From this ion temperature estimation, the influence of Doppler effect is ruled out easily: this is, in fact, connected with the ion velocity which is (due to the ion mass to electron mass ratio

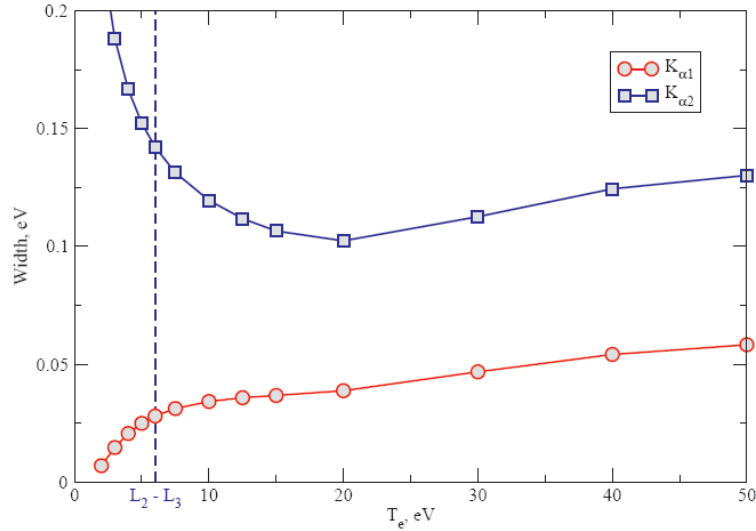


Figure 4.7: Stark broadening of the Ti-K α components as a function of the plasma electron temperature.

and the Ti atomic mass) about 10000 times smaller than the electron velocity. A value of some meV can be expected.

The Stark effect had to be calculated accurately. A computer simulation method described in [Stambulchik and Maron, 2006] was used and the local micro fields at ion locations for electrons and ions, as a function of time, were evaluated by means of a molecular dynamics (MD) model. The results are shown in Fig. 4.7: the line broadening due to the Stark effect is given as a function of the temperature for the two Ti-K α components. Assuming an electron temperature of about 20 eV one gets a non-measurable broadening for $K\alpha_1$ and a 0.1 eV broadening for $K\alpha_2$, which is smaller than the measured one.

Another possible source of broadening are satellites. M-shell holes produce satellites in K α lines too close to the diagram lines to be independently resolved. In experiments where Ti targets were bombarded with fast heavy ions, M-shell holes were considered responsible for blue shift and variations in the linewidth of the L-shell satellites of the K α lines [Hill et al., 1976]. In some published work [Aglitskii et al., 1982; Morita et al., 1983] a red shift in the K-shell emission of ionized spark plasmas was observed. This effect was ascribed to the presence of one vacancy in the M-shell of the emitting atoms. To our knowledge, no

red shift due to satellites has been measured for laser-plasma sources .

To demonstrate that there is no red shift of any kind in our measurements we compared scans of spectral images acquired with different intensities and target thicknesses. In any case no red shift could be discerned. Hence, we can say that any satellites, which may be present (as e.g. for 2 and 5 μm thick targets, see Chapter 5, Fig. 5.4), can be seen only on the blue wings of the $K\alpha$ lines, depending on the intensity and the target thickness. These two parameters can be considered as two different ways to vary the ionization stage $\langle Z \rangle$. In another study carried out under similar experimental conditions, Hansen et al. made a direct connection between $\langle Z \rangle$ of the plasma and the target thickness [Hansen et al., 2005].

In the present 25 μm target measurements, no significant shift is measured either for the high intensity or for the low intensity spectra to within ± 0.07 eV, as seen in Fig.4.6(C). Also, the line broadening is symmetrical with respect to the central photon energy, implying no red- or blue-shifted underlying satellites. Thus, in the absence of the two main signatures of satellites, peak shift and line asymmetry, it is safe to conclude that the observed broadening does not originate from satellites.

4.4 Simulation

The measurements are the results of many unavoidable averages: the spectra are integrated in time, in one spatial dimension (along the line of sight) and in the depth. To be able to extract information about the spatial distribution of the magnetic field, we compared the measurements with a 2D simulation. In Fig. 4.8 the main ideas behind the simulation are pictorially shown; in the following the main steps of the simulation are illustrated:

- The magnetic field was modeled as a function of the distance from the laser focal spot, with a $1/r^\gamma$ dependence when r is larger than the laser focal spot, and a linear dependence otherwise ($\gamma = 1$ is the case of a wire with streaming current). $\gamma = 0.4$ gave a satisfactory agreement with the measured data (see simulation in solid line, in Fig. 4.6(B)). A cylindrical symmetry and a doughnut-like distribution around the

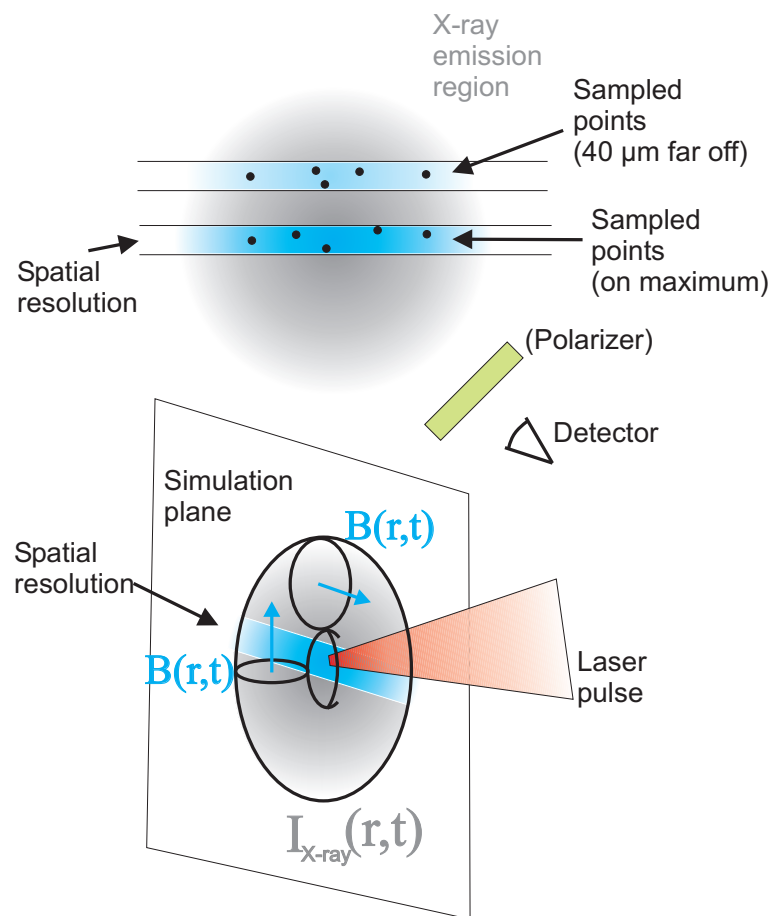


Figure 4.8: Illustration of some of the ideas behind the simulation. The X-ray emission in grey is overlapped with the magnetic field. The blue stripes give the spatial resolution: the emission features in them are integrated together.

focal spot were assumed for the magnetic field.

- The time dependence of the field is shown in the inset of Fig. 4.10(A) and was adapted, together with the relative delay with respect to the laser pulse from the works of [Sandhu et al., 2002, 2006].
- The X-ray emission was assumed to have a Gaussian shape, in space and time (500 fs FWHM [Reich et al., 2000]).
- The simulation begins 100 fs before the start of the laser pulse and continues for

1500 fs; at each step (50 fs) the X-ray emission and the magnetic field are sampled with a Monte Carlo routine in different positions; the intensity of the emitted radiation, the magnetic field and the position of the sampled points are saved.

- The X-ray emission is decomposed in the different polarizations according to the magnetic field vector orientation.
- The polarization properties of the spectrometer and, if inserted, of the polarizer are taken into account and the final intensity recorded on the film is calculated.
- The X-ray emission and the spectrum (due to the magnetic field influence¹) of points belonging to a single stripe (the bluish horizontal stripe, in Fig. 4.8) are averaged to take into account the integration done by the spectrometer because of its 1D imaging properties.
- The results coming for the single time steps are summed up to obtain the total, 1D space resolved lineshape. Times beyond 1.5 ps are not important because the X-ray emission has already ceased.
- The simulation takes into account the apparatus function and the real spatial resolution of the spectrometer so that the simulation and experimental results are directly comparable.

Some comments about the works cited in the second point [Sandhu et al., 2002, 2006]: this is the only time resolved measurement available concerning magnetic fields produced by fs laser pulses. They shined Al bulk and Al(500 nm) deposited on glass to study the behaviour of hot electrons. In this thesis, only the case of bulk Al was taken into account because the target used in this thesis was also made of metal and the target thickness is

¹Zeeman splitting and intensity of the resulting components were calculated by means of INTDPH2, a computer program written by E. Stamboulchik from the Weizmann Institute, Israel. It solves the Hamiltonian of the system under the influence of external electric and/or magnetic fields.

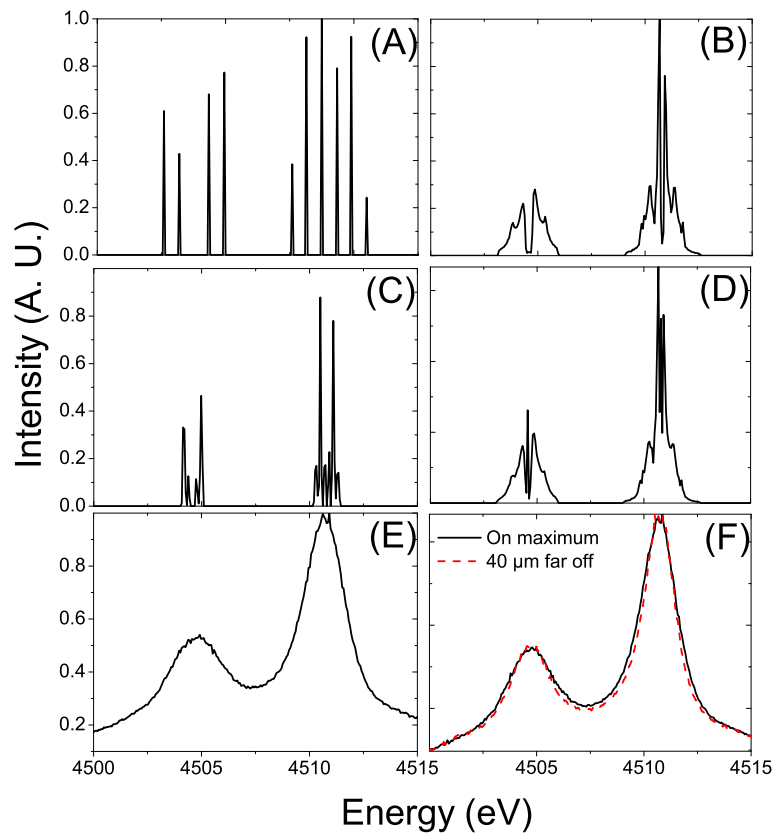


Figure 4.9: Simulation of influence of a magnetic field on the Ti-K α spectrum. More in the text.

reasonably comparable². However, in our case a magnetic field duration shorter than some ps can be expected. Under this point of view the model would be a worst case: a shorter magnetic field duration would mean higher peak magnetic field needed to reproduce the measured line broadening.

²Target thickness: 25 μm . The time needed for energetic electrons to go through the Ti foil is ≈ 100 fs, to be compared with the some hundred fs expected x-ray pulse duration. We note that the magnetic field duration in the case of a layer of Al + glass is much shorter: the hot electrons do not propagate easily in glass. The electric fields they build, can stop them very quickly. This implies a shorter duration of magnetic field. One can think of the target as Ti + vacuum.

In Fig. 4.9 some features of the simulation are shown to give a clearer view of the simulation's behaviour. (A) shows the effect of a constant magnetic field of 18 kT (or 180 MG) on Ti-K $\alpha_{1,2}$, i. e. the effect of a constant (in space and time) magnetic field on delta-like spectral lines. In (B) only the spatial variation of the magnetic field, is taken into account; the X-ray spatial emission is assumed to be Gaussian, 100 μm FWHM. The integration in one dimension due to the 1D imaging (the blue stripe in Fig. 4.8) causes the merging of the spikes into a continuous line: points in different positions experience different magnetic fields and emit with different intensities and wavelengths. (C): like (B) but the region considered is 40 μm far from maximum intensity. The magnetic field is smaller in average, the lines are consequently narrower. In (D) the time dependence of the magnetic field is taken into account (see inset in (A) Fig. 4.10); the position of the maximum intensity is considered again: the lines are smoother because the magnetic field assumes many more values in the different time steps. Let us assume now to repeat the calculations, not only for two energies of the spectrum, but also for every point of a spectrum acquired at an X-ray tube, weighting the calculated intensity with the measured intensity. Then we obtain a complete spectrum in which the evolution of magnetic field and X-ray emission, together with the energy and the spatial resolution of the spectrometer are taken into account. If the magnetic field is zero, we get the X-ray tube spectrum. If there is an influence of the magnetic field, we can calculate it: moreover the characteristics of the spectrometer are reproduced and we can directly compare the laser-plasma spectrum (with a certain measured spatial resolution) with the calculated one to get detailed information about the spatial evolution of the magnetic field. This is what we see in Fig. 4.9 (E) and (F). In (E) a constant (in time) magnetic field of 18 kT was assumed. In (F) the time evolution is included and the lines are consequently narrower. The effects of considering the region of maximum intensity or 40 μm far off are also shown.

The results for the K α_1 line are shown in Fig. 4.10 (A). The peak magnetic field is found to be $\sim 18 \text{ kT}$ ³. The experimentally-observed line broadening (solid line) of 30% is

³As an error a value of $\pm 5 \text{ kT}$ can be given. This does not come from the comparison simulation – measurements but from the model and assumptions used. The magnetic field time dependence, for

well accounted for by the model (dashed line). A simulation with the very same magnetic field time dependence is shown for $K\alpha_2$ in (B). For both plots the spectra shown are all nonpolarized. The ratio $K\alpha_1 / K\alpha_2$ for the X-ray tube spectrum and laser-plasma spectrum are slightly different. For this reason the results of the simulations for the two lines are shown separately with two different scales.

Simulations showed that the linewidth difference between polarized and nonpolarized spectra amounts to about 10–14%, as shown in Fig 4.11. Due to the shot number needed to obtain a sufficient density on the film, the background, caused by charged particles and bremsstrahlung, is very high in the case of polarized spectra. The resulting low signal to noise ratio is not enough to draw conclusions about the magnetic field from the comparison polarized–nonpolarized spectra.

We tried to use the technique described in Sec. 2.4 and successfully applied in [Deutsch et al., 1995] in order to find out how much the satellites could have influenced the measured line broadening. To get a quantitative estimation of the satellite influence we proceeded in the following steps:

- The best values for the free parameters (position, intensity and common line width of the multiplets calculated with a relativistic multiconfigurational Dirak–Fock code) are calculated by fitting them with a high resolution spectrum acquired at an X-ray tube.
- The procedure is repeated for laser-plasma spectra, allowing changes for the parameters only in the line width.
- If this had been enough to reproduce the broadened lines, one could have proved that only line broadening coming from a magnetic field was present. If, otherwise, other groups of satellites were needed, the possibility of a presence of satellites in the broadened profile would have been remarkably high.

example, was measured with lower intensities. The X-ray pulse duration at these laser intensities has not been measured and can only be roughly estimated.

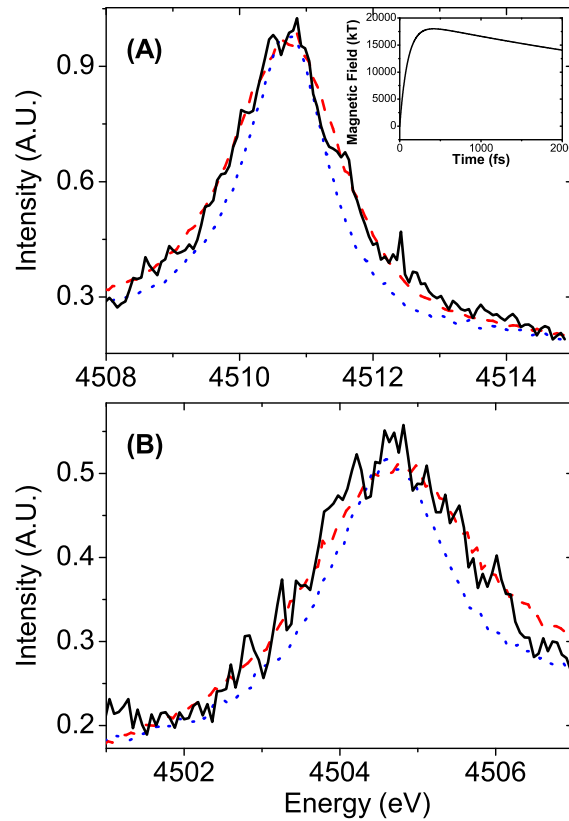


Figure 4.10: (A) Measured (solid line) and calculated (dashed line) $K\alpha_1$ line for a $25\ \mu\text{m}$ thick target and a laser intensity of $5 \cdot 10^{19}\ \text{W}/\text{cm}^2$. The magnetic field time dependence used in the calculation is shown in the inset. The X-ray-tube-produced $K\alpha_1$ line is also shown (dotted line). (B) The same for the $K\alpha_2$ line by using the same magnetic field. This plot has a different scale. More in the text.

Unfortunately the complexity of the titanium atomic structure together with the relatively low quality of the laser-plasma spectra did not allow any statement about the magnetic field and satellite presence. However, the presence of satellites could be reasonably excluded, as shown in Sec. 4.3, by taking into account symmetries of the line broadening and possible line shifts.

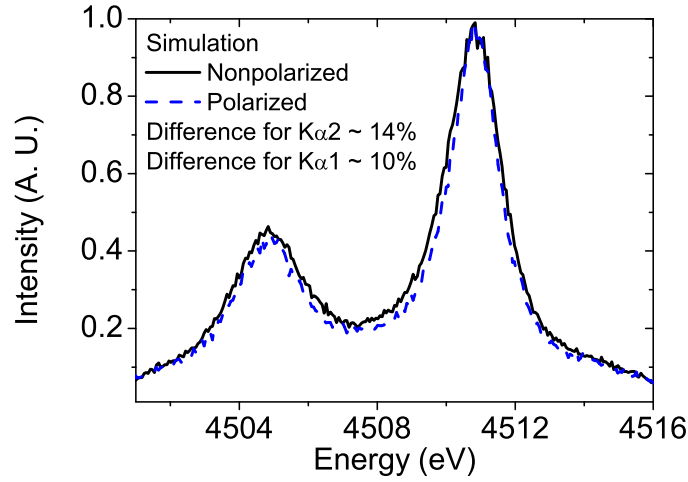


Figure 4.11: Expected changes of the line profile between polarized and nonpolarized spectra for the same conditions of Fig. 4.10. To be compared with the first spectrum of Fig. 5.5 in Chapter 5. There the noise level for the polarized spectrum is clearly too high to discern the expected linewidth change.

By exploiting the number of photons recorded on the film (about 9000 per pulse) we tried to estimate the magnetic field that can be expected. By taking into account the crystal reflectivity (eq. 3.14) and the losses due to 3 passes through Al filters, it is reasonable to assume 10^{10} photons created in the source. [Volkmer, 2004] calculated, by making use of a Monte Carlo + PIC code, for a $25 \mu\text{m}$ thick Ti foil and a detector at 45 degrees that one $K\alpha$ photon is created every 0.008 electron moving with an energy of about 1 MeV (see Chapter 5). Under the simplifying assumptions that all the electrons involved in the creation of $K\alpha$ radiation are going in the forward direction, belonging to the hot part of the distribution and are not involved in the refluxing at the back side of the target one finds that about 10^{12} electrons penetrate the target in a region with about $70 \mu\text{m}$ diameter (the measured FWHM of the X-ray source). We are then dealing with a 1.6 MA current and with an induced magnetic field of about 10 kT.

Note, that an average magnetic field of about 10 kT would be necessary to explain the measured line broadening (Fig. 4.10 takes into account a time dependence of the magnetic field). The result of these two completely different ways to calculate the magnetic field agree with each other.

4.5 Conclusions

For the first time it was possible to detect a laser-induced magnetic field inside the solid target: this was done by means of X-ray spectroscopy. To my knowledge this is not possible with any other method known at the moment.

We stress the fact that we observe line broadening when we compare two spectra acquired with different laser intensities (Fig. 4.5) but also when we consider, in the very same spectral image, two scans with different offsets (Fig. 4.6).

In conclusion we have shown that the Zeeman effect can be exploited to gain an insight into the complex subject of the laser-matter interaction at relativistic regimes. The ability to use X-rays to track the magnetic field, i.e. the electrons in their path through the matter, from *inside*, offers new intriguing perspectives to understand electron dynamics at such strong laser intensities.

Chapter 5

Spectropolarimetry of solid-density plasmas generated by fs laser pulses

5.1 Introduction

Spectropolarimetry allows detailed measurements and analysis of radiation, as well as its interaction with matter. Polarized spectra are sensitive to anisotropies (in the radiating and transmitting media) such as directionality in the electron velocity distribution [Fujimoto and Kazantsev, 1997]. Such polarization-dependent measurements have been employed in studies of high temperature laser-produced plasma lines [Kieffer et al., 1992, 1993] in high resolution X-ray spectroscopy of trapped highly charged ions [Shlyaptseva et al., 1997; Beiersdorfer et al., 1999] and in an X-pinch [Shlyaptseva et al., 2003].

$K\alpha$ emission in a target, produced by electrons accelerated in a dense, thin plasma layer at the target surface by laser pulses and then propagating in the cold target, can be used to monitor the propagation of electrons in matter [Pisani et al., 2000]. Spectropolarimetry of the $K\alpha$ emission, allows the study of the behavior of electrons *inside* the target. Compared with other techniques, this is a clear advantage. For example, an electron spectrometer measures the energy of electrons *after* they exit the target. In between they traverse huge electric fields, of the order of TV/m [Romagnani et al., 2005], created by the space charge separation. Thus, the electron spectrum may be altered considerably. Alternatively, a layered target can be used, in conjunction with an imaging system, to monitor the $K\alpha$ emission from the different layers [Feurer et al., 1997; Wharton et al., 1998]. This method also has drawbacks: the cross-section for the K-shell ionization by electron impact is not

a monotonic function of the energy. For example, for titanium it has a maximum at 20 – 30 keV, then a fall-off, and again a rise at MeV energies. In looking at the emitted intensity, it is not possible to determine whether it was generated by the high-energy electrons, going in the forward direction, or by electrons with much lower energy (thermal electrons or return current electrons).

5.2 Experimental setup

The experimental setup is given in Fig. 5.1 [Zamponi et al., 2007]. Titanium foils 25, 5, and 2 μm thick were used as target. Behind the target an electron spectrometer was assembled as an additional diagnostic. Alternatively an image plate stack could be employed to monitor the total amount of electrons, their energy and directionality.

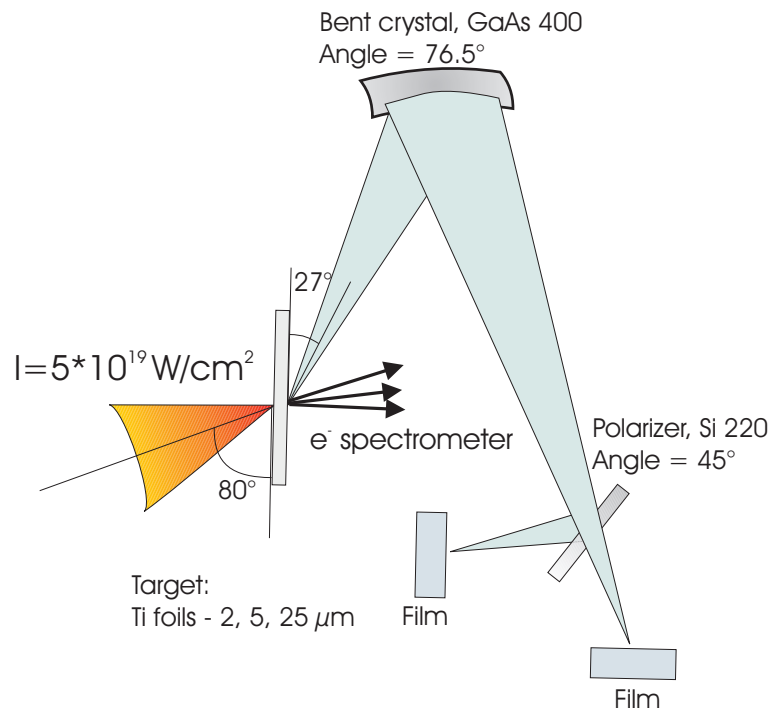


Figure 5.1: Scheme of the experimental setup.

The X-ray spectrometer employed a GaAs (400) crystal toroidally bent to radii of 450 mm in the horizontal direction and 305.9 mm in the vertical direction. It had an

energy resolution $E/\Delta E \approx 15000$ and a spatial resolution in the vertical direction of $4 \mu\text{m}$. A flat Si(220) crystal polarizer could be positioned in a non-dispersive orientation downstream from the bent-crystal analyzer, to allow the acquisition of polarized spectra [Uschmann et al., 1993]. The spectrum was recorded by means of Agfa Structurix X-ray film, which was calibrated in intensity to allow a quantitative extraction of the data.

5.3 Space and polarization dependent spectra

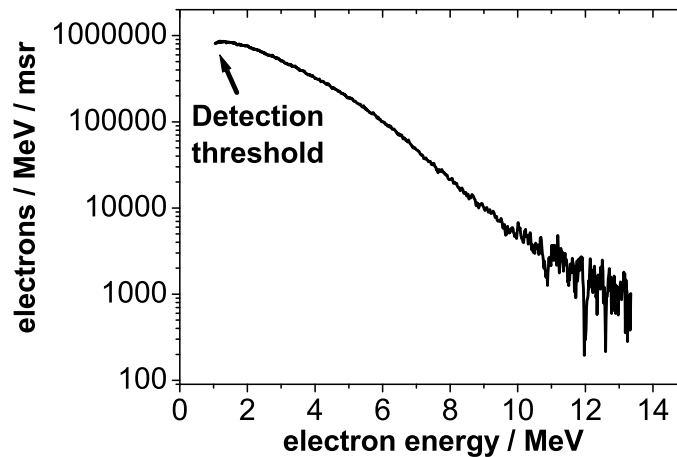


Figure 5.2: A typical electron spectrum.

In Fig. 5.2 we show an electron spectrum generated by focusing a $5 \times 10^{19} \text{ W/cm}^2$ intense laser pulse on a $2 \mu\text{m}$ -thick Ti foil. The electron temperature derived from the data was about 1.4 MeV and the analysis of the image plate stacks gave a similar value. The divergence derived for the stack data was ≈ 0.5 rad, with slightly better collimation for the higher energy electrons.

Fig. 5.3 (B) shows typical recorded spectral images for the same laser and target parameters described above. The horizontal and the vertical directions correspond to the energy and the spatial extent of the emission, respectively. Due to the 1D imaging the

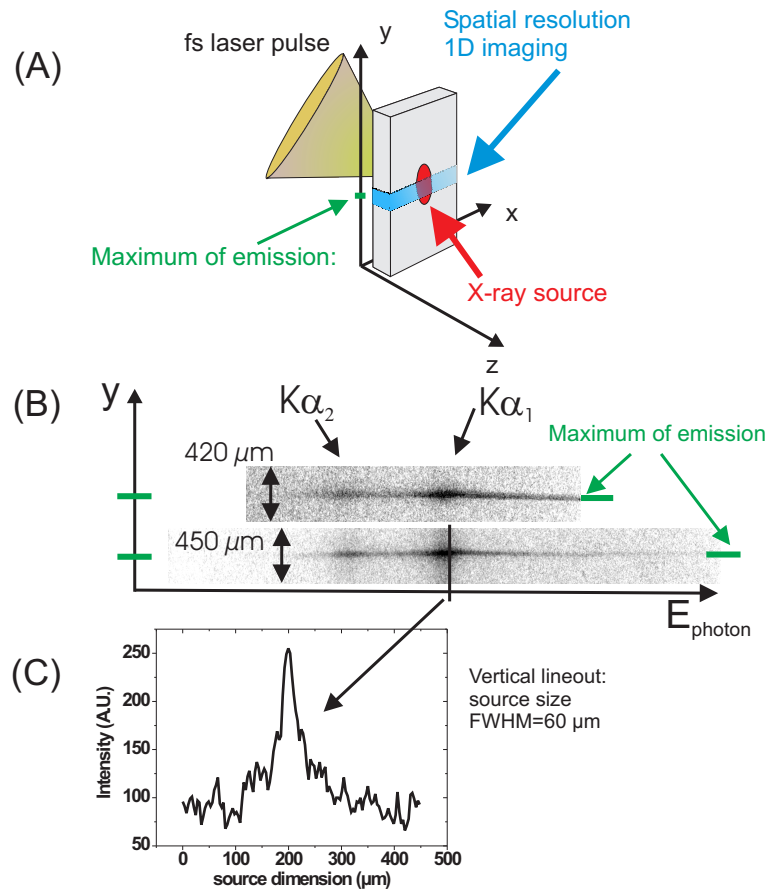


Figure 5.3: In (A) the target and the spectrometer geometry is described: the laser pulse impinges on the target and the X-ray spectrometer, placed behind, makes an 1D image of the source. The integration is accomplished along the line of sight, i. e. along the x-axis and in the depth (in figure shown by the volume embraced by the blue stripe). In (B) typical spectral images are shown. The upper one was acquired by using 250 laser pulses, with an intensity of $5 \times 10^{19} \text{ W/cm}^2$ on a $2 \mu\text{m}$ -thick Ti foil target; the polarizer was used. For the lower spectral image the same parameters were used but the polarizer was absent and only 15 laser pulses were needed. A vertical scan of the film at the $K\alpha_1$ peak position is shown in (C).

spectra are integrated over the extension of the emission along the line of sight. The two intensity peaks are the $K\alpha_1$ and $K\alpha_2$ lines, as indicated by the arrows. A lineout in the vertical direction provides the dimension of the $K\alpha$ source; in this case, a FWHM of about

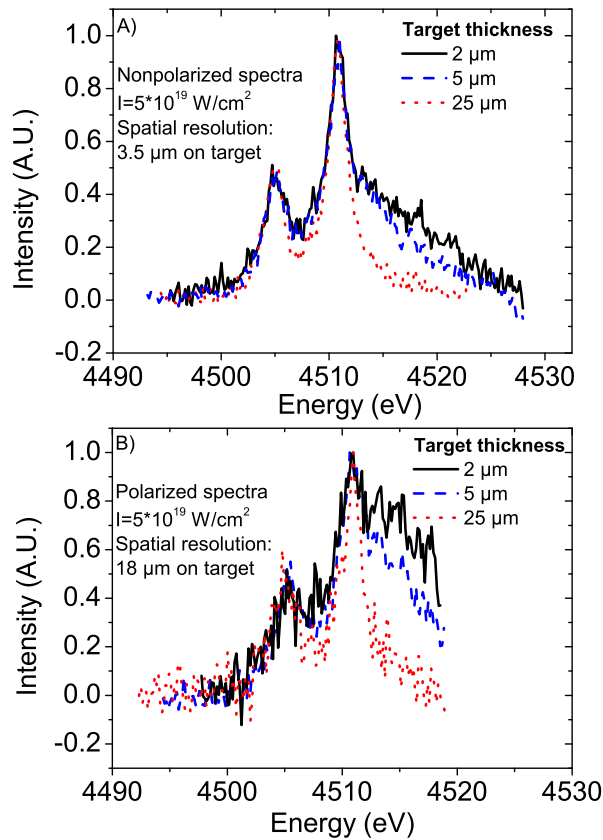


Figure 5.4: Comparison of polarized and nonpolarized spectra for different target thickness in the region of maximum intensity. The lower spatial resolution in B) was required to increase the signal to noise ratio.

60 μm on target is measured.

In Fig. 5.4 we show a comparison between polarized and nonpolarized spectra for different target thicknesses. The nonpolarized spectra show an increasingly pronounced shoulder on the “blue” side of both $K\alpha_1$ and $K\alpha_2$ as the target thickness is decreased, as has been already noted in Ref. [Hansen et al., 2005]. For the polarized spectra the change is considerably more pronounced than for the nonpolarized ones. For the 2- μm and 5- μm thicknesses the blue side is so strongly enhanced that $K\alpha_2$ becomes a small bump on the red side of $K\alpha_1$.

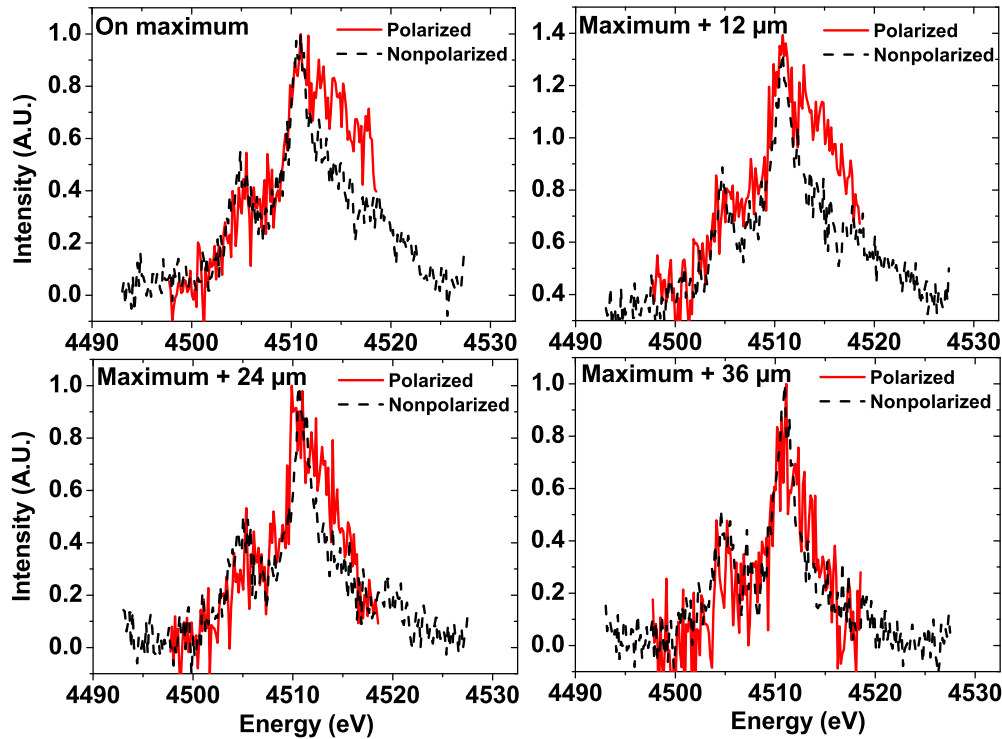


Figure 5.5: The dependence of the measured $K\alpha$ spectra on the displacement from the position of the maximum intensity.

The variation of the amount of satellites for the different target thicknesses can be explained as follows: the energy deposited by the laser pulse has to be distributed among a certain amount of atoms in the case of a thick target; an electron temperature will result and correspondingly an ionization degree. If the target is thin, the energy available for every atom is higher, the temperature and the ionization degree will be higher; there will be consequently an higher amount of satellites.

Figure 5.5 shows a dependence of both, polarized and nonpolarized spectra on the displacement from the peak-emission position of 12, 24, and 36 μm , for a 2 μm -thick target. The spatial resolution was 4 μm , and the laser intensity was 5×10^{19} W/cm². It

is seen that at the peak intensity there is a clear difference between the polarized and nonpolarized spectra. At $24\ \mu\text{m}$ from the maximum, the difference becomes smaller: the blue wing of the polarized spectrum is significantly reduced towards the unpolarized wing. At $36\ \mu\text{m}$ from the maximum the two spectra nearly coincide within the experimental error-bars.

In Fig. 5.6 the effects of a lower intensity irradiation are clearly to be seen. Here again a $2\ \mu\text{m}$ -thick target was employed. This figure should be compared with the first one of the series in Fig. 5.5. The blue side of the polarized spectrum is much less pronounced, indicating a much lower degree of polarization.

These results may provide insight into the electron motion within the target. The beam-like feature of the electron velocity distribution, clearly visible in the stack analysis, spreads out significantly only about $20\ \mu\text{m}$ away from the laser focal spot; $40\ \mu\text{m}$ away from focus the electron distribution is nearly isotropic. We note that the target concerning the spectra in Fig. 5.5 was only $2\ \mu\text{m}$ thick and the laser focal spot $5\ \mu\text{m}^2$. The region over which the electron velocity distribution stays anisotropic is much larger than these dimensions. It is possible that this is caused by the inhibition of electron propagation due to electric fields [Bell et al., 1997]. The bending of electron trajectories due to magnetic fields, as suggested by [Reich et al., 2003] may also have played a role.

At this point we want to stress that the steps to go from the comparison of a pair polarized–nonpolarized spectra to a reliable expression for the electron velocity distribution are very complex. In [Hakel et al., 2004] there is an example of the procedures needed to extract information from spectropolarimetry measurements. The laser target interaction is simulated by means of a hydrodynamical Lagrangian 1D code and a 1-1/2D particle-in-cell code. The former is used to monitor the overall target behavior as it is heated by the laser, including laser energy coupling and deposition, electron and ion heat conduction, and hydrodynamic motion; the latter to model the electron kinetics of the production of a beam of energetic electrons due to resonance absorption in the laser-plasma interaction. The results are used to feed other codes to calculate the overall ionization balance, and magnetic sub-level populations. Finally the information are put together to obtain, time

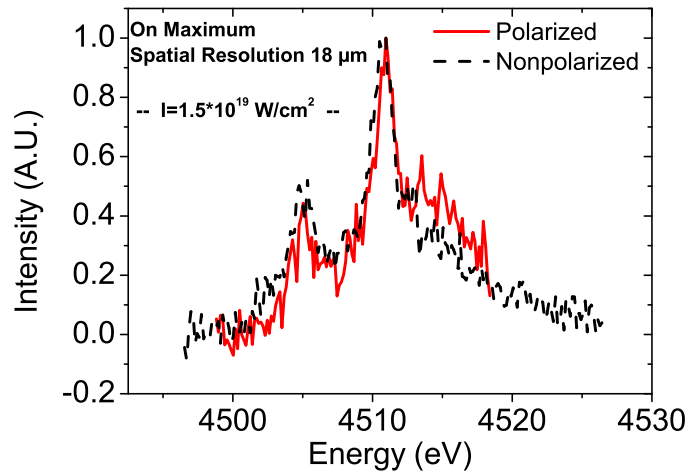


Figure 5.6: Comparison of polarized and nonpolarized spectra for lower intensity.

resolved, the values that can be measured with spectroscopic method, I^σ and I^π .

It is also worth to mention that the works that can be found in the literature are always concerning lines coming from a hot plasma (H-like, He-line). These calculations are relatively simpler than those involved to evaluate the scattering matrix for an almost complete atom, as it is the case for this thesis: the Ti atoms are three to five-fold ionized.

5.4 Conclusions

We measured spectra of the $K\alpha$ emission from Ti foil targets irradiated by femtosecond laser pulses. A strong polarization dependence of the X-ray spectra was observed.

The polarized spectrum evolution as a function of the distance from the peak of the emitted intensity was determined with a $4\text{-}\mu\text{m}$ spatial resolution.

The results present a clear indication of strongly anisotropic processes *inside* the laser-irradiated targets. Spectropolarimetry is thus a sensitive tool, e.g., in the studies of electron transport properties under such extreme conditions of relativistic plasmas at solid density.

Chapter 6

Energy resolved 2D imaging of an X-ray source at relativistic intensities

6.1 Introduction

The interaction of femtosecond laser pulses with solid target materials generates 'hot' electrons which, penetrating into the cold target, produce K-shell ionization and consequently X-ray emission in the keV energy-range. Even if a lot of efforts have been invested in the field, there are still many unclear aspects, as already noted in the introduction (see Sec. 2.1.3), e. g. the role of magnetic and electric fields and laser intensity on the source dimension. The behaviour of the electrons under these extreme conditions is also not well understood. This experiment was meant to help to comprehend and, if possible, to explain the sometimes contradictory results found in the literature.

6.2 Experimental Setup

The electrons, accelerated up to relativistic energy in the thin layer plasma at the interface laser-target, penetrate into the target. Along their path they ionize the K-shell of the target atoms, recombination takes place with consequent emission of $K\alpha$ radiation. We exploited this connection $K\alpha$ photon – electron to be able to track the path of the electrons through the target: a layered target was used in the experiment, so that different $K\alpha$ photons could be ascribed to different positions in the target. For this purpose we used two pin-holes coupled with two X-ray CCDs put at the back and at the front side of the target.

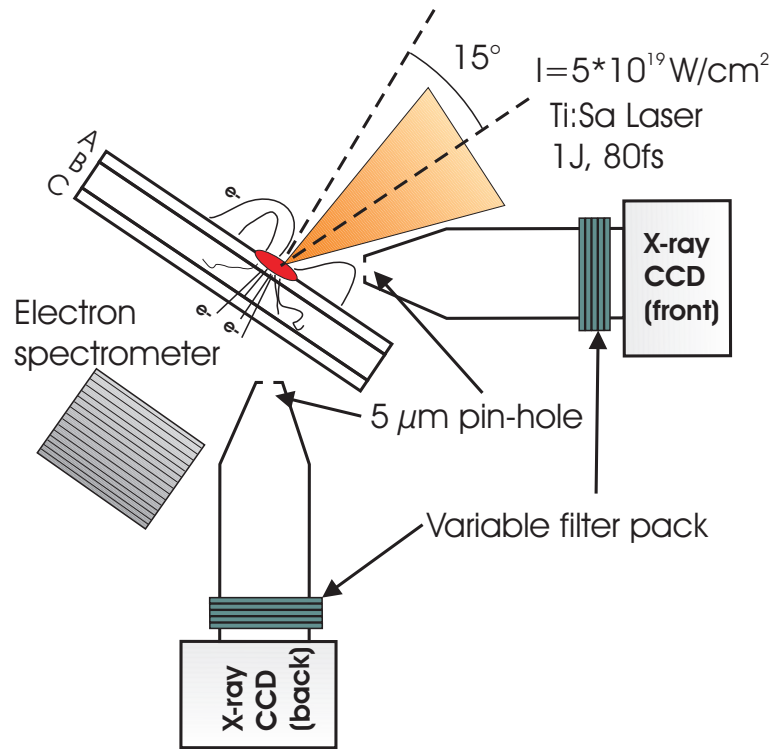


Figure 6.1: *Experimental setup.*

In the experiment, sketched in Fig. 6.1, the JeTi Ti:Sapphire laser pulses with 600 mJ on target in 70 fs, were tightly focused by means of an off-axis parabolic mirror to about $5 \mu\text{m}^2$ to reach intensities up to $5 \times 10^{19} \text{ W/cm}^2$. The target was either a Ti foil with 5 or 25 μm thickness or a layered target (Cr+Ni+Fe). Two $5 \mu\text{m}$ diameter pin-holes coupled with two well characterized deep-depletion back-illuminated charge-coupled device cameras [Zamponi et al., 2005] were looking to the front and the back side of the target at an angle of 45° . The spatial resolution of the imaging system was about $5 \mu\text{m}$ on target with a magnification $M=11$. The path between source and camera was shielded by a hollow lead cylinder containing NdFeB small magnets, to deflect electrons coming from the source. A careful filtering of the X-ray signal, obtained by using a variable number of $50 \mu\text{m}$ thick mylar sheets, allowed the CCD cameras to work in single photon regime, i. e. the number of detected photon was much smaller than the number of pixels. Since the amount of created charge on the camera chip is proportional to the photon energy, we could use the CCD

as a non-dispersive spectrometer. Imaging was made possible, virtually, in every energy window between 3–4 keV up to 12 keV, limited only by the energy resolution (about 180 eV for the CCD cooled down to -70° C) and the amount of photons available. In this way, a comparison for X-ray images recorded with the same laser pulses in different spectral windows could be made for the first time.

Software written in house remedied for X-ray photons splitted into more pixels (see for instance [Zamponi et al., 2005; Labate et al., 2002]). Care was taken to avoid the presence of visible light on the CCDs. A stack electron spectrometer [Galimberti et al., 2005] could alternatively be put behind the target to monitor electron temperature and divergence.

6.3 Titanium foils: Results

A first run employed Ti foils as a target. In Fig. 6.2 we show sample images of the X-ray source acquired in consecutive shots. The dimension of the images is $120 \mu\text{m} \times 120 \mu\text{m}$. The 45 degrees observation angle was not compensated: even if for $5 \mu\text{m}$ target foils this would be an immediate task, for $25 \mu\text{m}$ thick target foils this would be not straightforward. In this case the dimension of the source is comparable with the target thickness and it is impossible to say where photons are coming from.

In this case no filters were used, i. e. the images are not energy resolved. We note that the spot size increases by increasing the laser intensity (from $11.4 \mu\text{m}$ to $13.3 \mu\text{m}$). The B–C and D–E series are concerning the very same shots acquired from the front and the back camera, respectively. The images A6 to E6 were obtained by summing up about 100 single images. To avoid possible effects due to target surface irregularities, the center of mass of a square 50×50 pixel around the expected position of the source was calculated. Possible shifts were compensated and then the images were summed up.

Naively, from the comparison between D and E series, one would have expected to see the same features when looking from the front and the back side on to a $5 \mu\text{m}$ thick Ti foil, since the attenuation length for Ti $K\alpha$ photons in Ti is $20.3 \mu\text{m}$. On the contrary there are surprising differences. The intensity for the back camera is about a factor 3 lower (the

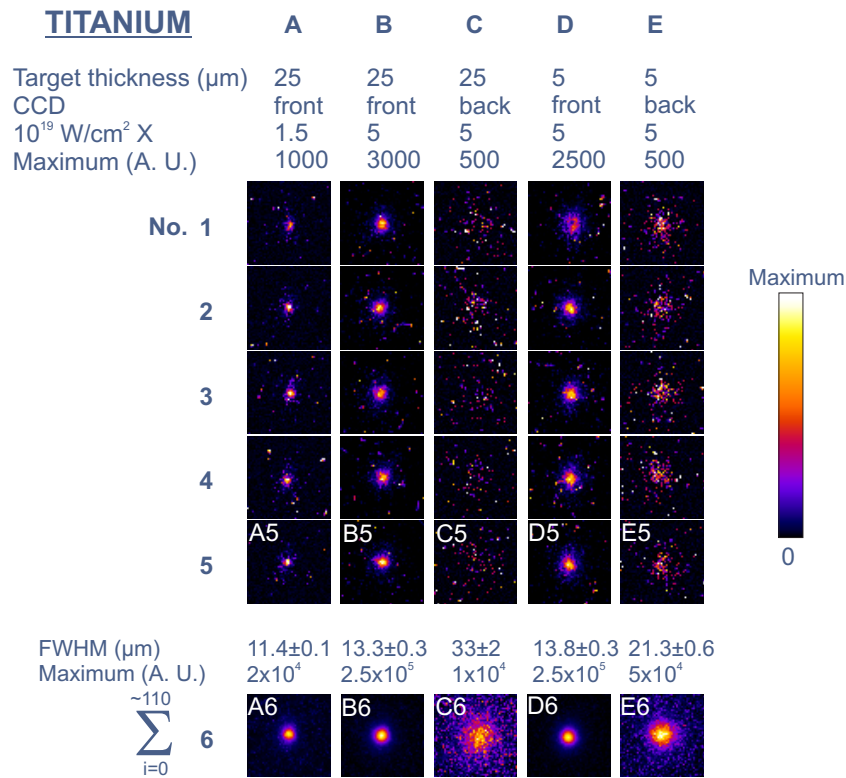


Figure 6.2: Series of consecutive single shots (from 1 to 5 for A to E). For each column a different scale was used. The dimension of the images is $120 \mu\text{m} \times 120 \mu\text{m}$. The target thickness in μm , the camera position, the intensity on target in W/cm^2 and the value of the maximum (see color bar on the right hand side) are reported on the upper side. Note that images B1–C1 to B5–C5 and D1–E1 to D5–E5 are the very same shots as seen from the two cameras. Images A6, B6, C6, D6, E6: sum of about 110 images with the above described characteristics. The FWHMs of the vertical lineouts, are reported on the images of the 6-series. Note that vertical lineouts can avoid possible influences of the target thickness (A6 and B6 comes from a $25 \mu\text{m}$ thick target, to be compared with the $5 \mu\text{m}$ spatial resolution and the attenuation length $\lambda_{Ti} = 20.3 \mu\text{m}$ for $\text{Ti-K}\alpha$; λ_{Ti} is the path needed to reduce the intensity by a factor $1/e$) and the geometry (the observation angle of 45°).

images have different scales) and the source is broader.

The explanation for this can be found by looking at the spectra recorded by the CCDs. In Fig. 6.3 spectra of the radiation recorded in the neighbour regions of the maximum

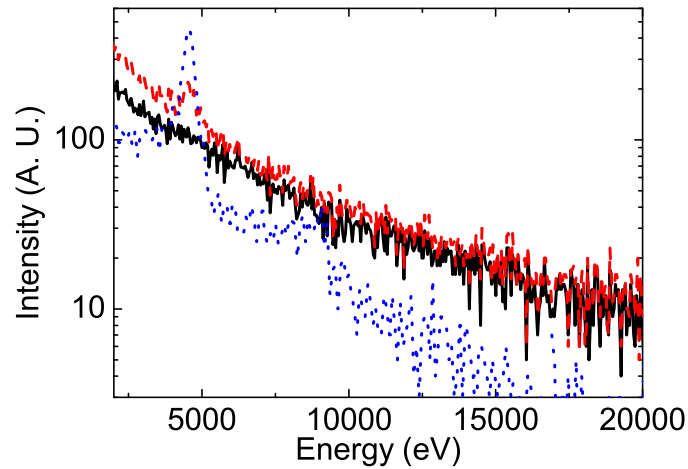


Figure 6.3: Comparison of spectra measured by taking into account pixels in a squared region around the region of maximum emission. About 110 single-shot images were analyzed. Solid line: 20×20 pixel region, front CCD, intensity $\approx 5 \times 10^{19}$ W/cm², 5 μ m thick Ti foil. Dashed line: same conditions but a 40×40 pixel region was used. A small peak at 4.5 keV is visible: Ti-K α photons come mainly from more peripheral regions. Dotted line: same as for solid line but as seen from the back camera. A clear Ti-K α peak is visible together with the Ti K-edge at about 5 keV. Bremsstrahlung is clearly reduced.

intensity are shown. K α radiation can be seen clearly only from the back camera or in regions relatively distant from maximum. Bremsstrahlung radiation is the dominant source for the front camera. A possible role of directional bremsstrahlung (see [Sentoku et al., 1998; Sheng et al., 2000]) cannot be excluded: in fact the two cameras are set at 45° symmetrical with respect to the target surface. The laser angle of incidence of 75° can permit the front camera to see much more bremsstrahlung than the back camera.

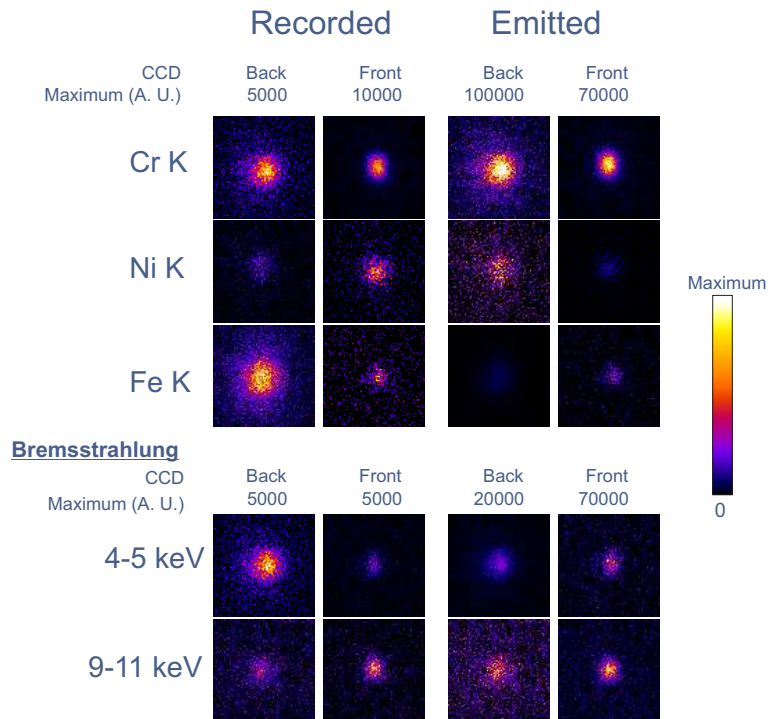


Figure 6.4: 2D images of the $K\alpha$ sources of Cr, Ni and Fe together with bremsstrahlung emissions in two different ranges as seen by the two CCDs. In the images belonging to the “emitted” column the absorption of the $K\alpha$ radiation, through target layers, filters etc., was taken into account. The maximum of the color scale is reported in each case. The dimension of each image is $180 \times 180 \sqrt{2} \mu\text{m}^2$.

6.4 Layered Target: Results

We also used a layered target, composed by $1.2 \mu\text{m}$ Cr + $10.9 \mu\text{m}$ Ni + $10 \mu\text{m}$ Fe¹, with laser pulses impinging on the Cr side. To be able to work in single photon regime attenuation filters (12 sheets of $50 \mu\text{m}$ thick mylar) were put between the front camera and the source. No filtering was needed for the back camera. Due to the energy resolution of about 200 eV (for CCD cooled down to -70°C), and the low number of photons in the source region, by adding many single shot images (1600 for Fig. 6.4) an energy resolved 2D imaging of the X-ray source at relativistic intensity was possible.

¹The Fe layer contained also about 10–15% Ni and Cr.

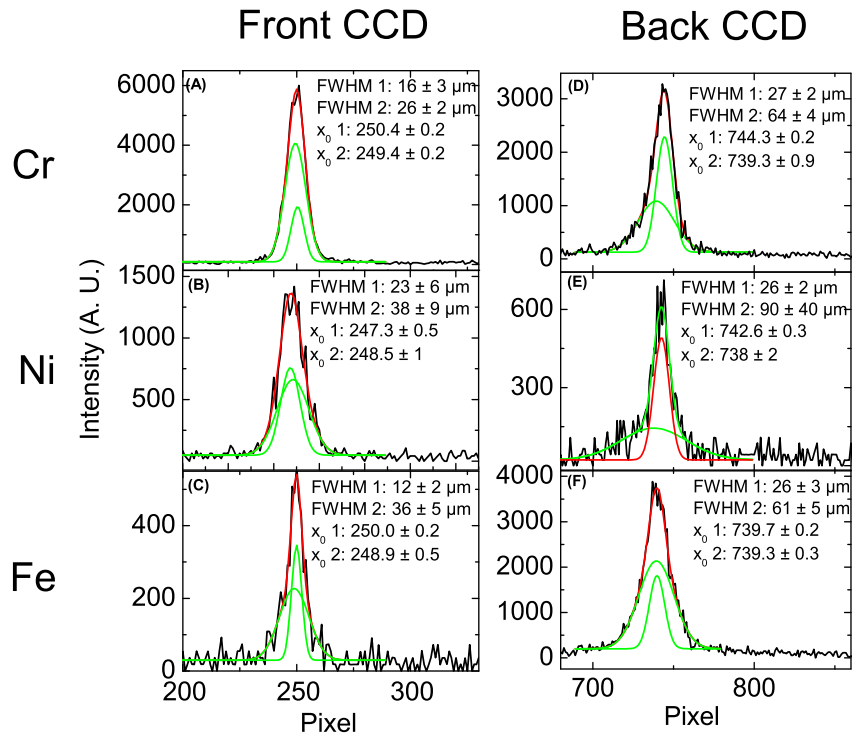


Figure 6.5: Horizontal lineout of the $K\alpha$ sources as recorded by the front and back CCDs, together with a fit performed with two Gauss functions. We show also the FWHMs of the two fitting functions and their position (x_0). The label “1” refers to the narrower curve. Note that the values of the FWHM does not consider possible effects coming from the geometry (angle of sight: 45°) or target thickness. For the sake of clarity, data concerning the bremsstrahlung images were not shown but are reported, in concise form, in Table 6.1.

In Fig. 6.4 the results of the X-ray source image reconstruction are reported. In the column “recorded” the images are shown as they were acquired by the CCDs; in the column “emitted” corrections for the absorption through filters and the different target layers were applied. The upper part of the panel shows the X-ray sources acquired in an energy window around a $K\alpha$ line (± 230 eV). In the lower panel we concentrated to regions of the spectrum where no spectral lines are present: those images are concerning only bremsstrahlung photons. To increase the number of collected photons a range much

broader than the CCD energy resolution was chosen. The energies involved are directly lower than the Cr-K α and higher than Ni-K α . Higher energies would have meant lower resolution because of the 2.5 μm thick Pt pin-hole and lower energies would have been too strongly absorbed by the filters.

We traced horizontal lineouts of the reconstructed images (shown in Fig. 6.5 together with fits made with two Gauss functions) to be able to resolve the different positions of the source: since the observation angle is 45°, different positions on the CCD correspond to different positions, i. e. depths, on the target. We made connections between fitted curves and origin of the sources by observing the FWHM and the positions (the x_0 's). The basic idea is that one fitting Gaussian should be related with one kind of emission (either bremsstrahlung or K α) from a specific layer. Two Gaussians were needed to well reproduce the emission features.

From Fig. 6.6 one can get a clearer overview in the X-ray emission structure. There, a series of sources is shown (the coloured ellipses) together with their dimensions, their origin (referring to Fig. 6.5) and the position on the CCD (which is directly related to the depth in the target).

Some words about the numbers given to indicate the position, they are the positions in pixel directly read from the CCD. A layer 1 μm thick (Cr is 1.2 μm), seen from 45 degrees, considering a magnification factor $M=11$ and the pixel dimension, about 26 μm , appears 0.3 pixel thick ($10 \mu\text{m} \approx 3 \text{ pixel}$)²

As an example, let us consider the emission on top. It is labeled as “Cr, Fe Front”: it means that, looking this emission in Fig. 6.5 (FWHM $\approx 14 \mu\text{m}$), can be found in the Cr and in the Fe source, as observed by the front CCD. We can reliably state that they come from the top of the target by observing their position: 250.4 ± 0.2 and 250.0 ± 0.2 pixel. The values for the positions of the other sources are all smaller, i. e. deeper in the target.

In the same way we note that the Fe source recorded by the front CCD (Fig. 6.4) is an artifact: its position (250.0 ± 0.2 and 248.9 ± 0.5 pixel read from Fig. 6.5; the Fe emission

²The sub-pixel resolution can be achieved by considering the Gaussian distribution used to fit the X-ray source. The errors bars are calculated by the fitting routine.

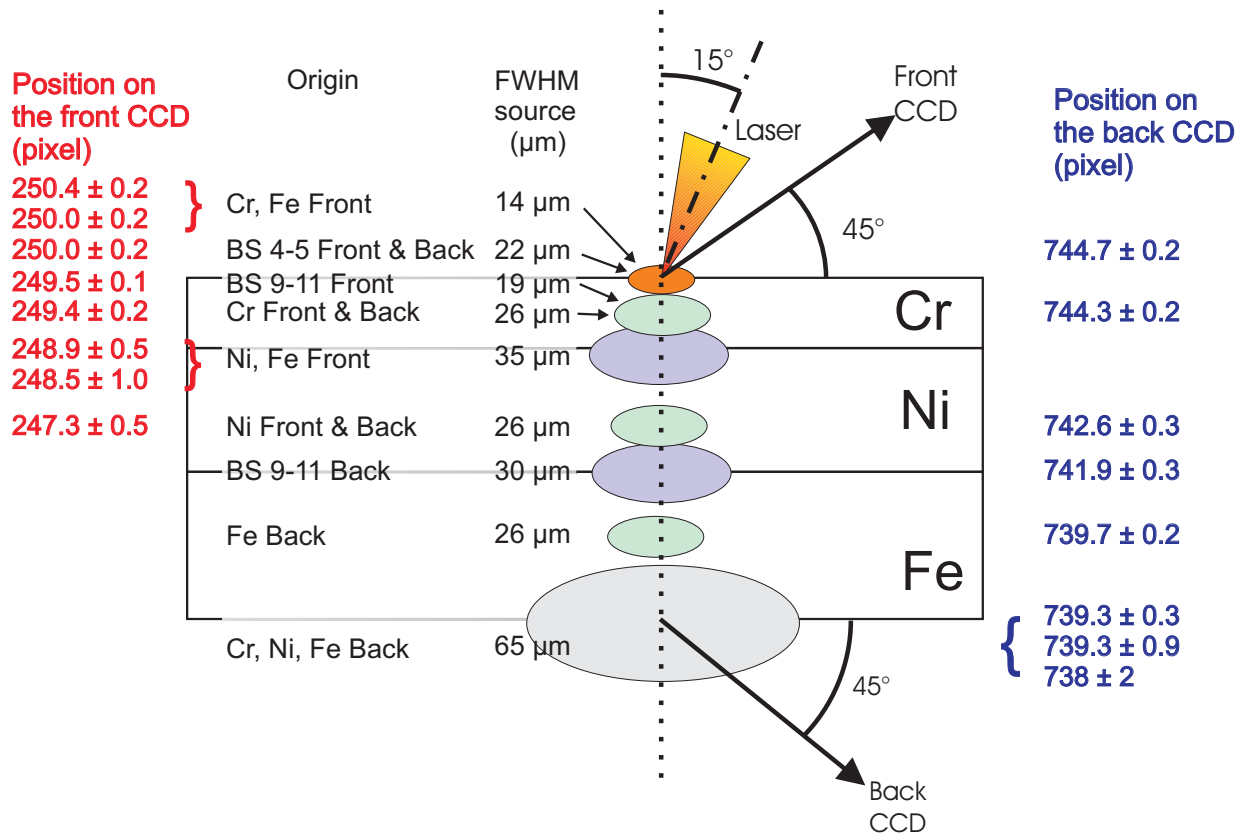


Figure 6.6: Overview of Fig. 6.5 with possible geometrical and physical explanation. The ellipses under the laser focal positions are the different sources at different positions on the CCD, i. e. depths. In the columns on left hand side the FWHM, the lineout (the kind of source; BS means bremsstrahlung) they come from and the position on the front CCD (as obtained by fitting the horizontal lineout) are given: they are at the same height of the sources they are referring to. In blue, right column, the same for the positions on the back CCD.

should be deeper) suggests that it consists of bremsstrahlung emission, with 6.4 keV energy, coming from the Cr and Ni layer (see later on). Support for this explanation comes from Fig. 6.7; the spectra seen by the two CCDs are plotted. The front CCD spectrum has no Fe- $K\alpha$ peak.

There are interesting features in the X-ray emission to be mentioned. The source on the target surface (laser side, orange ellipse) is the smallest, $\approx 14 \mu\text{m}$, and is seen only from the front CCD, in two different energy ranges (lineout A and C in Fig. 6.5): in both cases

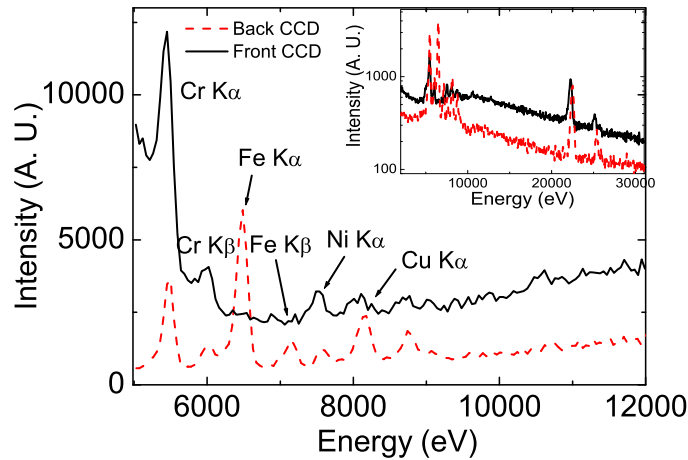


Figure 6.7: Spectra acquired by the CCDs working in single photon regime corrected for the filter used and the CCD quantum efficiency. Note the absence of Fe-K α on the front CCD. As already explained the Fe source seen by the first CCD was an artifact: now we see the absence of the line. In the inset, not corrected, a larger portion of the spectrum. The peaks at ≈ 25 keV are due to Ag present in the CCD circuitry.

the FWHM is similar ($16 \pm 3 \mu\text{m}$ and $12 \pm 2 \mu\text{m}$) and the positions are also corresponding (250.4 ± 0.2 and 250.0 ± 0.2 pixel). From the extremely small dimensions of the source, from the fact that its position is the closest to the surface, and that its emission is not seen from the back target (as already seen in Sec. 6.3), we think that this is bremsstrahlung, caused by energetic electrons close to the surface³. A bremsstrahlung source (4-5 keV) is seen in any case in the higher regions of the target (labeled with “BS 4-5 Front & Back”) even if with larger FWHM.

Another interesting feature is the relatively large emission region at the back side of the target (gray ellipse). It is seen only from the back CCD (lineout D, E and F in Fig. 6.5). In all the three cases FWHM and position coincide. It should be caused by the colossal electric fields created by the space charge [Romagnani et al., 2005] at the back side of the

³We emphasize the fact that a K α photon cannot be distinguished by a bremsstrahlung photon having the same energy

CCD	Energy (keV)	Position (pixel)	FWHM (μm)
Front	4–5	250.0 ± 0.2	21.8 ± 1.0
Front	9–11	249.5 ± 0.1	19.5 ± 0.8
Back (*)	4–5	740.7 ± 0.6	54 ± 3
Back (*)	4–5	744.7 ± 0.2	24 ± 2
Back	10–11	741.9 ± 0.3	30 ± 2

Table 6.1: Values of the peak position and FWHM for the different bremsstrahlung images as obtained from a fit with one (two for (*) case) Gauss function.

target: electrons are pulled back by such fields, not necessarily in the same point where they escaped the target (hence the broader emission) and create $K\alpha$ radiation. We remind that the Fe layer contained also about 15% of Ni and Cr. We come now to what we believe to be the “normal” $K\alpha$ radiation (green ellipses): electrons, with energies ranging from tens of keV up to tens of MeV, in their path through the target ionize the K-shell, recombination takes place and $K\alpha$ photons are emitted. The main characteristic of this emission is that it was recorded in all the three layers. It was seen by both cameras and, with very good reproducibility, has the same FWHM of about $26 \mu\text{m}$.

An unusually large emission (front CCD, purple ellipse) is seen between the $K\alpha$ emissions in Cr and Ni layer⁴. Because of its position, it is believed to be caused by magnetic fields induced by the resistivity change at the interface Cr-Ni, through the term $\mathbf{j}_{fast} \times \nabla\eta$ which bent the original electron trajectories in the target [Bell et al., 1998; Fuchs et al., 2003; Evans, 2006]. The idea is that electrons propagating in the target feel the resistivity change and, if they are not going exactly perpendicular to the interface, they build very intense magnetic fields. These fields, in turn influence the electron trajectories. Bremsstrahlung emission is believed to be created. We emphasize that the emission

⁴If we assume that the Cr $K\alpha$ emission takes place at about 249.5 (green ellipse), the purple ellipse is half pixel lower $\approx 1 \mu\text{m}$. This should be approximately the interface region between Cr and Ni.

recorded by the CCD should also have been bremsstrahlung because, in addition to Ni-K α also photons with Fe-K α energy are recorded; but in that region there is no Fe.

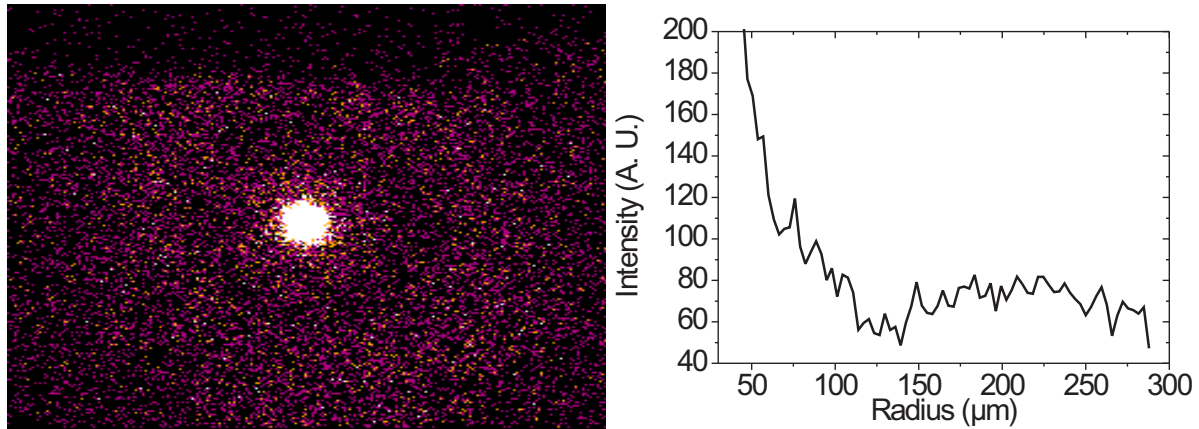


Figure 6.8: Halo of Cr-K α as seen from the front CCD. The dimension is $600 \mu\text{m} \times 900 \mu\text{m}$ (already corrected for the 45 degrees observation angle). A radial lineout is also presented.

There is a similar emission, probably at the Ni-Fe interface, seen by the back camera (pixel 741.9 ± 0.3). It's reasonable to assume that we are dealing with a source caused by a $\mathbf{j}_{fast} \times \nabla\eta$ magnetic field. The source dimension is $5 \mu\text{m}$ smaller but, while in the other case we had a good conductor – bad conductor transition, here the situation is opposite.

In Fig. 6.8 we show a weak ring-like halo surrounding the Cr-K α source. It is seen only by the front CCD and only with this energy: it could be the same halo observed in [Reich et al., 2003; Burgess et al., 1985; Luther-Davies et al., 1987]. It comes from the upper target layer and it could be caused by the presence of magnetic fields which bend the electron trajectories to regions hundreds μm away from the focal spot.

6.5 Conclusion

- For the first time an energy resolved 2D imaging of an X-ray source at relativistic intensities was done.

- By considering the FWHM of the green ellipses, and taking the error bars into account a maximal divergence of 0.15 rad can be obtained. The electron stack spectrometer gave a value of 0.7 rad. A plausible explanation for this is that the presence of space charge with electric fields of the order of TV/m at the back side of the target could have strongly influenced the electron beam features.
- We find an about $60 \mu\text{m} (\times\sqrt{2})$ diameter halo at the back of the target, we attribute this to reflux effects of the space charge fields. A much weaker and broader ring (some hundreds of μm) was found at the front side.
- We could monitor the bremsstrahlung emission. It comes mainly from the top layer and from interface regions.
- We see a broad ($30\text{--}35 \mu\text{m} \times\sqrt{2}$) bremsstrahlung emission at the two interfaces, with both cameras. We believe to have seen for the first time directly the influence of the $\mathbf{j}_{fast} \times \nabla\eta$ term of the magnetic field on the electron motion *in* the target [Bell et al., 1998]. This term, originating from a change in resistivity, can give rise to tens of kT magnetic fields and be able to bend electron trajectories in the target. This results in a bremsstrahlung emission caused by the bending. Note that this source is clearly larger than the “normal” $K\alpha$ source.⁵

⁵Is it possible that in other experiments, e. g. [Wharton et al., 1998; Stephens et al., 2004], based on buried fluor materials, this term could have negatively influenced the results, as already anticipated by [Bell et al., 1998]?

We put here some idea together, taken from the different chapters. The aim is to mix the knowledge from one experiment to elucidate not perfectly understood sides of another experiment.

1. In Fig. 5.5 we reported a comparison polarized – nonpolarized spectra for different distances (offsets) from the maximum intensity. Even if we were dealing with a $2\ \mu\text{m}$ thick Ti foil target, we had that the comparison polarized–nonpolarized spectra gave a hint at an anisotropic electron velocity distribution for distances of tens of μm . A possible interpretation of this can come again from the halo in the target back side. It is commonly believed to be caused by the space charge separation created by the electrons: there electric fields of $10^{12}\ \text{V/m}$ are generated and are responsible for the proton acceleration, for example. The idea is now that the positively charged target pulls the electrons back: this happens in a larger region than the original electron path (hence the halo is larger than the “normal” $K\alpha$ emission) and they acquire enough energy to create $K\alpha$ radiation. The spectropolarimetry sees a beam-like electron distribution, but the electrons are traveling now in the opposite direction. Support for this could come from time resolved measurements.
2. The stack electron spectrometer measured a total amount of electrons of about 10^{10} (for the $25\ \mu\text{m}$ thick Ti foils). This is approximately two orders of magnitude lower than needed to explain a 10 kT magnetic field. The electron transport inhibition played here a major role: no other explanation can be taken into account if we consider that we had 10^{10} photons from the source (see Sec. 4.4).

-
3. The stack electron spectrometer gave for the experiment in Chapter 6 measured a divergence of about 0.7 rad. If the assumption that the green ellipses in Fig. 6.6 are correctly representing the path of the fast electrons in the target, then we must conclude that the stack spectrometer has suffered a strong influence from the TV/m electric fields at the back side of the target. Even assuming a slightly divergent beam, ~ 0.1 rad considering the error bars, the features recorded by the stack spectrometer are only weakly connected with the characteristics of the electron beam *inside* the target.
 4. As already mentioned, there are return currents that can greatly influence the physics of the electron transport in the cold matter but they are not recognizable. The electrons belonging to them, can have energies of \sim keV, i. e. they can create $K\alpha$ radiation but there is no chance to identify them in a non-ambiguous way, to distinguish them from the more energetic, forward currents.
 5. Eq. 2.6 states that, for our experimental conditions, the fast current amounts to ~ 200 MA. Our simple estimation in Chapter 4 gave 1.6 MA as a result. As calculated in [Sentoku et al., 2002], the fast–return current compensation is always almost perfect; the difference of two orders of magnitude found here could be seen as an “almost perfect” compensation and accounts for, at least partially, the measured magnetic field. An additional hint for this, is given by the fact that the exponent in the simulated radial dependence of the magnetic field (we remind $\propto 1/r^\gamma$) was smaller than 1. If return currents had played a major role in the measured magnetic field, it should have been $\gamma \gg 1$ (for perfect compensation $\gamma = \infty$ and $B \neq 0$ only for the portion of space where the currents flow).

In this thesis the behaviour of electrons in solid density targets in a wide energy range (4 keV...14 MeV) as a result of laser-plasma interactions at relativistic intensities was investigated. Ultra-intense ultra-short laser pulses were tightly focused up to intensities of $5 \cdot 10^{19}$ W/cm² on a target and the X-ray emission was observed by means of a high-resolution spectrometer ($E/\Delta E \approx 15000$) with 1D imaging capabilities coupled with a polarizer, in one case, or of an energy resolving 2D X-ray imaging system, in the other case.

Ti-K α lines were monitored and a clear intensity dependent symmetrical line broadening was observed. Calculations performed at the Weizmann Institute (Israel), could exclude an influence of Stark and Doppler effect. Careful analysis of the data, observation of symmetries of the broadening and the absence of a significant line shift could rule out also the presence of satellites in the line shape leaving only magnetic fields to account for the observed changes. Thus, we could observe for the first time in laboratory the Zeeman effect in the X-ray regime caused by the extremely strong magnetic fields created in the laser-plasma interaction and by the electron propagation in the “cold” target. We stress the fact that the line broadening is observed by comparing two spectra acquired with different laser intensities but also by considering, in the very same spectral image, two scans (spectra) with different distances from the region of maximum intensity. The averaged measured magnetic field amounts to about 10 kT; simulations gave an estimate for the peak magnetic field: 18 ± 5 kT. Moreover, for the first time it was possible to detect magnetic field in the solid density plasma; to my knowledge this is not possible with any

other method known at the moment.

In the second part of this thesis, the use of an X-ray polarizer coupled with the high-resolution X-ray spectrometer, allowed the study of the polarization properties of Ti-K α line satellites. A strong polarization dependence of the satellites was observed. Further, the polarized spectrum evolution as a function of the distance from the peak of the laser intensity was determined. If the influence of electric and magnetic field are neglected, the polarization dependence is strictly connected with the beam-like characteristics of the electrons propagating in the target; hence these results could demonstrate the presence of strongly anisotropic processes *inside* the laser-irradiated targets and this technique can be successfully employed to study the electron transport properties under such extreme conditions.

Finally, energy resolved 2D images of a laser-plasma produced X-ray source, for the first time, were obtained. Impressive differences in intensity and source dimension between the front and the back side of the target, even for very thin foils, were found. The use a three layer target together with the possibility to observe the same source at different energies with 5 μm spatial resolution, allowed quantitative statements about the source features.

- Different types of emission could be recognized, at different depths with different dimensions, between 14 and more 65 μm .
- The target geometry together with the high spatial resolution suggested a possible structure for the many X-ray emissions.
- We believe to have observed, for the first time, the interfacial emission induced by the magnetic field created by the term $\mathbf{j}_{fast} \times \nabla\eta$, due to a change in the resistivity. These giant fields by bending the electron trajectories, induce bremsstrahlung emission.
- A maximal divergence of 0.15 rad can be obtained for the electron beam in the target. The electron stack spectrometer gave a value of 0.7 rad. A plausible explanation for this is that the presence of space charge with electric fields of the order of TV/m at

the back side of the target could have strongly influenced the electron beam features.

- A about 90 μm diameter halo at the back of the target was measured, we attribute this to reflux effects of the space charge fields. A much weaker and broader ring (some hundreds of μm) was found at the front side.

Bibliography

NRL Plasma Formulary. Naval Research Laboratory, Washington, DC 20375, 2006.

J. C. Adam, A. Heron, and G. Laval. *Phys. Rev. Lett.*, 97:205006, 2006.

E. V. Aglitskii et al. *J. Phys. B*, 15:2001, 1982.

H. Alfven. *Phys. Rev.*, 55:425, 1939.

F. Amiranoff et al. *Phys. Rev. Lett.*, 81:995, 1998.

A. Authier. *Dynamical Theory of X-Ray Diffraction*. Oxford University Press, 2003.

M. Bargheer et al. *Science*, 306:1771, 2004.

D. Batani et al. *Phys. Rev. E*, 65:066409, 2002.

D. Batani et al. *Phys. Rev. Lett.*, 94:055004, 2005.

F. N. Beg et al. *Phys. Plasmas*, 4:447, 1996.

P. Beiersdorfer et al. *Phys. Rev. A*, 60:4156, 1999.

A. R. Bell, R. G. Evans, and D. J. Nicholas. *Phys. Rev. Lett.*, 46:243, 1981.

- A. R. Bell, J. R. Davies, S. Guerin, and H. Ruhl. *Plasma Phys. Control. Fusion*, 39:653, 1997.
- A. R. Bell, J. R. Davies, and S. M. Guerin. *Phys. Rev. E*, 58:2471, 1998.
- A. R. Bell et al. *Plasma Phys. Control. Fusion*, 48:R37, 2006.
- T. V. M. Bootsma et al. *Nucl. Instr. and Meth. A*, 439:575, 2000.
- M. Borghesi et al. *Phys. Rev. Lett.*, 80:5137, 1998a.
- M. Borghesi et al. *Phys. Rev. Lett.*, 81:112, 1998b.
- M. Borghesi et al. *Phys. Rev. Lett.*, 83:4309, 1999.
- A. Bret, M.-C. Firpo, and C. Deutsch. *Phys. Rev. Lett.*, 94:115002, 2005.
- F. Brunel. *Phys. Rev. Lett.*, 59:52, 1987.
- M. D. J. Burgess, B. Luther-Davies, and K. A. Nugent. *Phys. Fluids*, 28:2286, 1985.
- S. Busch et al. *Appl. Phys. Lett.*, 82:3354, 2003.
- A. H. Compton and S. K. Allison. *X-Rays in Theory and Experiment*. van Nostrand, New York, 2nd ed. edition, 1954.
- T. E. Cowan et al. *Phys. Rev Lett.*, 84:903, 2000.
- J. R. Davies, A. R. Bell, M. G. Haines, and S. M. Guerin. *Phys. Rev. E*, 56:7193, 1997.
- M. Deutsch et al. *Journal of Research of NIST*, 109:75, 2004.
- M. Deutsch et al. *Phys. Rev. A*, 51:283, 1995.
- T. Ditmire et al. *Nature (London)*, 398:489, 1999.
- R. C. Duncan and C. Thompson. *Astrophys. J.*, 392:L9, 1992.
- R.G. Evans. *High Energy Density Physics*, 2:35, 2006.
- F. Ewald, H. Schwoerer, and R. Sauerbrey. *Europhys. Lett.*, 60:710, 2002.

- A. K. Freund F. N. Chukhovskii, M. Krisch. *Rev. Sci. Instrum.*, 63:920, 1992.
- R. Fabbro and P. Mora. *Phys. Lett.*, 90A:48, 1982.
- A. Ya. Faenov et al. *Physica Scripta*, 50:333, 1994.
- J. Faure et al. *Nature (London)*, 421:541, 2004.
- T. Feurer et al. *Phys. Rev. E*, 65:016412, 2001.
- T. Feurer et al. *Phys. Rev. E*, 56:4608, 1997.
- D. W. Forslund and J. U. Brackbill. *Phys. Rev. Lett.*, 48:1614, 1982.
- E. Förster. 1985.
- E. Förster, K. Gäbel, and I. Uschmann. *Laser and Particle Beams*, 9:135, 1991.
- J. Fuchs et al. *Phys. Rev. Lett.*, 91:255002, 2003.
- T. Fujimoto and S. A. Kazantsev. *Plasma Phys. Control. Fusion*, 39:1267, 1997.
- S. Bulanov G. Mourou, T. Tajima. *Rev. Mod. Phys.*, 78:309, 2006.
- M. Galimberti et al. *Rev. Sci. Instrum.*, 76:053303, 2005.
- J.-C. Gauthier et al. *Phys. Rev. E*, 52:2963, 1995.
- C. G. R. Geddes et al. *Nature (London)*, 421:538, 2004.
- P. Gibbon et al. *Plasma Phys. Control. Fusion*, 38:769, 1996.
- L. Gremillet et al. *Phys. Rev. Lett.*, 83:5015, 1999.
- D. E. Groom. In *Optical and IR telescope instrumentation and detectors*, volume 4008, page 634. Proc. SPIE, 2000. LBNL-45277.
- D. E. Groom et al. *Nucl. Instr. and Meth. A*, 442:216, 2000.
- D. E. Groom et al. In *Proc. 4th ESO Workshop on Optical Detectors for Astronomy*, pages LBNL-45276. Kluwer Academic Publishers, 1999.

- S.L. Gruner, M.W. Tate, and E.F. Eikenberry. *Rev. Sci. Instrum.*, 73:2815, 2002.
- S. M. Guerin et al. *Plasma Phys. Control. Fusion*, 41:285, 1999.
- P. Hakel et al. *Phys. Rev. E*, 69:056405, 2004.
- S. B. Hansen et al. *Phys. Rev. E*, 72:036408, 2005.
- K. Hashimodotani et al. *Rev. Sci. Instr.*, 69:3746, 1998.
- A. Hauer, J. D. Kilkenny, and O. L. Landen. *Rev. Sci. Instrum.*, 56:803, 1985.
- B. M. Hegelich et al. *Nature (London)*, 439:441, 2006.
- M. Hegelich et al. *Phys. Rev. Lett.*, 89:085002, 2002.
- K. W. Hill et al. *Phys. Rev. A*, 13:1334, 1976.
- J. Hiraga, H. Tsunemi, and E. Miyata. *Jpn. J. Appl. Phys.*, 40:1493, 2001.
- S. E. Holland et al. *IEEE Trans. Electron Devices*, 50:225, 2003.
- M. Honda, J. Meyer-ter-Vehn, and A. Pukhov. *Phys. Plasmas*, 7:1302, 2000.
- J. R. Janesick. *Scientific charge-coupled devices*. SPIE Press, Bellingham Washington, 2001.
- H.H. Johann. *Z. Phys.*, 69:185, 1931.
- T. Johansson. *Z. Phys.*, 82:507, 1933.
- D. C. Joy. *Monte Carlo modeling for electron microscopy and microanalysis*. Oxford University Press, Oxford, 1995.
- M. Kaluza et al. *Phys. Rev. Lett.*, 92:045003, 2004.
- B. E. Kane et al. *Rev. Sci. Instrum.*, 68:3843, 1997.
- A. Karcher et al. *IEEE Trans. Nucl. Sci.*, 51:5, 2004.
- S. B. Kemic. *Astrophys. J.*, 193:213, 1974.

- M. H. Key et al. *Phys. Plasmas*, 5:1966, 1998.
- J. C. Kieffer, H. Pepin, and F. Amiranoff. *Appl. Phys. Lett.*, 44:494, 1984.
- J. C. Kieffer et al. *Phys. Rev. Lett.*, 68:480, 1992.
- J. C. Kieffer et al. *Phys. Rev. E*, 48:4648, 1993.
- J. A. Koch et al. *Phys. Rev. E*, 65:016410, 2001.
- R. Kodama et al. *Nature (London)*, 412:798, 2001.
- R. Kodama et al. *Nature (London)*, 418:933, 2002.
- M. Kopecky. *Rev. Sci. Instrum.*, 66:4921, 1995.
- L. Labate et al. *Nucl. Instrum. Methods A*, 495:148, 2002.
- K. W. D. Ledingham et al. *Science*, 300:1107, 2003.
- F. Livet et al. *Nucl. Instr. and Meth. A*, 451:596, 2000.
- A. Lübcke et al. *Appl. Phys. B*, 80:801, 2005.
- B. Luther-Davies, A. Perry, and K. A. Nugent. *Phys. Rev. A*, 35:4306, 1987.
- R. C. Malone, R. L. McCrory, and R. L. Morse. *Phys. Rev. Lett.*, 34:721, 1975.
- S. P. D. Mangles et al. *Nature (London)*, 421:535, 2004.
- E. Martinolli et al. *Phys. Rev. E*, 73:046402, 2006.
- R. J. Mason and M. Tabak. *Phys. Rev. Lett.*, 80:524, 1998.
- J. P. Matte and J. Virmont. *Phys. Rev. Lett.*, 49:1936, 1982.
- T. Missalla et al. *Rev. Sci. Instrum.*, 70:1288, 1999.
- A. Modena et al. *Nature (London)*, 377:606, 1995.

- P. H. Mokler and F. Folkmann. *X-ray production in heavy ion-atom collisions in "Structure and collisions of ions and atoms*, volume 5. Berlin and New York, Springer-Verlag, 1978.
- A. Morak et al. *Physica Status Solidi B*, 243:2728, 2006.
- S. Morita et al. *Phys. Lett.*, 94:147, 1983.
- F. Pisani et al. *Phys. Rev. E*, 62:5927, 2000.
- L. Poletto, A. Boscolo, and G. Tondello. *Appl. Opt.*, 38:29, 1999.
- G. Pretzler et al. *Appl. Phys. Lett.*, 82:3623, 2003.
- G. Pretzler et al. *Phys. Rev. E*, 58:1165, 1998.
- G. Prigozhin et al. *IEEE Trans. on Electron Devices*, 50:246, 2003.
- A. Pukhov and J. Meyer-ter-Vehn. *Phys. Rev. Lett.*, 76:3975, 1996.
- A. Pukhov and J. Meyer-ter-Vehn. *Appl. Phys. B*, 74:355, 2002.
- A. Raven, O. Willi, and P. T. Rumsby. *Phys. Rev. Lett.*, 41:554, 1978.
- C. Reich. PhD thesis, Friedrich Schiller University Jena, Germany, 2002.
- Ch. Reich et al. *Phys. Rev. Lett.*, 84:4846, 2000.
- Ch. Reich et al. *Phys. Rev. E*, 68:056408, 2003.
- C. Rischel et al. *Nature (London)*, 390:490, 1997.
- L. Romagnani et al. *Phys. Rev. Lett.*, 95:195001, 2005.
- F. B. Rosmej et al. *J. Quant. Spectrosc. Radiat. Transfer*, 65:477, 2000.
- A. Rouse, C. Rischel, and J.-C. Gauthier. *Rev. Mod. Phys*, 73:17, 2001a.
- A. Rouse et al. *Nature (London)*, 410:65, 2001b.
- A. Rouse et al. *Phys. Rev. E*, 50:2200, 1994.

- W. Rozmus and V. T. Tikhonchuk. *Phys. Rev. A*, 42:7401, 1990.
- A. S. Sandhu et al. *Phys. Rev. Lett.*, 89:225002, 2002.
- A. S. Sandhu et al. *Phys. Rev. E*, 73:036409, 2006.
- M. Sarfaty et al. *Phys. Plasmas*, 2:2583, 1995.
- H. Schwoerer et al. *Phys. Rev Lett.*, 86:2317, 2001.
- H. Schwoerer et al. *Nature (London)*, 439:445, 2006.
- Y. Sentoku, K. Mima, S. Kojima, and H. Ruhl. *Phys. Plasmas*, 7:689, 2000.
- Y. Sentoku, K. Mima, P. Kaw, and K. Nishikawa. *Phys. Rev. Lett.*, 90:155001, 2003.
- Y. Sentoku et al. *Phys. Rev. E*, 65:046408, 2002.
- Y. Sentoku et al. *Phys. Plasmas*, 5:4366, 1998.
- Z. M. Sheng et al. *Phys. Rev. Lett.*, 85:5340, 2000.
- G. N. Shigeoka et al. *Phys. Rev. A*, 69:052505, 2004.
- A. S. Shlyaptseva et al. *Rev. Sci. Instrum.*, 74:1947, 2003.
- A. S. Shlyaptseva et al. *Rev. Sci. Instrum.*, 68:1095, 1997.
- M. Siegbahn and W. Stenström. *Phys. Zeitschr.*, 17:318, 1916.
- K. Sokolowski-Tinten et al. *Nature (London)*, 422:287, 2003.
- L. Spitzer and R. Härm. *Phys. Rev.*, 89:977, 1953.
- E. Stambulchik and Y. Maron. *J. Quant. Spectrosc. Radiat. Transfer*, 99:730, 2006.
- J. A. Stamper et al. *Phys. Rev.*, 26:1012, 1971.
- R. B. Stephens et al. *Phys. Rev. E*, 69:066414, 2004.
- R. J. Stover et al. volume 3019, page 183. Proc. SPIE, 1997.

- D. Strickland and G. Mourou. *Opt. Commun.*, 56:219, 1985.
- L. Strüder. *Nucl. Instr. and Meth. A*, 454:73, 2000.
- R. N. Sudan. *Phys. Rev. Lett.*, 70:3075, 1993.
- M. Tabak et al. *Phys. Plasmas*, 1:1626, 1994.
- S. Takagi. *Acta Crystallographica*, 15:1311, 1962.
- M. Tatarakis et al. *Nature (London)*, 415:280, 2002.
- M. Tatarakis et al. *Phys. Rev. Lett.*, 90:175001, 2003.
- M. Tatarakis et al. *Phys. Rev. Lett.*, 81:999, 1998.
- D. Taupin. PhD thesis, University of Paris, 1964.
- U. Teubner et al. *Phys. Rev. E*, 54:4167, 1996.
- K. Torii, H. Tsunemi, E. Miyata, and K. Hayashida. *Nucl. Instr. Methods A*, 361:364, 1995.
- V. K. Tripathi and C. S. Liu. *Phys. Plasmas*, 1:990, 1994.
- J. Trümper et al. *Astrophys. J.*, 219:L105, 1978.
- H. Tsunemi et al. *Astrophys. J.*, 554:496, 2001.
- H. Tsunemi et al. *Nucl. Instr. and Meth. A*, 436:32, 1999.
- I. Uschmann et al. *J. Appl. Cryst.*, 26:405, 1993.
- L. Veisz et al. *Phys. Plasmas*, 11:3311, 2004.
- S. Volkmer. Master's thesis, Friedrich Schiller University, Jena, Germany, 2004.
- F. Walden et al. *Phys. Rev. E*, 59:3562, 1999.
- J. M. Wallace. *Phys. Rev. Lett.*, 55:707, 1985.
- E. S. Weibel. *Phys. Rev. Lett.*, 2:83, 1939.

K. B. Wharton et al. *Phys. Rev. Lett.*, 81:822, 1998.

S. C. Wilks et al. *Phys. Rev. Lett.*, 69:1383, 1992.

B. K. F. Young et al. *Rev. Sci. Instrum.*, 69:4049, 1998.

F. Zamponi, T. Kämpfer, A. Morak, I. Uschmann, and E. Förster. *Rev. Sci. Instrum.*, 76:116101, 2005.

F. Zamponi, A. Lübcke, T. Kämpfer, I. Uschmann, E. Förster, R. Sauerbrey, E. Kroupp, E. Stambulchik, D. Fisher, Y. Maron, B. Hidding, M. Clever, G. Pretzler, R. Sharon, and M. Deutsch. *High Energy Density Physics*, In Press, 2007.

P. Zeeman. *Philos. Mag.*, 43:226, 1897.

N. Zhavoronkov, Y. Gritsai, M. Bargheer, M. Woerner, Th. Elsaesser, F. Zamponi, I. Uschmann, and E. Förster. *Opt. Lett.*, 30:1737, 2005.

Ch. Ziener et al. *Phys. Rev. E*, 66:066411, 2002.

G. Zschornack. *Atomdaten für die Röntgenspektaranalyse*.

Appendix A

Characterization of the CCD

A.1 Introduction

In recent years the use of CCDs as detector for X-rays has been increasing [Gruner et al., 2002]. The constraint to have high QE together with high spatial resolution also in the range of 5-10 keV forced the development of detectors with new features [Strüder, 2000; Janesick, 2001]. After the advent of “Back-Illuminated” (BI) CCDs, since few years Deep Depletion (DD) CCDs are commercially available [Bootsma et al., 2000]. DD means that the sensitive region has been made thicker to increase the probability of an interaction between the impinging radiation and the detector [Holland et al., 2003; Groom, 2000; Groom et al., 2000; Stover et al., 1997]. Another stringent requirement that new generations of CCDs must fulfill is the capability of single photon detection: this means that every single detected photon must leave a clear track on CCD signal [Livet et al., 2000]. This is crucial for applications in Time Resolved X-ray Diffraction (TRXD) context [Rischel et al., 1997; Rouse et al., 2001a].

A.2 The Quantum Efficiency

The used device was a back-illuminated deep depletion ANDOR 420DX-BD-DD CCD. The chip consists of 256 times 1024 squared pixels of $26 \mu\text{m} \times 26 \mu\text{m}$ for a total available area of 6.7 mm times 26.6 mm.

The QE was tested with the setup shown in Fig.A.1 [Hashimodotani et al., 1998; Poletto et al., 1999]: the Bremsstrahlung radiation created in a tungsten X-ray tube, was sent on to the target (titanium, copper, iron, silver and tin were used). K shell fluorescence radiation was produced.

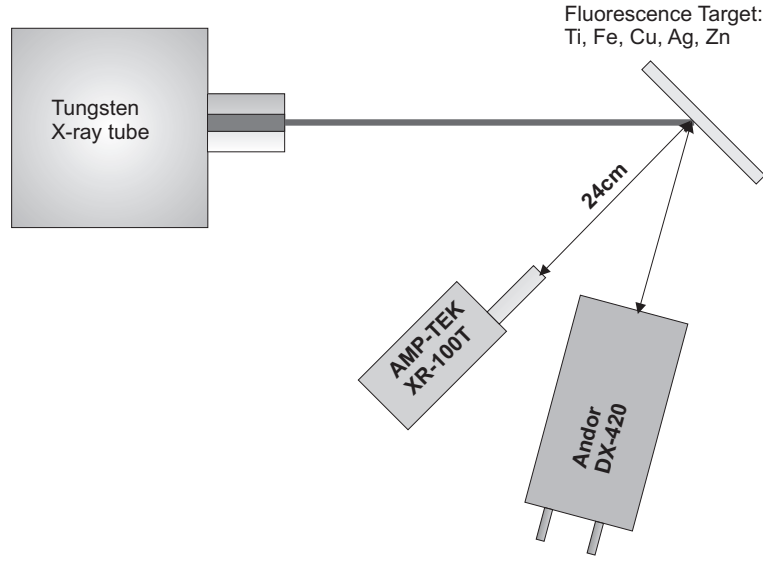


Figure A.1: *Experimental setup for the measurement of the quantum efficiency.*

The CCD and the AMP-TEK diode (a cooled silicon diode with known QE ¹) were put at the same distance from the target. In order to cool the CCD without having ice condensation on the chip, the CCD was put in a small vacuum chamber (pressure $\sim 10^{-5}$ mbar). The CCD was cooled down to -40 °C. We used a readout time of $16 \mu\text{s}$ corresponding to a conversion factor of $7 e^-$ per channel. The readout noise for this setting is $6 e^-$. To screen the chip from visible radiation 2 sheets of Al-coated Mylar were used. A Kapton window of $50 \mu\text{m}$ was the interface between vacuum and air.

The shutter, put in the primary beam, was open for 1 s. The CCD exposure time was 3 s. For Ti, Cu and Fe we set the X-ray tube to 20 kV and 10 mA. In order to excite K-lines for silver and tin we worked with 40 kV. To take into account the reduced QE of the CCD in that regime of energies we used a current of 30 mA.

The same parameters of the X-ray tube were also used for the AMP-TEK detector; in this case the shutter was open for about 60 s.

The CCD was working in “single photon regime” [Labate et al., 2002; Livet et al., 2000], i.e. the number of photons recorded by the CCD, N , was much smaller than the number of pixels, N_p . In our case $N/N_p \simeq 0.01$. Exploiting the fact that a photon interacting with the CCD

¹www.amptek.com

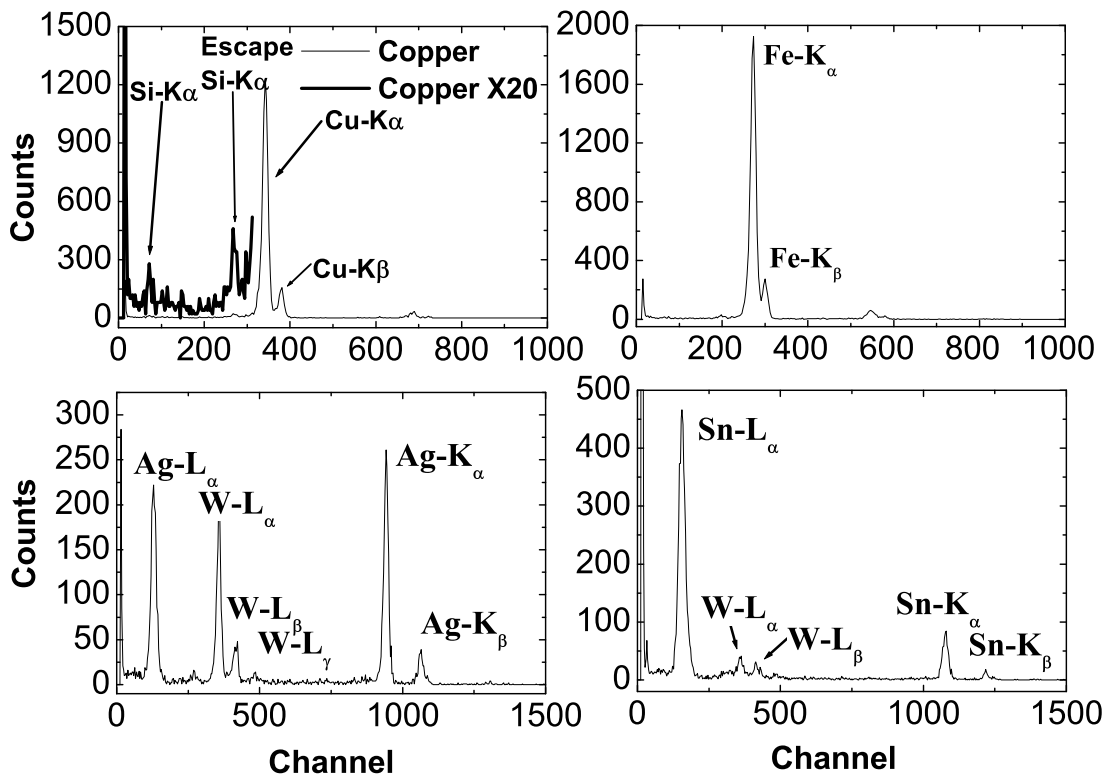


Figure A.2: Spectra of Cu, Fe, Ag and Sn are here shown. The thicker line is a 20 times magnification. Note that different scales were used.

creates a charge proportional to its energy, one can plot in a histogram excited channels vs. how often such channels appear. What is obtained is a spectrum of the impinging radiation; the CCD is working as a non-dispersive spectrometer. The reconstruction of split events was done by a program developed to recognize simple patterns. If a pattern was matching the distribution of the signal on different pixels then the values from these pixels were summed up to reconstruct the original signal.

All the images were background subtracted, in order to remove CCD imperfections and hot spots.

Fig. A.2 shows four of such spectra, for copper, iron, silver and tin, respectively. Each histogram is calculated by applying the program to three different images and then summing up

Table A.1: Percentage of events consisting of 1, 2, 3 or 4 pixels. The results of titanium, iron and copper are comparable and therefore grouped together. The same was done for silver and tin. More in the text.

pixels involved	Ti, Fe & Cu [%]	Ag & Sn [%]
1	57	47
2	36	41
3	4	6
4	3	6

the results. The thicker line in the Cu spectrum is a magnification to show the Si-K α peak and the escape peak (see [Strüder, 2000]).

Peaks at two times the photon energy are the “two photon events”: in one pixel or in a small region two photons impinged; the program recognized them as a single event and the signal was summed up to create a second fictitious peak.

Further, the program was used to plot histograms, that were made with reconstructed events concerning only 1, 2, 3 and 4 pixels. Events with a higher amount of involved pixels are very unfrequent. We report in fig. A.3 such histograms for titanium.

In table A.1 we report how often the pixel splitting appears. To do this, we divide the number of K α (and K β for Ti) events for 1, 2, 3 and 4 pixels by the total amount of K α (and K β for Ti) events. No noticeable differences between titanium, copper, iron were found. For these energies 57 % of the detected photons is recorded in one single pixel.

In order to measure the QE of the CCD for the different energies we compared the number of photons detected by the CCD and the AMP-TEK. For AMP-TEK an absolute calibration curve is available.

In fig. A.4a the results are reported. All the possible sources of attenuation were taken into account. The number of photons on the detector per unit area and time was determined. The estimated errors were 10% for titanium, iron and copper, due to fluctuations of the number of detected photons, and 20% for silver and tin because of the reduced sensitivity of both instruments

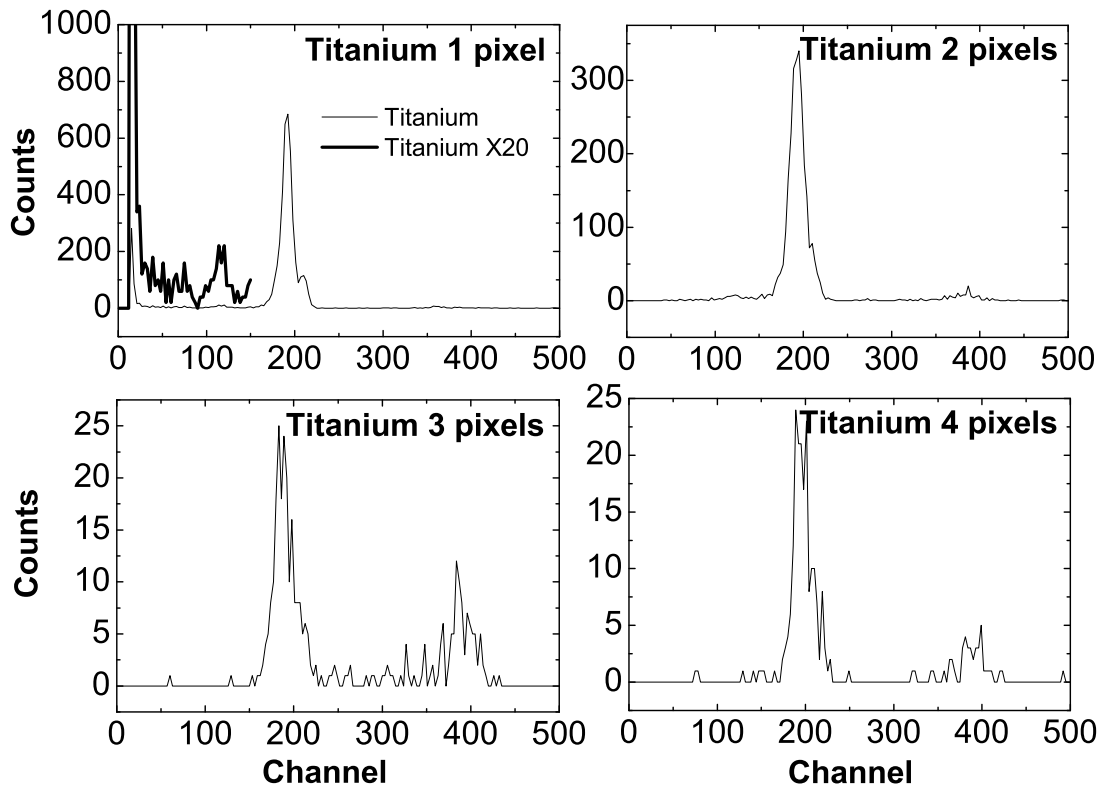


Figure A.3: The histograms for the four different kind of events are reported. Note the different scale on the four graphs. The thicker line is a 20 times magnification.

at such energies. For titanium and iron the AMP-TEK detector couldn't resolve $K\alpha$ and $K\beta$: the efficiency is then concerning photons belonging to both lines. The QE for $W-L\alpha$ and $W-L\beta$ is also reported. We found here much higher fluctuations in the number of photons detected by the AMP-TEK. The absorption of $40\ \mu\text{m}$ of silicon as a function of energy (solid line) is plotted. This is a measure of the CCD depletion region depth (and also of the CCD thickness: the CCD under exam was a BI), i.e. the depth of the region where the charge produced by an X-ray photon can be completely collected. The manufacturer gives an interval for such a value between $30\ \mu\text{m}$ and $50\ \mu\text{m}$.

An excellent sensitivity for $Ti-K\alpha$ is to be noticed. For $Cu-K\alpha$ the QE is almost 50%.

In fig. A.4b we plot the incoming photon energy vs. the channel number together with a

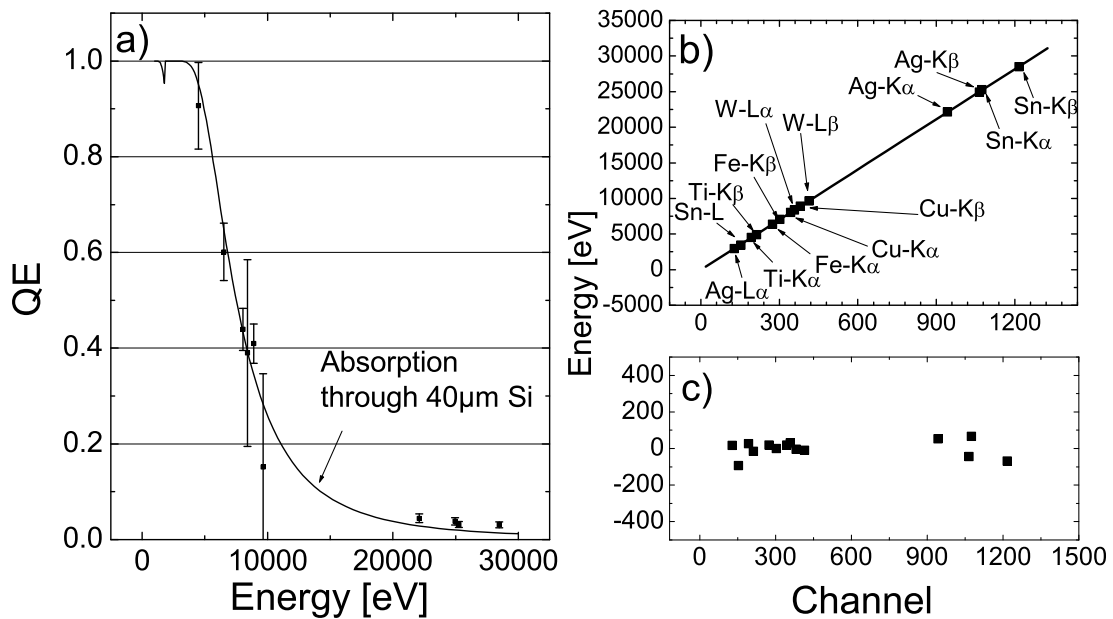


Figure A.4: In a) the measured QEs for the different energies under test are presented. We plot also (solid line) the absorption of 40 μm Si as a function of energy. This is the depletion region depth. In b) the channel value for very different photon energies is reported together with a linear fit. In c) the fit residuals are displayed. Note the different scales for the last 2 graphs.

linear fit. In fig. A.4c the fit residuals are shown: deviations from linearity are in the order of 0.2%.

By taking into account both Ti and Cu $K\alpha$ peaks, their “full width half maximum” (FWHM) value was found: $\Delta E_{FWHM} \sim 340$ eV. This is the energy resolution of the CCD at this temperature.

From [Strüder, 2000], the theoretical energy resolution for a silicon detector for such energy is 102 eV. The measured energy resolution is a factor 3 lower the theoretical value for a silicon detector: the high thermal noise of this kind of system could explain the reduced performance. The chip can anyway be cooled down to -70 °C.

A.3 Spatial resolution

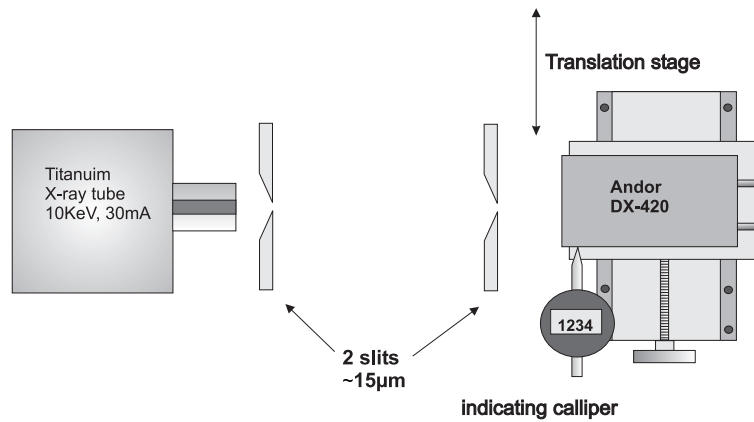


Figure A.5: *Experimental setup used to test the spatial resolution of the CCD.*

To test more carefully the spatial resolution of the CCD we performed an additional experiment [Tsunemi et al., 1999; Karcher et al., 2004]. The aim was to measure the charge cloud dimensions. As shown in Fig. A.5, we mounted the CCD on a translation stage, whose movement, parallel to the chip plane, could be accurately monitored by means of a caliper with about $2\ \mu\text{m}$ precision. The beam of an X-ray tube (Titanium target, 10 keV, 30 mA), collimated by two, about $15\ \mu\text{m}$ wide slits, was sent on the CCD. We acquired images for different positions of the translation stage; steps were about $2\text{-}3\ \mu\text{m}$ long. The beam dimension was smaller than the pixel dimension. The idea is simple: as the slit width can be considered small compared to the pixel dimension, we can assume that the broadening effect (responsible for the more-pixel events) is exclusively due to charge diffusion in silicon (see later on). To measure the amount of broadening the chip was moved, until the beam was impinging in a region close to a pixel border. At this position it was possible to observe the adjacent pixel collecting a part of the charge. We had then a rough estimation of the cloud dimension. We moved farther until we acquired images for a total path of $56\ \mu\text{m}$, that means more than two pixels.

A spatial Gaussian distribution was assumed for the charge cloud. The Gaussian distribution had only one free parameter, σ (i.e. the dimension of the charge cloud). In fact the area and the position were given by the channel value of the involved pixels and the position of the CCD read on the caliper, respectively.

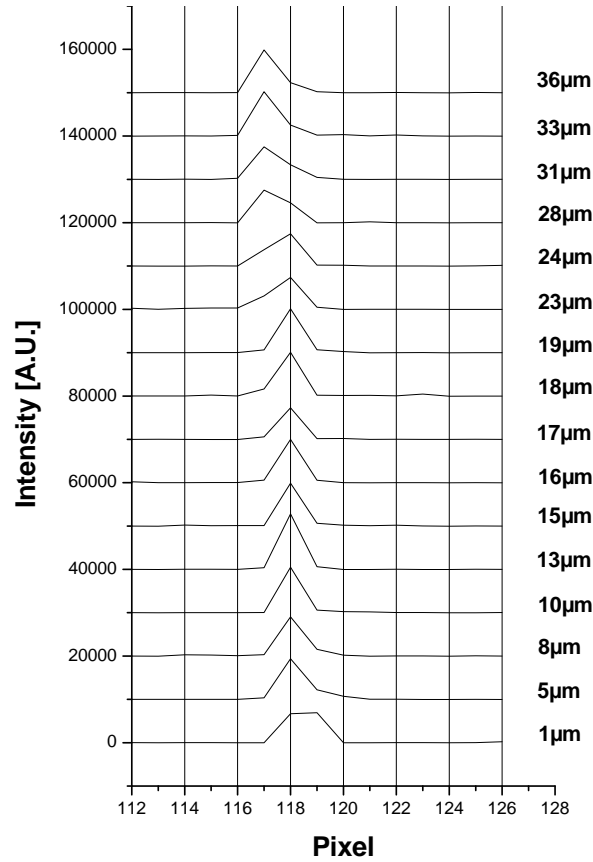


Figure A.6: Results obtained with the setup used in fig. A.5. On the abscissa is the pixel involved, on ordinate the measured intensity at the different positions of the CCD. The different positions, indicated on the right hand side of each plot, have been translated for the sake of clarity. The amount of photons involved for every plot is about 60.

By taking into account the apparatus function, we found $\sigma = (3.4 \pm 1.1) \mu\text{m}$ [Groom et al., 1999; Prigozhin et al., 2003; Tsunemi et al., 2001; Hiraga et al., 2001; Torii et al., 1995]. It's interesting to compare σ with what was found in tab. A.1. To do this, we define that there is a split event when more than 15% of the total generated charge lies in the neighbour pixel. Then the measured σ means that 53 % of the total amount of events are single pixel events, in good agreement with the measured value, 57%.

Photons with higher energies create more electron-hole pairs in a larger region. We performed Monte Carlo simulations to know which is the contribution to the dimension of the electron-hole

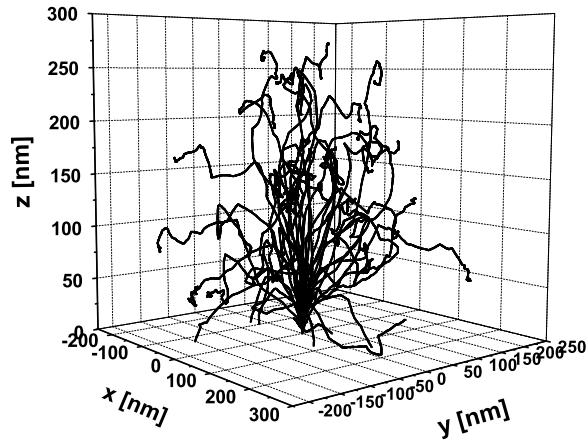


Figure A.7: The simulated path of 100 electrons having an energy of 4.5 keV in silicon. The scale for the three axis is the same.

cloud coming from the photon energy.

In the simulation the photon energy was supposed to be given to a single electron, that is uniformly slowed down in the matter, following [Joy, 1995], and that creates electron-hole pairs along his path.

The number of electron-hole pairs vs. radius of the generated cloud was plotted in fig. A.8.

For titanium the radius is some hundreds of nm large, it means that the measured charge cloud dimension was due only to the charge diffusion in silicon.

For tin the situation is clearly different. Here the final dimension is the sum of two contributions: the diffusion part (the σ previously measured) and the part caused by the longer path of electrons in silicon. Using the quadrature sum we get $\sigma_{total}=4.3 \mu\text{m}$. Again we want to compare the σ_{total} coming from the simulation with the amount of single pixel event found in tab. A.1: here we find 45 %, to be compared to the 47 % previously measured.

In conclusion a calibration of a deep-depletion back-illuminated CCD used for TRXD purposes was performed. For Ti-K α an efficiency of about 90% and for Cu-K α almost 50% was found. In comparison, a similar CCD not deep depletion from the same manufacturer, was tested and gave

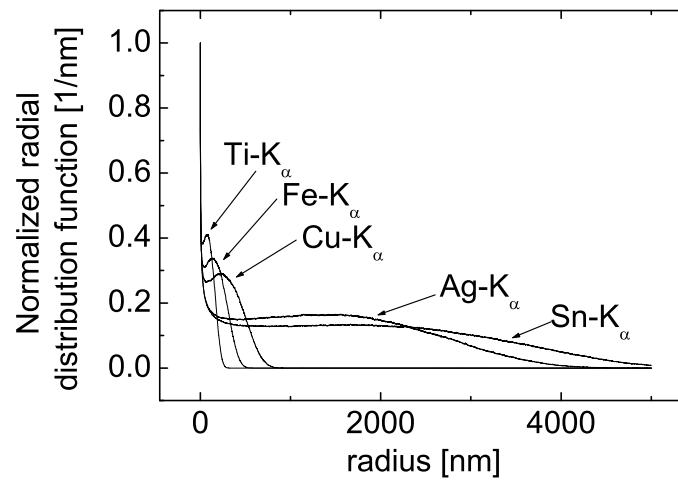


Figure A.8: The radial distributions of the electron hole pairs cloud produced by one electron having the energy of different $K\alpha$ lines. The values are normalized to the highest value to allow a direct comparison.

44% and 18% quantum efficiency for titanium and copper, respectively [Volkmer, 2004].

Especially in the case of titanium, almost every impinging photon is detected and a clear track is left on the CCD.

Im Rahmen dieser Arbeit wurde das Verhalten von Elektronen im Festkörpertarget im Energiebereich 4 keV...14 MeV als Folge von relativistischer Laser-Plasma Wechselwirkung erforscht. Ultrakurze, ultraintensive Laserpulse wurden auf Intensitäten von bis zu $5 \cdot 10^{19}$ W/cm² fokussiert. Mit Hilfe eines hochauflösenden Röntgenspektrometers ($E/\Delta E \approx 15000$) sowie eines energieauflösenden Röntgen-2D-Abbildungsystems wurde die Röntgenemission untersucht.

Ti-K α Linien wurden beobachtet, und eine eindeutige intensitätsabhängige symmetrische Verbreiterung konnte gemessen werden. Im Weizmann Institut (Israel) durchgeführte Berechnungen zeigen, dass es sich nicht um Stark- oder Doppler-Effekt handelt. Sorgfältige Datenanalyse, Betrachtung von den Symmetrien der Linienverbreiterungen und die Tatsache, dass es keine Linienverschiebung gab, konnten auch den im Prinzip möglichen Einfluss von Satelliten ausschliessen. Nur der Einfluss von Magnetfeldern kann die Größe der Linienverbreiterung erklären. Es wurde also zum ersten Mal der Zeeman-Effekt im Labor im Röntgenbereich beobachtet. Verantwortlich dafür sind die extrem hohen Magnetfelder, die bei der Laser-Plasma Wechselwirkung und bei der Elektronenausbreitung im "kalten" Target entstehen. Es wird betont, dass die Linienverbreiterung auf zwei unabhängige Art und Weisen sichtbar wird: Sowohl bei der Auswertung zweier Spektren, die bei verschiedenen Laserintensitäten aufgenommen wurden als auch in ein und demselben spektralen Bild, wenn zwei Scans (Spektren) verglichen werden, die verschiedene Abstände vom Intensitätsmaximum haben. Mittlere Magnetfeldstärken von $\approx 10^4$ T erklären die gemessene K α Linienverbreiterung. In Simulationen wird eine maximale Feldstärke von $(18 \pm 5) 10^3$ T abgeschätzt. Zum ersten Mal konnten laser-produzierte Magnetfelder in Plasmen mit Festkörperdichte beobachtet werden. Nach heutigem Kenntnisstand ist die Röntgenspektroskopie die einzige Methode, die solche Messungen erlaubt.

Im zweiten Teil dieser Dissertation wurde ein Röntgenpolarisator mit dem hochauflösenden

Röntgenspektrometer gekoppelt, um die Polarisations-eigenschaften der Ti-K α Liniensatelliten zu untersuchen. Eine starke Polarisationsabhängigkeit der Satelliten wurde festgestellt. Die Evolution der polarisierten Spektren als Funktion des Abstandes vom Intensitätsmaximum wurde bestimmt. Kann der Einfluss elektrischer und magnetischer Felder vernachlässigt werden, ist die Polarisationsabhängigkeit eng verbunden mit einer strahlartigen Elektronenverteilung und weist daher auf stark anisotrope Prozesse in dem laserbestrahlten Target hin. Die Spektralanalyse kann deshalb benutzt werden, um Elektronentransporteigenschaften unter extremen Bedingungen zu studieren.

Im dritten Teil dieser Arbeit wurde ein energieauflösendes 2D abbildendes System verwendet, um eine durch relativistische Laserintensitäten erzeugte Röntgenquelle zu untersuchen. Deutliche Unterschiede in Intensität und Größe der Quelle zwischen Vorder- und Rückseite wurden (sogar für sehr dünne Folien) gemessen. Die Benutzung von Schichttargets für die energieaufgelösten Abbildungen mit hoher räumlicher Auflösung (5 μm) erlaubt, quantitative Aussagen über die Quelleigenschaften zu treffen:

- In verschiedenen Targettiefen wurden verschiedene Quellen unterschiedlicher Größe (zwischen 14 und mehr als 65 μm) identifiziert.
- Es deutet vieles darauf hin, dass erstmals die Grenzflächenemission beobachtet werden konnte, die durch ein Magnetfeld erzeugt wird, das durch den Sprung im spezifischen Widerstand η an der Grenzfläche zweier Materialien entsteht ($\frac{\partial \mathbf{E}}{\partial t} = \mathbf{j}_{fast} \times \nabla \eta$). Diese großen Felder führen zu einer Ablenkung der Elektronen und damit zur Emission von Bremsstrahlung.
- Die Röntgendiagnostik liefert eine maximale Divergenz des Elektronenstrahles im Target von 0.15 rad, während ein Elektronenspektrometer einen Wert von 0.5 rad liefert. Diese Diskrepanz kann durch große elektrische Felder ($\sim \text{TV/m}$) auf der Targetrückseite, die durch Raumladungen induziert wurden, erklärt werden.
- Die Quelle auf der Targetrückseite ist von einem 90 μm großen Halo umgeben. Dieses wird einem Rückflusseffekt durch die Raumladungsfelder zugeschrieben. Ein deutlich schwächerer und breiterer Ring (einige hundert μm) tritt auch auf der Vorderseite auf.

Curriculum Vitae

Persönliche Daten

Name:	Flavio
Vorname:	Zamponi
Geburtsdatum:	8. Mai 1975
Geburtsort:	Macerata (Italien)
1 Kind	

Schulbildung

1981–1989:	Grundschule
1989–1994:	Liceo Scientifico “G. Galilei” Macerata (Italien)
1994–2002:	Studium der Physik an der Universität Pisa (Italien)
Diplomarbeit zum Thema:	”Nomarsky interferometry of plasmas produced by picosecond laser pulses”
2001–2002:	Zivildienst
Seit August 2002:	Doktorand am Institut für Optik und Quantelektronik der FSU Jena

Jena, den 14. Mai 2007

Flavio Zamponi

Ehrenwörtliche Erklärung

Ich erkläre hiermit ehrenwörtlich, dass ich die vorliegende Arbeit selbstständig und ohne Hilfe Dritter und ohne Benutzung anderer als der angegebenen Hilfsmittel und Literatur angefertigt habe. Die aus anderen Quellen direkt oder indirekt übernommenen Daten und Konzepte sind unter Angabe der Quelle gekennzeichnet.

Weitere Personen waren nicht an der inhaltlich-materiellen Erstellung der vorliegenden Arbeit beteiligt. Insbesondere habe ich hierfür nicht die entgeltliche Hilfe von Vermittlungs- bzw. Beratungsdiensten (Promotionsberater oder andere Personen) in Anspruch genommen. Niemand hat von mir unmittelbar oder mittelbar geldwerte Leistungen für die Arbeiten erhalten, die im Zusammenhang mit dem Inhalt der vorgelegten Dissertation stehen.

Die Arbeit wurde bisher weder im In- noch im Ausland in gleicher oder ähnlicher Form einer anderen Prüfungsbehörde vorgelegt.

Die geltende Prüfungsordnung der Physikalisch-Astronomischen Fakultät ist mir bekannt.

Ich versichere ehrenwörtlich, dass ich nach bestem Wissen die reine Wahrheit gesagt und nichts verschwiegen habe.

Jena, den 14. Mai 2007

Flavio Zamponi